

# **Antinuclei Production in Central Au-Au Collisions at RHIC**

Dissertation  
zur Erlangung des Doktorgrades  
der Naturwissenschaften

vorgelegt beim Fachbereich Physik  
der Johann Wolfgang Goethe-Universität  
in Frankfurt am Main

von  
Christof Struck  
aus Marburg

Frankfurt am Main, 2003  
(D F 1)

Vom Fachbereich Physik der  
Johann Wolfgang Goethe-Universität als Dissertation  
angenommen.

Dekan: Prof. Dr. Horst Schmidt-Böcking

Gutachter: Prof. Dr. Reinhard Stock  
Prof. Dr. Herbert Ströbele

Datum der Disputation:

# Zusammenfassung

Ultra-relativistische Schwerionenstöße bieten die einzigartige Möglichkeit, extrem verdichtete Kernmaterie zu erzeugen. Ziel ist hierbei der experimentelle Nachweis und das Studium des Quark-Gluon-Plasmas — ein Zustand, bei dem sich die hadronische Kernmaterie auflöst und sich deren Bestandteile, Quarks und Gluonen, in einem kollektiven, stark wechselwirkenden System frei bewegen können.

Aufgrund von Modellrechnungen, basierend auf der Theorie der starken Wechselwirkung, der Quanten-Chromodynamik, erwartet man den Phasenübergang von hadronischer Materie zum Quark-Gluon-Plasma etwa bei einer Temperatur von 170 MeV und einer Energiedichte von  $1 \text{ GeV}/\text{fm}^3$ . Die langjährigen Messungen am CERN-SPS, unter anderem mit Blei-Blei-Kollisionen bis zu einer Schwerpunktsenergie von 17 GeV/Nukleonpaar, und auch die ersten Ergebnisse am RHIC, mit Schwerpunktsenergien bis zu 200 GeV/Nukleonpaar, zeigen, daß diese Temperaturen und Dichten im Anfangsstadium von zentralen Kollisionen erreicht und — am RHIC sogar deutlich — überschritten werden.

Ein genaues Studium des Phasenübergangs gestaltet sich jedoch schwierig. Einerseits ist die exakte Phasenstruktur stark wechselwirkender Materie noch weitgehend unbekannt, und andererseits existiert der extrem verdichtete und aufgeheizte Zustand in Schwerionenkollisionen nur für sehr kurze Zeit — einige Fermi/c ( $10^{-23}$  Sekunden). Der in den Kollisionen erzeugte Feuerball kühlt ab und dehnt sich explosionsartig aus, ein erzeugtes Quark-Gluon-Plasma kondensiert dabei wieder zu hadronischer Materie. Mit Ausnahme von einigen direkten Signalen der Anfangsphase der Kollision, ist nur dieser Endzustand für Detektoren zugänglich.

Für das detaillierte Verständnis der dynamischen Evolution des Feuerballs einer Schwerionenkollision ist die exakte Kenntnis des hadronischen Endzustandes essenziell und gleichzeitig die Grundlage für die Interpretation der Observablen des Anfangszustands. Diese Arbeit soll einen Beitrag dazu liefern, indem die Emission von leichten Kernen, auch *Cluster* genannt, analysiert wird. Dieser Forschungsansatz ist aus der Physik des kosmischen Urknalls schon wohl vertraut. Dort analysiert man die relativen Häufigkeiten leichter Kerne (He, Li, Be bis C), die ebenfalls im Zuge der Expansions-Abkühlung

kondensieren; sie ergeben eine Art von „Moment-Aufnahme“ für ein charakteristisches Stadium der Expansion, das die vorhergehende Dynamik zu verstehen hilft. In Schwerionenkollisionen können leichte Kerne aufgrund ihrer geringen Bindungsenergie im Vergleich zur Feuerballtemperatur nur am Ende der dynamischen Entwicklung der Kollision durch Koaleszenz von Nukleonen produziert werden. Hier liefert ihre Häufigkeitsverteilung somit Informationen vom Endzustand sowie der vorhergegangenen kollektiven Expansion.

Im Rahmen dieser Arbeit wurde die Emission leichter **Antimaterie**-Kerne in zentralen Gold-Gold-Kollisionen bei einer Schwerpunktsenergie von 200 GeV/Nukleonpaar betrachtet. Dazu wurden die Daten des STAR Detektors am RHIC analysiert. STAR ist ein Hadronen-Detektor, der sich durch hohe Präzision in der Impulsmessung und Teilchenidentifikation in einem sehr großen Akzeptanzbereich auszeichnet. Wichtigste Komponente ist eine großvolumige *Time Projection Chamber* (TPC), die, unter anderem, die Möglichkeit zur Identifikation leichter Kerne bietet. Insbesondere zweifach geladene Teilchen, wie Helium-3 und Antihelium-3, können mit der STAR TPC annähernd im gesamten Impulsraum gemessen und, anhand des spezifischen Energieverlusts  $dE/dx$  der Teilchen im Gas der TPC, identifiziert werden.

Da Untergrund, verursacht durch die Wechselwirkung von Hadronen im Detektormaterial, die Messung von Materie-Kernen erheblich stört, wurde im Rahmen dieser Arbeit nur die Emission von Antimaterie-Kernen, Antideuteronen und Antihelium-3, eingehend studiert. Allerdings sind diese Observablen äußerst selten: In 3 Millionen Kollisionen wurden nur etwa 5000 Antideuteronen und 193 Antihelium-3-Cluster beobachtet.

Ein Teil dieser Arbeit war der Entwicklung des Level-3 Trigger-Systems in STAR gewidmet. Motivation dieses System ist die Anreicherung von seltenen Observablen bei einer gleichzeitigen Reduktion des Rohdatenflusses durch eine gezielte *online* Selektion von Kollisionen. Hierzu muß eine höhere Rate zur *online* Dateninspektion zur Verfügung stehen, als zum Speichern der Daten. Der Rohdatenfluß aus der großvolumigen TPC beträgt circa 20 MByte pro Kollisionsereignis, wobei RHIC etwa 50 zentrale Kollisionen der Goldkerne pro Sekunde zur Analyse anbietet. Der daraus resultierende Rohdatenfluß von etwa 1 GByte/s kann (und soll) nicht vollständig auf Band geschrieben werden. Der Level-3 Trigger filtert relevante Ereignisse heraus.

Das Level-3 System, bestehend aus einer Multiprozessor-Farm, leistet eine schnelle Spurrekonstruktion in der TPC — mit einer Rate von derzeit bis zu 50 Hz — und erlaubt so eine Ereignisselektion aufgrund von physikalischen Observablen, identisch mit entsprechenden *offline*-Analysen. Die Spurrekonstruktion gleicht der entsprechenden *offline*-Rekonstruktion und erreicht annähernd deren Effizienz und Präzision in der Impulsbestimmung. Allerdings steht dem Level-3 System der primäre Kollisionsvertex nicht mit der gleichen Auflösung zur Verfügung, wie der *offline*-Rekonstruktionskette. Somit ver-

richtet die Level-3-Rekonstruktion auf eine Unterscheidung zwischen primären Teilchenspuren, die direkt an oder nahe bei dem primären Vertex emittiert werden, und Spuren von sekundären Teilchen, die aus Zerfallsprozessen oder Gammakonversionen entfernt vom primären Vertex stammen, und behandelt alle Spuren als Teilchen sekundären Ursprungs bei entsprechend geringerer Impulsauflösung.

Die Messung des spezifischen Energieverlusts  $dE/dx$  der Teilchen im Gas der TPC steht auch im Level-3 System zur Teilchenidentifikation zur Verfügung. Allerdings wird auf eine detaillierte Kalibration dieser Daten *online* verzichtet, im Interesse der Analysegeschwindigkeit. Folglich ist *online* die  $dE/dx$ -Auflösung um einige Prozent geringer, aber für die Anwendung in der Triggerentscheidung ausreichend.

Ein Trigger auf die sehr seltenen Antihelium-Kerne ( $Z = -2$  Trigger) stellt eine typische Anwendung des Level-3 Systems dar, die durch das hohe Signal-zu-Untergrund-Verhältnis für Antimaterie-Cluster zusätzlich begünstigt ist. Dieser Triggeralgorithmus wurde im Rahmen dieser Arbeit implementiert und kam während der Gold-Strahlzeit des Jahres 2001 zum Einsatz, als das Level-3 System erstmalig zur Anreicherung von seltenen Observablen eingesetzt wurde. So konnten etwa 0.7 Millionen zentrale Gold-Gold-Kollisionen, zusätzlich zu den 3 Millionen ohne Level-3 Trigger gespeicherten Ereignissen, *online* im Level-3 System rekonstruiert und nach Antihelium-Signalen in der TPC durchsucht werden. Ein längerer Einsatz des Level-3 Systems war nicht möglich, da bei der meist niedrigen Luminosität von RHIC während der Gold-Strahlzeit 2001 die Voraussetzung einer hohen Ereignisrate zur *online* Selektion nicht gegeben war.

Die Beschreibung der Datenanalyse dieser Arbeit ist in zwei Teile gegliedert. Der erste Teil (Kapitel 4) betrachtet die Analyse des, durch den  $Z = -2$  Trigger angereicherten Datensatzes. Im zweiten Teil (Kapitel 6) wird anschließend die Analyse des normalen, ohne Level-3 Trigger gewonnenen Datensatzes detailliert dargelegt.

Der im  $Z = -2$  Trigger verwendete Algorithmus zur Antihelium-Identifikation entspricht annähernd der *offline*-Analyse. Hierzu werden Spuren als  $Z = -2$ -Kandidaten selektiert, die einen spezifischen Energieverlust  $dE/dx$  entsprechend dem Erwartungswert für diese Teilchen zeigen und Mindestanforderungen an die Spurqualität, wie Spurlänge und Anzahl der einzelnen  $dE/dx$ -Messungen, erfüllen. Wesentlich für die Analyse des angereicherten Datensatzes ist einerseits die Bestimmung der Trigger-Effizienz und andererseits eine exakte Normierung. Der vom Level-3 Trigger unbeeinflusste Datensatz bot ausreichend Statistik, um die Effizienz des  $Z = -2$  Triggers mit den Daten selbst zu bestimmen. Dazu wurden die Antihelium-3-Kandidaten der Level-3-Rekonstruktion mit den Kandidaten der *offline*-Analyse ereignisweise verglichen. Die so gewonnene Trigger-Effizienz erreicht oberhalb eines transversalen Impulses von  $p_t = 1$  GeV/c etwa 80% relativ zur *offline*-Analyse, un-

terhalb circa 50%.

In den vom  $Z = -2$  Trigger selektierten 867 Events, aus 0.7 Millionen ausschließlich *online* analysierten Kollisionen, wurden von der *offline*-Analyse 28 Antihelium-3-Kerne gefunden, zusätzlich zu 193 aus dem normalen Datensatz von 3 Millionen Kollisionen. Dies ist mit dem Erwartungswert bei einer Trigger-Effizienz von circa 80% verträglich.

Soll diese Verstärkung des seltenen Antihelium-Signals auch in der Berechnung des invarianten Wirkungsquerschnitts  $E \frac{d^3\sigma}{dp^3}$  berücksichtigt werden, so ist neben der Trigger-Effizienz auch die genaue Normierung auf die Zahl der verwendeten Ereignisse wichtig. Die hierzu notwendige Zahl der ausschließlich *online* analysierten Ereignisse läßt sich entweder aus den vom Level-3 System geführten Zählern entnehmen, oder aus der Zahl der nicht von Level-3 selektierten, d.h. zufällig gewählten, Kollisionen — vorausgesetzt, das Verhältnis von Level-3-Eventrate zu Datensicherungsrate war konstant.

Ein Vergleich der gewonnenen invarianten Wirkungsquerschnitte von Antihelium-3 mit und ohne Berücksichtigung des von Level-3 angereicherten Datensatzes zeigt eine gute Übereinstimmung innerhalb der statistischen Unsicherheiten. Bereits die Verstärkung des Signals um 20% durch den  $Z = -2$  Trigger bewirkt eine Reduzierung der statistischen Unsicherheit der Ergebnisse, auch mit Berücksichtigung der Unsicherheit der Trigger-Effizienz.

Dies zeigt die Äquivalenz von *online* Level-3- und *offline*-Rekonstruktion und damit die Möglichkeiten des Level-3 Systems zur Verstärkung von seltenen Observablen in STAR. Dieses System bringt zukünftig — eine ausreichende Luminosität von RHIC vorausgesetzt — eine Beobachtung von Antialpha-Kernen und Seltsamkeit tragenden Anti-Hypertritonien in den Bereich des Möglichen. Weiterhin erlaubt es die Messung von Antihelium-3 mit hoher Statistik.

Wie bereits erwähnt, wurde im Rahmen dieser Arbeit sowohl die Antihelium-3- als auch die Antideuteron-Emission analysiert, basierend auf den primären Teilchenspuren der *offline*-Datenrekonstruktion.

Ebenso wie Antihelium-3, werden Antideuteronen anhand des spezifischen Energieverlusts  $dE/dx$  identifiziert. Allerdings ist dies für Antideuteronen auf einen relativ kleinen Impulsbereich von  $0.4 < p_t < 0.9$  GeV/c beschränkt. Im Gegensatz zum praktisch untergrundfreien Antihelium-3-Signal, wurde zunächst das Antideuteron-Signal mit Hilfe einer entsprechenden Parametrisierung von Untergrund- und Signalverteilung vom Untergrund getrennt. Die Analyse der Clusterausbeute beinhaltet außerdem eine Korrektur der geometrischen Akzeptanz und Rekonstruktionseffizienz, sowie der Absorptionsverluste im Detektormaterial.

Auf diese Weise wurde der invariante Wirkungsquerschnitt für Antideuteronen, im Impulsbereich  $0.4 < p_t < 0.9$  GeV/c und Rapidität  $|y| < 0.3$ , und Antihelium-3, im Bereich  $1.0 < p_t < 5.0$  GeV/c und  $|y| < 1$ , bestimmt. Die

systematischen Unsicherheiten wurden dabei durch Variation der Identifikationskriterien und Korrekturparameter auf etwa 10% abgeschätzt, mit Ausnahme der Randbereiche im verwendeten Impulsbereich für Antideuteronen, in denen die Unsicherheiten 30 bis 40% erreichen. Die, im Vergleich zu bisherigen Messungen, große Zahl von Antihelium-3-Kernen in diesem Datensatz erlaubte — erstmalig in der Schwerionenphysik — die Berechnung des differentiellen invarianten Wirkungsquerschnitts als Funktion des transversalen Impulses.

Die Interpretation der Ergebnisse (Kapitel 7) erfolgte einerseits in Bezug auf einfache statistische, bzw. thermische Modelle und andererseits im Rahmen des Koaleszenz-Modells der Clusterproduktion. Für letzteres ist die Hinzunahme des Multiplizitätsspektrums der Antiprotonen notwendig, das ebenfalls in STAR gemessen wurde.

Zunächst wurden die gemessenen Multiplizitäten von Antiprotonen, Antideuteronen und Antihelium-3 anhand eines statistischen Modells verglichen. Unter der Annahme eines Feuerballs im thermischen und chemischen Gleichgewicht lassen sich die globalen Eigenschaften Temperatur  $T$  und chemisches Potential  $\mu$  zum Zeitpunkt der Clusterproduktion aus den gemessenen Multiplizitäten bestimmen. Diese zeigen eine gute Übereinstimmung mit dem statistischen Modell bei einer Temperatur von  $(135 \pm 15)$  MeV und einem chemischen Potential von  $(5 \pm 15)$  MeV. Eine entsprechende Interpretation von SPS-Daten ergibt eine sehr ähnliche Temperatur von  $(130 \pm 15)$  MeV, bei höherem chemischen Potential von  $(200 \pm 15)$  MeV. Die Übereinstimmung der Clustermultiplizitäten mit diesem Modell läßt die gleiche Schlußfolgerung zu, wie die statistische Analyse der hadronischen Endzustände in Kern-Kern- sowie in elementaren Elektron-Elektron- und Proton-Proton-Kollisionen. Demnach wird auch die Produktion von Clustern rein statistisch von dem Phasenraum dominiert, der bei der Temperatur  $T$  und chemischen Potential  $\mu$  zur Verfügung steht. Diese Modelle nehmen, ebenso wie für die Hadronen beim chemischen Ausfrieren des Feuerballs, einen Zustand höchster Entropie, und damit thermisches und chemisches Gleichgewicht, bei der Entstehung an.

Das Transversalimpuls-Spektrum der Antihelium-3-Kerne liefert weitere Informationen über die dynamische Expansion des Feuerballs. So deutet der *slope*-Parameter von  $(950 \pm 140)$  MeV im Vergleich zum *slope*-Parameter des Antiproton-Spektrums auf eine hohe transversale Flußgeschwindigkeit hin. Der aus dem Spektrum extrahierte mittlere Transversalimpuls  $\langle p_t \rangle = 2.6 \pm 0.4$  GeV/c der Antihelium-3-Emission, erlaubt die Angabe einer oberen Grenze für die Flußgeschwindigkeit von  $(0.68 \pm 0.06)c$ , da die mittlere transversale Bewegung dieser schweren Teilchen nicht von der thermischen Bewegung, sondern der kollektiven Expansion dominiert wird.

Eine genauere Abschätzung der Fluß- oder Expansionsgeschwindigkeit des Feuerballs am Ende seiner dynamischen Entwicklung läßt sich aus der Verteilung des mittleren Transversalimpulses als Funktion der Teilchenmasse ge-

winnen. Dieser wurde in STAR, neben Antihelium-3, auch für Pionen, Kaonen und Protonen gemessen. Unter der Annahme eines idealen Gases im thermischen Gleichgewicht kann der mittlere Transversalimpuls als Funktion der Temperatur, der transversalen Expansionsgeschwindigkeit und der Teilchenmasse angegeben werden. Eine Anpassung dieser Funktion zeigt gute Übereinstimmung mit den Daten für eine Temperatur von  $(130 \pm 40)$  MeV und eine mittlere Expansionsgeschwindigkeit von  $(0.46 \pm 0.08)c$  und bestätigt somit die Temperatur der statistischen Analyse. Ebenso wie die Temperatur entspricht die transversale Expansionsgeschwindigkeit am RHIC den Beobachtungen in zentralen Blei-Blei-Kollisionen am SPS.

Die Multiplizitäten der Antideuteronen und Antihelium-3, sowie der gemessenen Antiprotonen erlauben die Berechnung der Koaleszenz-Parameter  $B_2$  und  $B_3$ . Diese werden als Verhältnis des invarianten Wirkungsquerschnitts der Cluster mit Massenzahl  $A$  und dem  $A$ -fachen Produkt der Nukleon-Spektren definiert und erlauben Rückschlüsse auf das Feuerballvolumen zum Zeitpunkt der Clusteremission. Im Rahmen eines einfachen thermischen Modells erwartet man einen antiproportionalen Zusammenhang zwischen Koaleszenz-Parameter und Volumen. Die im Rahmen dieser Arbeit berechneten Parameter  $B_2 = (0.41 \pm 0.2) \times 10^{-3} \text{ GeV}^2/c^3$  (bei einem Transversalimpuls der Antideuteronen von  $0.75 \text{ GeV}/c$ ) und  $B_3 = (0.15 \pm 0.1) \times 10^{-6} \text{ GeV}^4/c^6$  (bei  $p_t = 2.5 \text{ GeV}/c$  der Antihelium-3-Cluster) folgen dem bisher beobachteten Trend in Kern-Kern-Kollisionen von abnehmenden Parametern bei ansteigender Schwerpunktsenergie. Entsprechend dem thermischen Modell kann dies qualitativ mit einem Anstieg des Feuerballvolumens erklärt werden.

Eine quantitative Interpretation der Koaleszenz-Parameter erfolgte im Rahmen dieser Arbeit in Bezug auf das Koaleszenz-Modell von Scheibl und Heinz, da ausschließlich diese theoretische Beschreibung der Clusteremission eine longitudinale und transversale Expansion des Feuerballs einschließt. Dieses Modell stellt einen Zusammenhang zwischen den Koaleszenz-Parametern und Homogenitätswolumina her, die auch bei Hanbury-Brown-Twiss-Korrelationsanalysen extrahiert werden. Diese beschreiben nicht die absolute Größe des Feuerballs im Koordinatenraum, sondern die Größe der Regionen im Feuerball, in denen Teilchen mit ähnlichen Impulsen emittiert werden. Die hier berechneten Homogenitätswolumina (gemessen bei einer transversalen Masse größer  $1 \text{ GeV}/c^2$ ) aus der Antideuteron- und Antihelium-3-Emission stimmen sehr gut miteinander überein — auch mit den Ergebnissen von Pion-Pion-Korrelationen bei niedrigeren transversalen Massen. Im Vergleich zum SPS zeigt diese Analyse einen Anstieg der Homogenitätswolumina um einen Faktor zwei.

Als Ergebnis dieser Arbeit läßt sich abschließend feststellen, daß sich der Endzustand der Schwerionenkollisionen am RHIC nur geringfügig vom SPS unterscheidet. Sowohl die Temperatur im Feuerball am Ende der dynamischen Entwicklung, zum Zeitpunkt des kinetischen Ausfrierens, als auch die



transversale Expansionsgeschwindigkeit saturieren mit der Schwerpunktsenergie. Einzig eine Abnahme des chemischen Potentials und eine Zunahme der Homogenitätsvolumina wurde beobachtet. Dies ist zunächst überraschend, steht doch am RHIC eine zwei- bis dreifach höhere Energiedichte im Anfangszustand zur Verfügung. Dies bewirkt offensichtlich keine gravierenden Änderungen des hadronischen Enzustands, der im Gegenteil von streng statistischen Prozessen dominiert wird.



# Contents

<b>Zusammenfassung</b>	<b>i</b>
<b>1 Introduction and Overview</b>	<b>1</b>
1.1 Heavy-Ion Collisions . . . . .	4
1.1.1 Thermodynamic Picture . . . . .	6
1.2 Light Cluster Formation . . . . .	8
1.2.1 Coalescence Models I: Classical Statistics . . . . .	9
1.2.2 Coalescence Models II: Quantum Statistics . . . . .	12
<b>2 The STAR Experiment</b>	<b>15</b>
2.1 The Magnet . . . . .	17
2.2 The Time Projection Chamber . . . . .	17
2.3 Additional Detectors . . . . .	20
2.4 The Trigger . . . . .	21
2.5 The Relativistic Heavy Ion Collider . . . . .	24
<b>3 The Level-3 Trigger</b>	<b>27</b>
3.1 Architecture . . . . .	27
3.1.1 The STAR DAQ Architecture . . . . .	28
3.1.2 The Sector Level-3 . . . . .	29
3.1.3 The Global Level-3 . . . . .	29
3.2 Pre-/Postscaling and Counters . . . . .	30
3.3 Event Reconstruction . . . . .	32
3.3.1 Cluster Finding . . . . .	32
3.3.2 Track Finding . . . . .	34
3.3.3 Particle Identification . . . . .	36
3.3.4 Vertex Reconstruction and Distance of Closest Approach . . . . .	37
<b>4 The <math>Z = -2</math> Trigger Algorithm</b>	<b>39</b>
4.1 Cuts . . . . .	40
4.2 Trigger Efficiency . . . . .	44
4.3 Normalization . . . . .	46
4.4 Results . . . . .	48

4.5	Outlook . . . . .	51
<b>5</b>	<b>The Offline Reconstruction</b>	<b>53</b>
5.1	Event Reconstruction in the TPC . . . . .	53
5.1.1	Cluster Finding . . . . .	54
5.1.2	Track Finding . . . . .	54
5.1.3	Distortion Corrections . . . . .	54
5.2	Global Event Reconstruction . . . . .	56
5.2.1	Global Tracking . . . . .	56
5.2.2	Primary Vertex Reconstruction . . . . .	56
5.2.3	Primary Track Fit . . . . .	57
5.3	Particle Identification with $dE/dx$ . . . . .	57
5.3.1	The Bethe-Bloch Equation . . . . .	57
5.3.2	Measurement and Calibration . . . . .	58
5.4	Simulation . . . . .	60
<b>6</b>	<b>The Analysis of Antinuclei Spectra</b>	<b>61</b>
6.1	Data Set . . . . .	61
6.2	Antinuclei Identification . . . . .	62
6.2.1	Cuts . . . . .	64
6.3	Antinuclei Yield and Corrections . . . . .	65
6.3.1	Energy Loss . . . . .	66
6.3.2	Background Subtraction . . . . .	68
6.3.3	Acceptance and Efficiency . . . . .	72
6.3.4	Absorption . . . . .	72
6.4	Systematic Uncertainties . . . . .	77
6.4.1	Antideuteron Analysis . . . . .	77
6.4.2	Antihelium-3 Analysis . . . . .	79
6.5	Results . . . . .	79
6.5.1	Antideuteron Invariant Yield . . . . .	80
6.5.2	Antihelium-3 Invariant Yield . . . . .	81
6.6	Antiproton Invariant Yield . . . . .	81
<b>7</b>	<b>Discussion</b>	<b>85</b>
7.1	Antinuclei Abundance . . . . .	85
7.2	Inverse Slope and Mean Transverse Momentum . . . . .	87
7.3	Coalescence Parameter . . . . .	91
7.3.1	Collision Energy Dependence . . . . .	94
7.4	Volume of Homogeneity . . . . .	94
<b>8</b>	<b>Summary and Conclusion</b>	<b>99</b>
<b>A</b>	<b>Coordinates, Variables and Definitions</b>	<b>101</b>

<b>B Efficiency Uncertainties</b>	<b>103</b>
<b>Bibliography</b>	<b>111</b>
<b>Danksagung</b>	<b>117</b>



# Chapter 1

## Introduction and Overview

Relativistic heavy ion collisions are a unique tool to study nuclear matter under extreme conditions. They can be used to investigate the equation of state of strongly interacting matter in the region of very high temperature and density, apart from the conditions of nuclear matter otherwise accessible in the laboratory.

The constituents of strongly interacting matter, quarks and antiquarks, have so far only been observed in bound states of quark-antiquark pairs or triplets of (anti)quarks, i.e. hadrons. Within the picture of the very successful theory of strong interaction “Quantum Chromodynamics” (QCD) this *confinement* is due to a binding potential  $V_{QCD} \propto r$  rising linearly with the quark separation  $r$ . Thus, at some distance it becomes energetically favorable to produce a quark-antiquark pair instead of further separation. At the same time, the interaction weakens at small distances and large momentum transfers — an effect usually called *asymptotic freedom*.

Early after the theory of QCD was introduced, it was applied to hadronic matter at high temperatures and/or high densities [1]. There the asymptotic freedom reaches a point, where hadronic bound states melt to a collective state of strongly interacting matter, the so-called “Quark-Gluon Plasma” (QGP). Within a QGP the long-range binding potential is screened similar to the Debye-screening of the electromagnetic interaction at high densities and the *deconfined* quarks can move freely, see Figure 1.1.

The investigation of the phase structure of QCD was triggered by the Big Bang theory and the question of the inner structure of neutron stars [2], which both include phases of either extremely high temperature and low density — during the expansion of the universe within the first microseconds — or high density at low temperature in the inner core of neutron stars. The theoretical description of the phase structure has proven to be difficult. Indeed, potentially exact non-perturbative calculations are only possible with numerical computation techniques of Lattice QCD [3]. These calculations predict a phase boundary between a hadronic gas and QGP at a critical temperature  $T_c \approx 150 - 170$

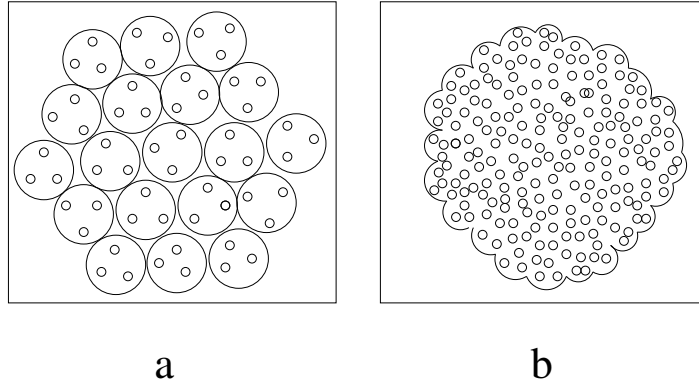


**Figure 1.1:** Simplified comparison of confined quarks in closely packed nuclear matter (a) and deconfined quark matter, i.e. Quark-Gluon Plasma, at very high densities (b).

MeV for vanishing baryon density. A schematic view of the phase diagram of strongly interacting matter is shown in Figure 1.2. The phase boundary at low temperatures is expected at about five to ten times the baryon density of nuclear matter  $\rho_0 \approx 0.15/\text{fm}^3$ . The evolution of the early universe and of neutron stars through the phase diagram is indicated by the solid lines.

For more than twenty years the field of Heavy-Ion Physics is active and motivated by the possibility to observe and study a creation of QGP in heavy ion collisions. Recently the field got new impulses, when the Relativistic Heavy Ion Collider (RHIC) at the Brookhaven National Laboratory was shut on. This accelerator facility provides gold beams with a top energy of 100 GeV/nucleon, and therefore collisions at a center-of-mass energy of 200 GeV/nucleon-pair. That way, an increase in the collision energy of more than an order of magnitude compared to the lead-lead collisions at 17 GeV/nucleon-pair at the Super Proton Synchrotron (SPS) at CERN can be achieved. Following up an extensive heavy-ion program at the SPS, RHIC now provides the possibility to study the QCD phase structure far closer to the limit of vanishing baryon density, and so in a region much more accessible to the theoretical description. The search for an experimental confirmation of the QGP turned out to be as complicated as the theoretical description. As the hot and dense fireball created in heavy ion collisions cools and expands rapidly, it has to cross the phase boundary twice, if that can be reached at all. Detectors mainly measure the hadronic remnants of the fireball, which are mostly pions, kaons and protons. These however carry exclusively information of the system after hadronization. Direct signals of the earlier and much hotter phase like leptons and photons are much more difficult to study, due to their much smaller cross sections. Possible signatures of QGP and the present understanding of experimental results are summarized in [4]. The interpretation of the SPS results allows the



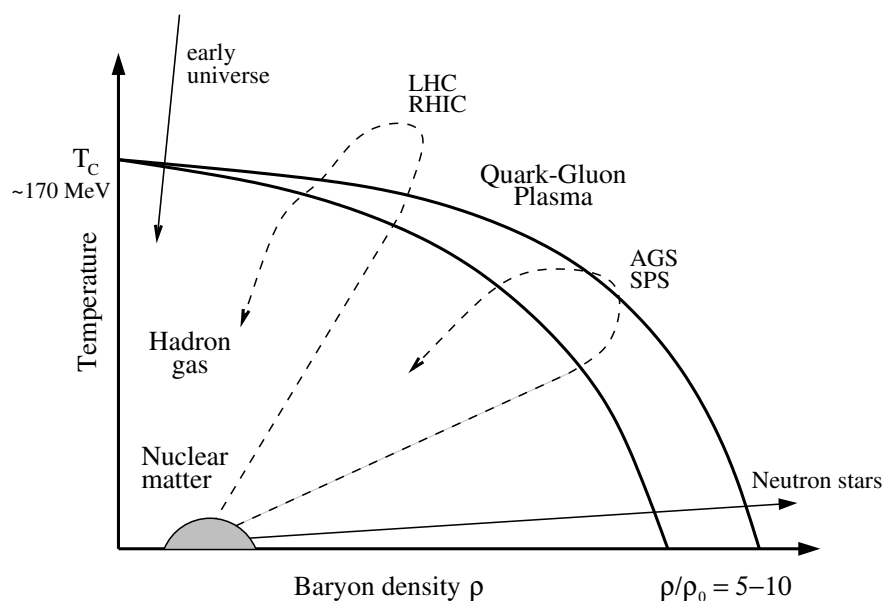


**Figure 1.2:** Schematic phase diagram of strongly interacting matter. Arrows indicate the evolution of different scenarios where a Quark-Gluon Plasma could have been created.

conclusion, that the data is at least consistent with a creation of QGP at top SPS energies [5].

This thesis is supposed to investigate light antinuclei production in relativistic heavy ion collisions. Light nuclei and antinuclei, often named light clusters, are very sensitive to the global conditions temperature, nucleon density, volume and collective motion at the last stage of the collisions, when all hadronic interactions cease. Profound knowledge of the global properties at the kinetic freeze-out of the fireball is the baseline for the understanding of the fireball evolution and allows to extrapolate back to the early phase.

This thesis is based on the data of the STAR detector at RHIC from the gold run at a beam energy of 100 GeV/nucleon during the year 2001. STAR is a large acceptance hadron detector with a Time Projection Chamber (TPC) as main component featuring high momentum resolution and good particle identification capabilities especially at low momenta. For double charged particles the TPC provides particle identification for almost the full momentum range and is thus well suited for the detection of light clusters.

At first, this thesis reports on the development of a high-level software trigger, the Level-3 trigger system, for the STAR detector. The Level-3 trigger is designed to enhance STAR's capabilities to record rare observables. The system performs a full online event reconstruction of the tracking detectors, i.e. the TPC during 2001, and thus allows to select events based on physics observ-

ables immediately. As one of the first applications a trigger on the very rare double negatively charged  $Z = -2$  particles, such as antihelium-3 and -4, was implemented as part of this work and ran during the year 2001 for the first time.

This thesis is structured into three main parts. The first chapter shall briefly introduce the current understanding of heavy ion collisions and the concept of light cluster formation, as well as the cluster coalescence model. Chapter 2 provides an overview of the STAR detector at RHIC. The second section, Chapters 3 and 4, shall explain the Level-3 trigger, especially the details of the  $Z = -2$  trigger. It will conclude with the comparison of the analysis results for antihelium-3 with and without triggered events proving the successful implementation of the Level-3 trigger. The last part of the thesis consists of three chapters and is dedicated to the data analysis: Chapter 5 will introduce first the offline event reconstruction followed by a detailed explanation of the antideuteron and antihelium-3 analysis in Chapter 6. The thesis will conclude with a discussion of the results and the interpretation with respect to the recent coalescence model which allows comparisons to the results of Hanbury-Brown, Twiss correlation measurements.

## 1.1 Heavy-Ion Collisions

Figure 1.3 explains the current understanding of heavy ion collisions at SPS and RHIC energies. This is taken from [6], where an overview on the standing of Heavy-Ion Physics is given after the first results from RHIC were published. The figure shall illustrate the evolution of the fireball created in central heavy ion collisions and indicate the global conditions at the different stages as well as the evidence for these from SPS and RHIC data. [6] and the references therein serve also as reference for the numbers quoted in the following paragraph.

The initial energy densities reached in central collisions are about  $3 \text{ GeV}/\text{fm}^3$  at SPS and above  $5 \text{ GeV}/\text{fm}^3$  at RHIC at temperatures about 220-250 MeV — well above the critical density and temperature of deconfinement. It seems to be obvious that the created fireball will reach a quark matter phase, however rapidly it cools and expands under pressure. Within a few Fermi/c ( $10^{-23}$  sec) the fireball hadronizes (chemical freeze-out) at a temperature of about 175 MeV and a chemical potential of 270 MeV at SPS and 45 MeV at RHIC. The evolution of the fireball after hadronization is very similar at SPS and RHIC. It further expands in both longitudinal and transverse direction with similar velocities in transverse direction. Finally, at a temperature of about 120 to 130 MeV the system reaches thermal (kinetic) freeze-out when hadronic interactions cease and the emitted particles move freely to the detectors.

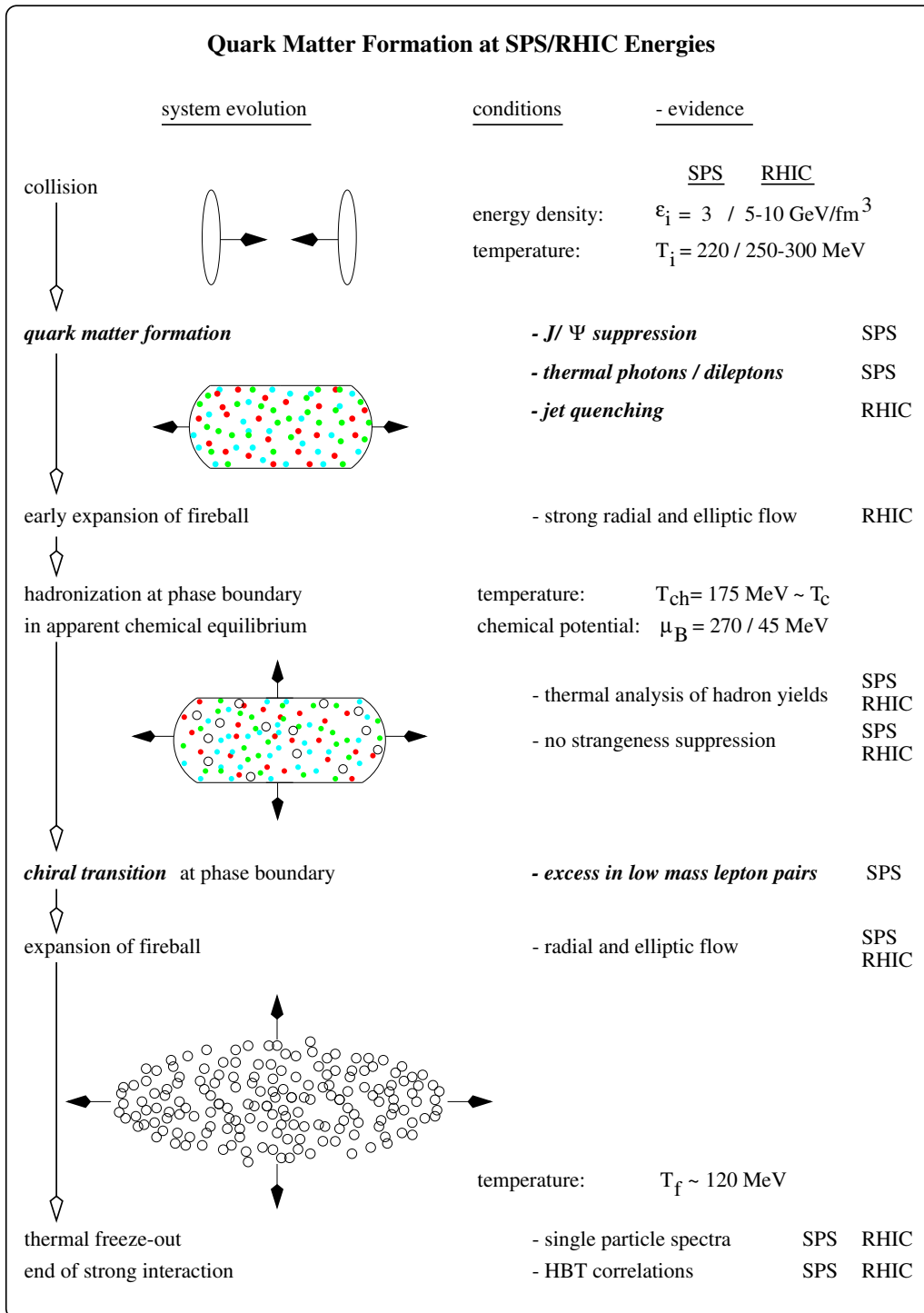


**Figure 1.3:** Fireball evolution after the impact of two heavy ions at SPS/RHIC energies. The global conditions and their evidence are given at the different stages. This figure was taken from [6].

### 1.1.1 Thermodynamic Picture

Thermodynamics — as already indicated by the language — is very suitable for a description of the macroscopic properties of the many-body reactions in heavy ion collisions. Both the system size (compared to the typical scale of strong interactions of one Fermi) and the particle number (in a Au nucleus 197 and in a Pb nucleus 208) are sufficiently large. Assuming thermal and chemical equilibrium, the properties temperature, energy, pressure, etc. can be expressed in terms of the Gibbs grand canonical ensemble [7].

Looking at the fireball after hadronization as it is done by the hadron detectors, the grand canonical partition function  $Z$  for a hadronic resonance gas at temperature  $T$  is defined in statistical mechanics as

$$Z = \sum_n \langle n | e^{(H - \mu \hat{N})/T} | n \rangle, \quad (1.1)$$

where  $H$  is the Hamiltonian,  $\mu$  the chemical potential and  $\hat{N}$  the particle number operator. Global baryon number, isospin and strangeness conservation requires the introduction of a chemical potential  $\mu$  (for a derivation see for example [8]), which plays an essential role for the particle number densities as shown below.

Coming from the partition function  $Z$ , the thermodynamic values pressure  $P$ , particle number  $N$  and entropy  $S$  can be calculated as usual,

$$P = T \frac{\partial \ln Z}{\partial V}, \quad (1.2)$$

$$N = T \frac{\partial \ln Z}{\partial \mu}, \quad (1.3)$$

$$S = \frac{\partial(T \ln Z)}{\partial T}. \quad (1.4)$$

$V$  is the volume of the system in which chemical equilibrium is reached. The energy  $E$  is given by

$$E = -PV + TS + \mu N. \quad (1.5)$$

In the simple situation of an ideal gas of boson and fermions the partition function becomes

$$\ln Z = \pm \frac{gV}{2\pi^2} \int p^2 dp \ln \left( 1 \mp e^{-\frac{E_i - \mu}{T}} \right). \quad (1.6)$$

Here,  $g$  is the spin degeneracy,  $E_i$  the energy of the particle of species  $i$  and  $\pm$  is selected according to the quantum statistics for bosons and fermions, respectively. From Equation 1.3 follows for the number of particles of a given species  $i$

$$N = \frac{gV}{2\pi^2} \int \frac{p^2 dp}{e^{\frac{E_i(p) - \mu}{T}} \mp 1} \quad (1.7)$$

and thus for the differential multiplicity

$$\frac{d^3 N}{dp^3} = \frac{gV}{(2\pi)^3} \frac{1}{e^{\frac{E_i(p)-\mu}{T}} \mp 1}. \quad (1.8)$$

The occurrence in Equation 1.7 shows the important role of the chemical potential  $\mu$  as a modifier of the vacuum energy  $E_i(p)$  in the medium with the temperature  $T$ . It thus changes the penalty factor for the production of a particle of species  $i$  with energy  $E_i(p)$ .

The well known Boltzmann distribution can be derived from Equation 1.8 in the limit of high temperatures and small chemical potentials, i.e.  $e^{(E_i-\mu)/T} \gg 1$ ,

$$\frac{d^3 N}{dp^3} \propto e^{-E_i(p)/T}, \quad (1.9)$$

which is the common basis for simple considerations from hadron spectra.

This statistical theory can be used to describe the hadronic resonance gas after hadronization of the fireball. In the description, often denoted as hadron chemistry [8, 9, 10], the basic thermodynamic parameters  $V$ ,  $T$  and the baryon chemical potential  $\mu_B$  are derived from a combined fit of Equation 1.7 to the measured hadron multiplicities. The chemical potential  $\mu_i$  of species  $i$  includes the three components baryon  $\mu_B$ , strangeness  $\mu_S$  and isospin chemical potential  $\mu_I$ ,  $\mu = \mu_B B_i + \mu_S S_i + \mu_I I_i$  for the given baryon number  $B_i$ , strangeness content  $S_i$  and isospin  $I_i$ . However, both  $\mu_S$  and  $\mu_I$  can also be expressed in terms of the baryon chemical potential. The success of this description of the hadronization on a wide range of collision energies in nucleus-nucleus collisions, as well as in elementary  $e^+e^-$  and  $pp$  collisions (where the canonical ensemble is employed), is quite remarkable. It shows that the fireball freezes out *into* a hadron gas in apparent thermal and chemical equilibrium [10], i.e. a state of maximum entropy dominated by the available phase space. The Equilibration cannot be reached by rescattering after hadronization, especially not in elementary  $e^+e^-$  and  $pp$  collisions.

Figure 1.4, taken from [11], shows a summary of the results of the statistical analysis for different collision energies in the QCD phase diagram. The data maps the phase diagram at the time of system hadronization in the direction of decreasing baryon chemical potential and increasing temperature for increasing collision energy. At SPS and RHIC energies the chemical freeze-out occurs very close to the phase transition boundary (recent values for RHIC data at 130 GeV/nucleon center-of-mass energy are  $T = 175$  MeV and  $\mu_B = 45$  MeV [12]).

The interpretation of the statistical analysis of the hadronization combined with the observed strangeness enhancement in central compared to peripheral  $AA$  collisions at SPS is one of the strongest arguments for the observation of a “little Big Bang” [10, 13], i.e. the creation of quark matter, in central heavy ion collisions at SPS energies and above.

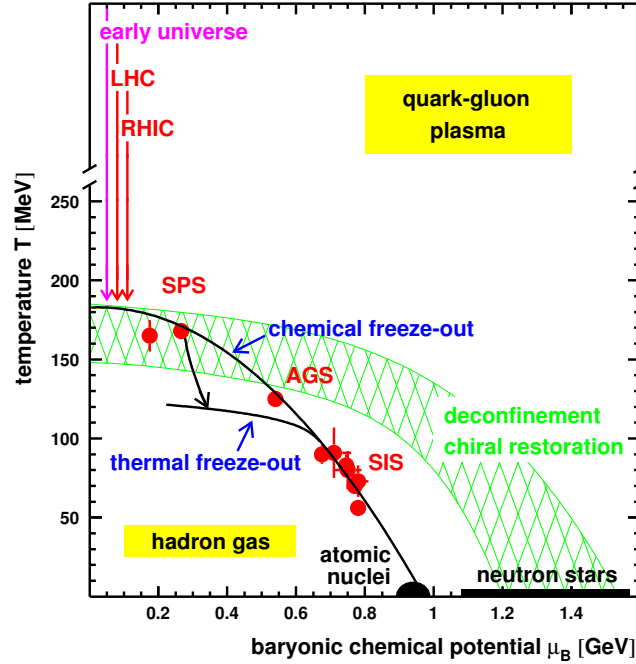


**Figure 1.4:** Phase diagram, taken from [11], mapped by the statistical analysis of hadron abundances at different collision energies. As indicated by the solid black line the hadron chemistry derives the thermodynamic variables at chemical freeze-out. Kinetic freeze-out occurs later in time after further cooling and expansion of the fireball.

The same statistical description can also be applied to the light cluster formation discussed in the following section, which then allows an investigation of the kinetical freeze-out of the fireball.

## 1.2 Light Cluster Formation

Light nuclei like deuterons, tritons, helium-3 and their antiparticles are among the exotics in the hadronic cocktail, which is found after kinetic freeze-out of the fireball created in heavy ion collisions. Now, one could expect nuclear cluster emission only close to beam rapidities as fragmentation in the spectator region. However, nuclei emitted at mid-rapidity and especially antinuclei must originate from the fireball. Since the cluster binding energy (e.g. 2.2 MeV for  $d$  and 7.7 MeV for  ${}^3\text{He}$ ) is very small compared to the temperature of the fireball (about 150 MeV), they can only reach the detector, if they are produced at the last stage of the collision — at kinetic freeze-out. Any clusters produced earlier re-interact during the hot and dense phase are very likely to break-up.

Therefore, the final-state coalescence is the dominating cluster formation mechanism, where  $A$  nucleons close in coordinate space with small relative momenta merge to a nuclear cluster with mass number  $A$ . Thus, cluster yields are very sensitive not only to the phase-space distribution of the particles in the source at kinetic freeze-out, but also the source size and shape in coordinate space. In particular, the space-momentum correlations generated by collective motion, where particles close in space have similar momenta, have a strong effect on final-state coalescence.

As pointed out first by Mrówczyński [14], the physics of coalescence is very similar to the Hanbury-Brown and Twiss interferometry [15], which is traditionally used to investigate the fireball at kinetic freeze-out. The cluster coalescence process is nothing else but an  $A$ -body correlation and provides an important complimentary access to the freeze-out parameters. Both methods share the same variables: source size, density and dynamics at kinetic freeze-out.

In the coalescence picture the cluster momentum distribution is related to the proton momentum distribution (here in the invariant form, see Appendix A) as

$$E_A \frac{d^3 N_A}{d^3 p_A} = B_A \left( E_p \frac{d^3 N_p}{d^3 p_p} \right)^A \quad \text{with } p_p = p_A/A, \quad (1.10)$$

where in general it is assumed that the momentum distribution of neutrons has the same shape as the proton momentum distribution. The proportionality constant  $B_A$  is called Coalescence Parameter. This is at first purely phenomenologic and expresses in some way the probability that  $A$  nucleons close in momentum space merge to form a cluster of mass number  $A$ . So  $B_A$  serves as a common parameter to characterize the measured cluster production.

Large cluster yields were observed already at the beginning of heavy-ion physics at Bevalac and in the following at AGS at the Brookhaven National Laboratory. This triggered the development of several different theoretical descriptions of the coalescence process and various interpretations of  $B_A$  [16, 17, 18, 19, 20, 21, 22, 23]. The models relevant for the understanding and the interpretation of cluster results will be discussed in the following sections.

### 1.2.1 Coalescence Models I: Classical Statistics

Looking at the details of the coalescence process, one has to include in general a *third body* to carry away the excess binding energy, for example a pion as catalyst for deuteron coalescence  $p + n + \pi \rightarrow d + \pi$ . In the early coalescence models the whole system was used as third body. Indeed, Butler and Pearson [16] suggested deuteron formation in proton-nucleus collisions as a binding of cascade nucleons in the presence of the target nuclear optical potential. However, in the rather violent relativistic heavy ion collisions, a static

nuclear optical potential loses its meaning.

Scharzschild and Zupančič [17], extended by Gutbrod et al.[18], used a purely statistical ansatz, where  $A$  nucleons within a sphere of radius  $p_0$  in momentum space merge to form a cluster. The probability to find a nucleon in the momentum sphere is

$$P = \frac{1}{M} \frac{4\pi}{3} p_0^3 \left( \gamma \frac{d^3 N_N}{dp^3} \right), \quad (1.11)$$

where  $M$  is the mean number of nucleons in the system and  $\gamma \frac{d^3 N_N}{dp^3}$  the Lorentz-invariant nucleon momentum distribution. Now, the statistical probability to find  $A$  nucleons in this sphere is given by

$$P_M(A) = \binom{M}{A} P^A (1 - P)^{M-A}. \quad (1.12)$$

In the case of large nucleon numbers and small clusters, i.e.  $M \gg 1$  and  $M \gg A$ , as well as a small mean number of nucleons in the sphere,  $MP \ll 1$ , the previous equation can be reduced to

$$P_M(A) = \frac{(MP)^A}{A!}. \quad (1.13)$$

Hence, using Equation 1.11 yields

$$\gamma \frac{d^3 N_A}{dp_A^3} = \frac{1}{A!} \left( \frac{4\pi}{3} p_0^3 \right)^{A-1} \left( \gamma \frac{d^3 N_N}{dp^3} \right)^A \quad (1.14)$$

with the cluster momentum  $p_A = Ap$ . Taking spin and isospin into account, the coalescence parameter can therefore be written in this picture as

$$B_A = A \frac{2s_A + 1}{2^A} \frac{R_{np}^N}{N!Z!} \left( \frac{4\pi}{3} \frac{p_0^3}{m} \right)^{A-1}. \quad (1.15)$$

Here,  $R_{np}$  is the ratio of neutrons and protons in the source,  $N$  and  $Z$  are the neutron and proton numbers of the cluster with spin  $s_A$  and  $m$  is the proton mass.

This statistical picture made no assumptions on the details of the coalescence process itself and therefore does not account for the problem of energy conservation. Accordingly, it has no predictive power on the parameter  $p_0$ , which is extracted from fits to the data. In addition,  $B_A$  contains no dependence on the collision system besides  $R_{np}$  and is only linked to the momentum difference of the constituent nucleons, unique for a given cluster species. Nevertheless, this simple coalescence picture worked quite well for intermediate energy  $AA$  collisions as well as  $pA$  and  $pp$  collisions in the whole energy range, where indeed nearly constant coalescence parameters were observed ( $B_2 \approx 2 \cdot 10^{-2} \text{GeV}^2 c^{-3}$  and  $B_3 \approx 2 \cdot 10^{-4} \text{GeV}^4 c^{-6}$ ).



First deviations from a constant coalescence parameter for the different systems were observed in  $AA$  collisions at AGS, where  $B_A$  decreased by more than a factor of five compared to the average given above. This led to the conclusion, that in these collisions at larger energy, the reaction volume needs to be taken into account. Unlike in low energy  $AA$  and  $pp$ ,  $pA$  collisions where the reaction volume is of similar size as the cluster itself and  $B_A$  only related to the intrinsic cluster parameter  $p_0$ , the reaction volume in  $AA$  at higher energies is considerably larger. That means, nucleons close in momentum space are not necessarily close in coordinate space, and  $B_A$  becomes thus sensitive to the source size at freeze-out.

Mekjian proposed to apply the thermodynamical description of the hadronization to the coalescence process [19], following the earlier idea of Hagedorn of a statistical deuteron production in  $pp$  collisions [24]. Applying Equation 1.8 in the Boltzmann limit,

$$\frac{d^3 N}{dp^3} = \frac{gV}{(2\pi)^3} \exp\left(-\frac{E - \mu}{T}\right), \quad (1.16)$$

to both the cluster and constituent nucleons and a cluster chemical potential of  $\mu_A = N\mu_n + Z\mu_p$  in a thermal and chemical equilibrated volume, one can conclude directly that

$$B_A = A \frac{2s_A + 1}{2^A} R_{np}^N \left(\frac{(2\pi\hbar)^3}{mV}\right)^{A-1}. \quad (1.17)$$

The thermodynamic parameters  $V$ ,  $T$  and  $\mu$  in Equation 1.16 are now investigated at the time of clusterization, i.e. at the kinetic freeze-out of the fireball, instead of the chemical freeze-out studied by the hadron chemistry model. Here,  $B_A$  depends on the source volume as  $B_A \propto (1/V)^{A-1}$  and is therefore able to provide an explanation for the decreasing coalescence parameter observed on increasing collision energy in  $AA$  collisions (see Chapter 7.3).

This thermodynamic ansatz again makes no assumption on the details of the coalescence mechanism, but assumes thermal and chemical equilibrium, as introduced in the previous section. Mekjian tried to justify this picture by comparing the deuteron reaction rates to the typical time scales of the fireball evolution. Here, a different interpretation of the thermodynamic coalescence model is proposed. Following the argumentation given above for a thermodynamic hadronization process, the clusterization process is also phase-space dominated, and clusters freeze out chemically into a state of maximum entropy, as well. Hence, clusters are in the same way born into thermal and chemical equilibrium at kinetic freeze-out as hadrons at chemical freeze-out of the fireball.

## 1.2.2 Coalescence Models II: Quantum Statistics

Quantum statistical [21, 22, 23] approaches to the coalescence process are based on the density matrix formulation. The number of created clusters in this model is determined by the projection of the cluster density matrix onto the  $A$ -nucleon density matrix in the fireball taken at the freeze-out time. Unlike the classical approaches, the quantum mechanical description can take the internal cluster structure and energy conservation into account. Sato and Yazaki [21] even refrain from assuming thermal and chemical equilibrium of the cluster source. However, none of these models, besides the recent framework of Scheibl and Heinz [23], account for the strong collective expansion dynamics observed in relativistic heavy ion collisions and will therefore be no further discussed in this thesis.

Scheibl and Heinz incorporate in their coalescence model formulation a dynamically expanding source in both transverse and longitudinal direction, motivated by hydrodynamics. As they assume also a local thermal and chemical equilibrium, the coalescence parameter is in its form identical with the classical result in Equation 1.17 — modified only by a quantum mechanical correction factor  $\langle \mathcal{C}_A \rangle$  and a replacement of the source volume in coordinate space  $V$  by an effective volume  $V_{eff}$ ,

$$B_A = A \frac{2s_A + 1}{2^A} \langle \mathcal{C}_A \rangle \frac{V_{eff}(A, M_t)}{V_{eff}(1, m_t)} \left( \frac{(2\pi\hbar)^3}{m_t V_{eff}(1, m_t)} \right)^{A-1}. \quad (1.18)$$

Here, the cluster transverse mass  $M_t$  (see Appendix A) is related to the nucleon transverse mass as  $M_t = Am_t$ . The effective volume  $V_{eff}$  now explicitly depends on the mass number  $A$  and the transverse momentum as a consequence of transverse collective flow. Using the similarity of coalescence and HBT, Scheibl and Heinz find an expression of the effective volume in terms of the HBT radii  $R_\perp$  and  $R_\parallel$  as

$$V_{eff}(A, M_t) = \left( \frac{2\pi}{A} \right)^{3/2} R_\perp^2(m_t) R_\parallel(m_t). \quad (1.19)$$

In the language of HBT,  $V_{hom}(m_t) = R_\perp^2(m_t) R_\parallel(m_t)$  is interpreted as “volume of homogeneity”, i.e. the fraction of the fireball where particles with given momentum are emitted. It is remarkable, that this determines also the coalescence probability. The quantum mechanical correction factor  $\langle \mathcal{C}_A \rangle$  is related to the intrinsic cluster size.

Polleri showed [25], that cluster yields are also very sensitive to the transverse nucleon density profile and in the case of transverse collective flow a box-like nucleon density profile is phenomenologically preferred. Scheibl and Heinz confirmed this result and Equation 1.18 therefore becomes for  $A = 2$  and 3

$$B_2 = \frac{3\pi^{3/2}\hbar^3 \langle \mathcal{C}_d \rangle}{2m_t V_{hom}(m_t)} e^{2(m_t - m)(1/T_p^* - 1/T_d^*)} \quad (1.20)$$

and

$$B_3 = \frac{2\pi^3 \hbar^6 \langle \mathcal{C}_{t,3He} \rangle}{\sqrt{3} m_t^2 V_{hom}^2(m_t)} e^{3(m_t - m)(1/T_p^* - 1/T_{t,3He}^*)}, \quad (1.21)$$

where  $T_i^*$  is the inverse slope parameter of a Boltzmann fit to the transverse mass spectrum of particle species  $i$  (see Chapter 7).

The results of the light antinuclei analysis presented in this thesis will be discussed in terms of both the classical thermal model, as well as the quantum statistical formulation of Scheibl and Heinz. As shown above, this allows to interpret the source volume extracted from coalescence in terms of the homogeneity volume and to compare this to HBT results for identical hadrons.



# Chapter 2

## The STAR Experiment

The Solenoidal Tracker At RHIC (STAR) is one of five experiments currently set up at RHIC. It is designed as a large-acceptance hadron-detector capable to detect a large fraction of the produced hadrons in central heavy-ion collisions at RHIC's top energy of  $\sqrt{s_{nn}} = 200$  GeV. It is also intended to study polarized proton-proton collisions. That way, one can estimate the gluon spin contribution to the total spin of the proton. STAR can furthermore be used to examine ultra-peripheral Au-Au collisions, in which the passing ions interact only through photon and pomeron exchange, originated by the intense electric field of the ions [26]. Additionally, proton-proton and proton-nucleus interaction data will serve as a reference for heavy-ion studies. The STAR detector is able to handle the wide particle multiplicity range of those different programs from a few tracks — usually less than ten, seen in an ultra-peripheral Au-Au collision — reaching up to several thousands seen in a central collision.

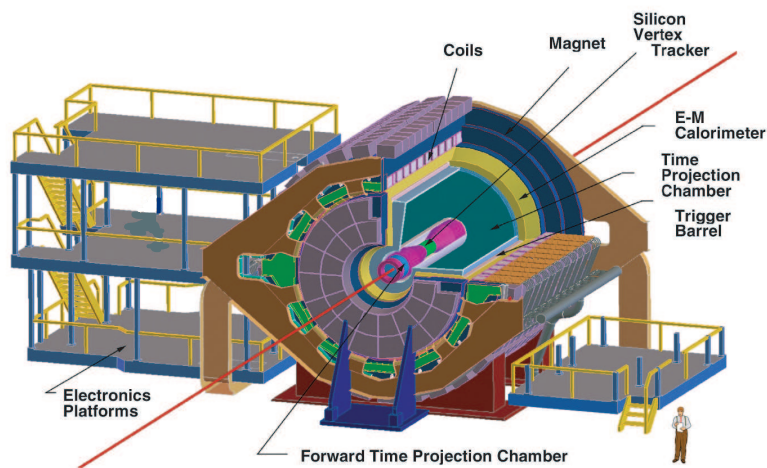
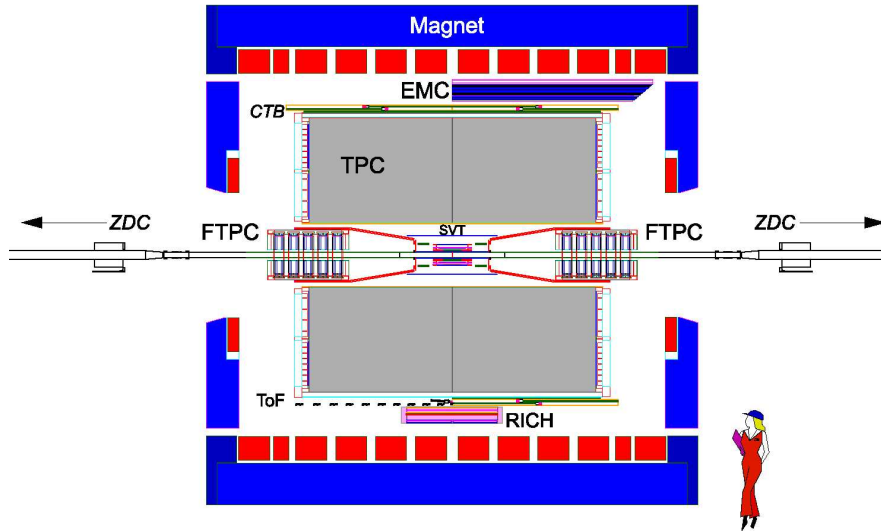


Figure 2.1: Perspective view of the STAR detector.

STAR features detector systems for high-precision tracking, momentum analysis and particle identification at the center-of-mass rapidity.

Figure 2.1 shows a perspective view of the STAR detector. The main component is a large Time Projection Chamber (TPC) covering the pseudorapidity range  $|\eta| \leq 1.8$  as well as the full azimuthal angle. A Ring-Imaging-Cherenkov (RICH) detector placed at center-of-mass rapidity provides particle identification capabilities far to the high momentum region. Additional subsystems of STAR are Forward Time-Projection-Chambers (FTPCs) to reconstruct particles in the forward-rapidity range, a Silicon-Vertex-Tracker (SVT) allowing particle tracking close to the main interaction point and an Electromagnetic Calorimeter (EMC). These subsystems are housed by a solenoidal magnet providing a homogeneous field parallel to the beam axis for momentum analysis.



**Figure 2.2:** Schematic side view of the STAR detector configuration of the year 2001 running period.

A schematic side view of the year 2001 configuration of the STAR detector is shown in Figure 2.2.

In preparation of the 2001 running period the FTPCs, the SVT and part of the EMC were added to the already existing system. Furthermore, a small Time-of-Flight (TOF) patch was installed for a first test of this detector system. In the 2001 run the RHIC facility delivered Au beams at  $\sqrt{s_{nn}} = 200$  GeV for the first time.

This chapter shall give an overview on the main components of the STAR detector, followed by a description of the low level triggers used in the 2001 run plus a brief introduction to the RHIC facility.

## 2.1 The Magnet

The design of the magnet was dominated by the goals of the STAR physics program. Primary design requirements were set by the momentum measurement of high-energy particle tracks, which are nearly straight, as well as the field uniformity crucial for the precision of position measurements in the detector system. The magnet provides an extremely homogeneous field parallel to the beam axis with a strength up to 0.5 T. This condition simplifies momentum reconstruction as charged particle tracks in the TPC follow mostly a helix.

The magnetic field was thoroughly mapped at a field strength of 0.25 and 0.5 T using a steerable array of Hall probes with a precision of about 1 – 2 Gauss. The uniformity at full field strength was determined to be better than  $\pm 50$  Gauss in radial direction and  $\pm 3$  Gauss in azimuthal direction. This setup allows to calculate the distortion effects on tracks in the TPC with a precision of approximately 200 – 300  $\mu\text{m}$ . A detailed description of the magnet can be found in [27].

## 2.2 The Time Projection Chamber

The main tracking detector of STAR is a large Time Projection Chamber, which measures tracks and momenta of charged particles and provides particle identification by detecting the ionization energy loss  $dE/dx$  along the particle trajectory. It can so be considered as a large 3D digital camera with a corresponding number of 70 million pixels, which records very detailed pictures of high multiplicity heavy-ion collisions.

Since this thesis is based on the analysis of TPC data, the following section shall give a short summary about the design and functionality of the STAR TPC. A detailed description can be found in [28], the standard reference for Time Projection Chambers is [37].

The TPC is centered around the main interaction point with full azimuthal coverage around the beam line. Figure 2.3 shows the TPC schematically. It measures 4.2 m in length and 4 m in diameter, where the active tracking volume starts at an inner radius of 0.5 m. At full magnetic field all particles with a transverse momentum exceeding 100 MeV/c and pseudorapidity between  $-1.8$  and  $1.8$  enter the chamber. The central membrane (labeled as *high voltage membrane* in Figure 2.3), separates the detector into two parts. Each half is then divided into twelve sectors similar to a clock.

The TPC is an empty box of cylindrical shape filled with a gas mixture of methane and argon (P10: 10% methane and 90% argon) in a clearly defined uniform electric field of approximately 135 V/cm. Charged particles passing through here ionize the gas molecules about every tenth of a millimeter. These secondary electrons drift in the electric field to the nearest end-cap of the TPC,

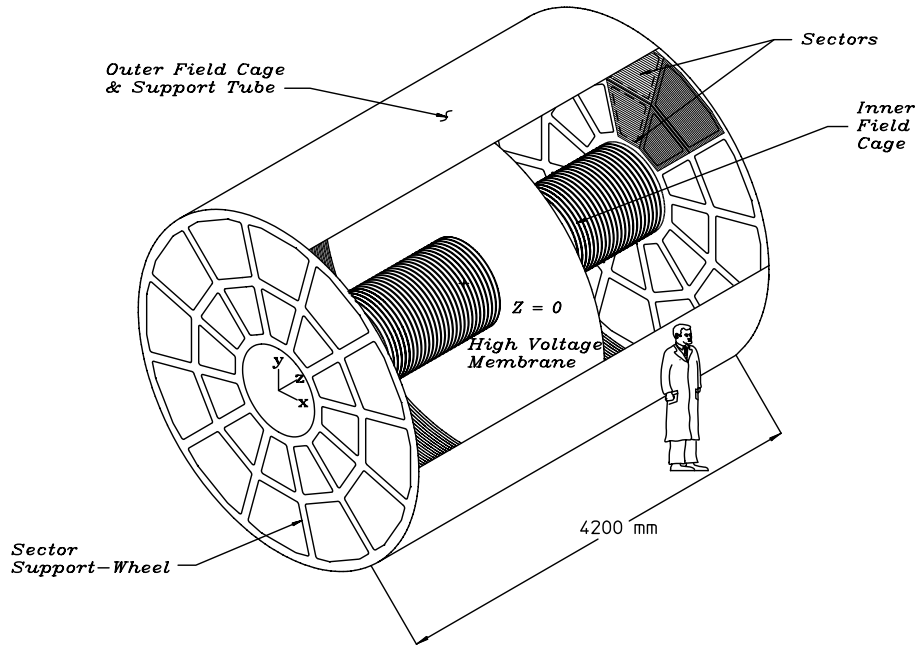


**Figure 2.3:** Schematic view of the STAR TPC. The detector is divided into two halves by the high voltage membrane and twelve sectors on each side.

where the signal is read out by a system based on a Multi Wire Proportional Chamber (MWPC) design. Field uniformity is crucial for the precision of the measurements, since the drift length of the electrons can be up to two meters. The electric field is generated by the central membrane, operated at a potential of 28 kV, the inner and outer field cage and the grounded end-caps. A constant field gradient is insured by the equi-potential rings of the inner and outer field cages. The drift velocity of the electrons was measured at  $5.45 \text{ cm}/\mu\text{s}$ . The operating parameters of the TPC, i.e. electric field and pressure, were set to reach a maximum stability for the running condition: Through several days the variation of the drift velocity was less than  $0.01 \text{ cm}/\mu\text{s}$  and less than  $0.001 \text{ cm}/\mu\text{s}$  during the time period of one run.

A schematic cross-section view of the read-out system is illustrated in Figure 2.4. It shows the three wire planes, which open or close the TPC read-out system and amplify the electron signal, as well as the pad geometry of the inner and outer subsectors described below.

The first wire plane is the so-called "Gating Grid". It can be seen as the shutter of this high resolution digital camera. The shutter is open and drifting electron clouds are able to enter the read-out system, when all wires are set



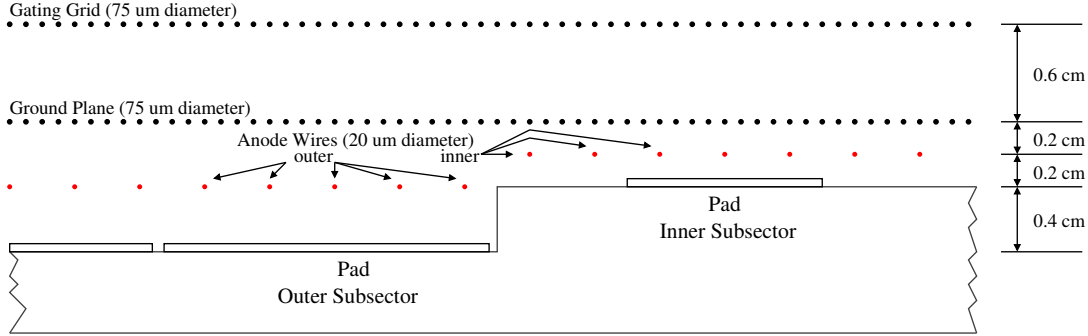


**Figure 2.4:** Schematic cross-section view of the TPC read-out plane.

to the same potential (typically 110 V). Setting the wires to alternating  $\pm 75$  V of the nominal value closes the shutter and cleans the read-out plane for the next “picture”. The two wire planes and the pad plane below construct the Multi Wire Proportional Chamber: The electron clouds are amplified by the anode wires and a temporary image charge is induced on the pads. This image charge is then measured by a pre-amplifier/shaper/waveform digitizer system. The Ground plane between the anode wires and the Gating grid terminates the electric field in the MWPC. Additionally, it can be pulsed to test and calibrate the pad electronics. The three dimensional picture of a particle track is then reconstructed from the signal location in the pad plane, identical with the  $x, y$ -plane, and the drift time of the signal. This, combined with the drift velocity, yields the position along the  $z$  axis.

The pad plane layout for one sector is shown in Figure 2.5. This layout is separated into an outer part with full pad coverage, optimized for the  $dE/dx$  resolution, and an inner part with smaller pad size to improve two-track and momentum resolution for low momentum tracks. With thirteen padrows in the inner subsector and 32 in the outer subsector a particle track can be sampled with up to 45 points. The total number of pads in each of the 24 described sectors of the TPC is 5692.

The precision of the particle track reconstruction is limited mainly by the diffusion of the produced electron clouds drifting to the read-out planes. This sets the scale for the read-out system in both the  $x, y$ -plane and the drift direction, i.e. sampling rate: A transverse diffusion of  $230 \mu\text{s}/\sqrt{\text{cm}}$  for the gas mixture P10 corresponds to  $\sigma_T = 3.3$  mm after a drift length of 210 cm at full magnet field. Similarly, the longitudinal diffusion for an electron cloud drifting the full length of the TPC is  $\sigma_L = 5.2$  mm. At a drift velocity of  $5.45 \text{ cm}/\mu\text{s}$  this equals a spread in drift time of approximately 230 ns FWHM. Accordingly the sampling rate of the read-out was set to 9.4 MHz.

Table 2.1, taken from [28], summarizes the parameters of the STAR TPC. The performance of the chamber will be discussed later, in the context of event

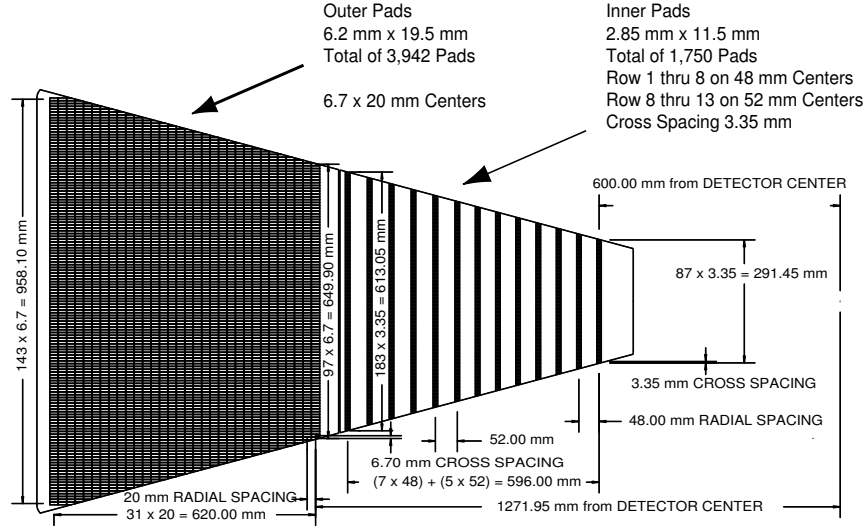


**Figure 2.5:** Anode pad plane layout of one full sector. The inner sector is optimized for two track resolution whereas the outer sector is optimized for  $dE/dx$  resolution.

reconstruction and particle identification (Chapter 5).

## 2.3 Additional Detectors

Additional detector systems in STAR extend the possibilities for particle reconstruction and identification beyond the limits of the TPC. Forward Time Projection Chambers (FTPCs) [29], located on both sides of the TPC, provide track momentum reconstruction in the forward region, pseudorapidity interval  $2.5 < |\eta| < 4.0$ , and thus improve the global event characterization, especially for asymmetric systems like p+A. The tracking inside of the TPC is extended by the Silicon Vertex Tracker (SVT), [30] consisting of three layers of silicon drift detectors. The reconstruction of short-lived particles is improved by secondary vertexing in this very high resolution detector, together with the primary vertex finding, critical for a high momentum resolution of primary tracks. Both the FTPCs and the SVT were installed and commissioned for the 2001 run.

A Ring Imaging Cherenkov Detector (RICH) [31] extends STAR's particle identification in the momentum of up to 3 GeV/c kaons and 5 GeV/c protons. Placed at the center of the TPC it covers the pseudorapidity range of  $|\eta| < 0.3$  and  $\Delta\phi = 20^\circ$ .

The Electromagnetic Calorimeter (EMC) [32] is intended to study rare, high- $p_t$  processes and photons, electrons,  $\pi^0$  and  $\eta$  mesons with pseudorapid-

Item	Dimension	Comment
Length of the TPC	420 cm	Two halves, 210 cm long
Outer Diameter of the Drift Volume	400 cm	200 cm radius
Inner Diameter of the Drift Volume	100 cm	50 cm radius
Distance Cathode to Ground Plane	209.3 cm	Each side
Cathode	400 cm diameter	At the center of the TPC
Cathode Potential	28 kV	Typical
Drift Gas	P10	10% methane, 90% argon
Pressure	Atmospheric + 2 mbar	Regulated at 2 mbar
Drift Velocity	5.45 cm/ $\mu$ s	Typical
Transverse Diffusion ( $\sigma$ )	230 $\mu$ m/ $\sqrt{\text{cm}}$	At 140 V/cm and 0.5 T
Longitudinal Diffusion ( $\sigma$ )	360 $\mu$ m/ $\sqrt{\text{cm}}$	At 140 V/cm
Number of Anode Sectors	24	12 on each end
Number of Pads	136608	
Signal to Noise Ratio	20 : 1	
Electronics Shaping Time	180 ns	FWHM
Signal Dynamics Range	10 bits	
Sampling Rate	9.4 MHz	
Sampling Depth	512 time buckets	380 time buckets typical
Magnetic Field	0, $\pm 0.25$ T, $\pm 0.5$ T	Solenoidal

**Table 2.1:** Summary of the TPC parameters, taken from [28].

ity  $|\eta| < 1.0$ . In contrast to the slow tracking detectors, the EMC will be used in the trigger. This subsystem is supposed to be completed in 2003.

Figure 2.6 shows a summary plot of the acceptance of STAR's various detector components for the 2001 run. The EMC is not enclosed in this plot, as it was not yet integrated at that time.

## 2.4 The Trigger

The trigger system of STAR splits into four levels, depending on the detector information used and on the corresponding time budget, i.e. trigger rate. The following section shall introduce the lowest level, STAR Level-0, which is the fastest and was used to trigger on the collision geometry and interaction location. A detailed description of the STAR trigger design and hardware for Level-0, 1 and 2 can be found in [33]. The highest level, STAR Level-3, will be described in the next chapter.

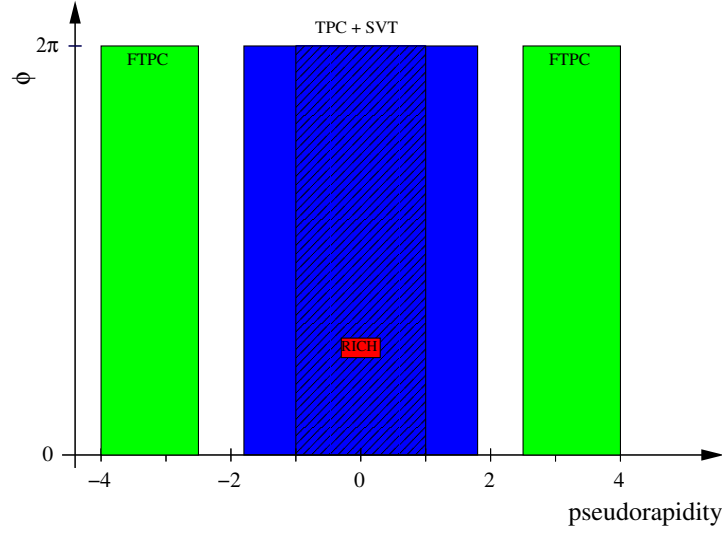


**Figure 2.6:** Acceptance of STAR's detector components shown as a function of pseudorapidity and azimuthal angle for the run 2001.

During the Au-Au run in year 2001, STAR utilized a Central Trigger Barrel (CTB) and two Zero Degree Calorimeters (ZDCs) [38] to trigger on the collisions geometry. The CTB is a scintillator array, covering the outside of the TPC, and measures the charged particle multiplicity with pseudorapidity  $|\eta| < 1.0$ . The ZDCs are placed at 18 m downstream (east and west of STAR) from the nominal interaction point at an angle close to zero degree. Positioned behind an accelerator dipole magnet they measure the energy of neutral spectator particles remaining in the forward region. All four RHIC experiments have a complement of the ZDCs to cross-calibrate the centrality trigger between them.

The correlation between the sum of the ZDC pulse heights and that of the CTB is displayed in Figure 2.7 for Au-Au events with successfully reconstructed primary vertices using the TPC tracks. Most events are in a high ZDC/small CTB signal region. Those events show a small transverse particle multiplicity and a high energy remaining in the forward region and therefore belong to collisions with large impact parameter. Collisions with progressively smaller impact parameter have less energy in the forward region, i.e. smaller ZDC signals, and more energy in the midrapidity region, i.e. higher signal in the CTB. Therefore the correlation between ZDCs and CTB pulse heights can be used to trigger on the collision geometry.

The timing information of the east and west ZDC signals by itself implies the measurement of the primary interaction location. At STAR the resolution of this method can reach  $\sigma = 3.2$  cm [39], as soon as a slewing correction is applied. Since the STAR detector acceptance as function of the primary vertex position varies, especially for the smaller detectors like SVT and RICH, the

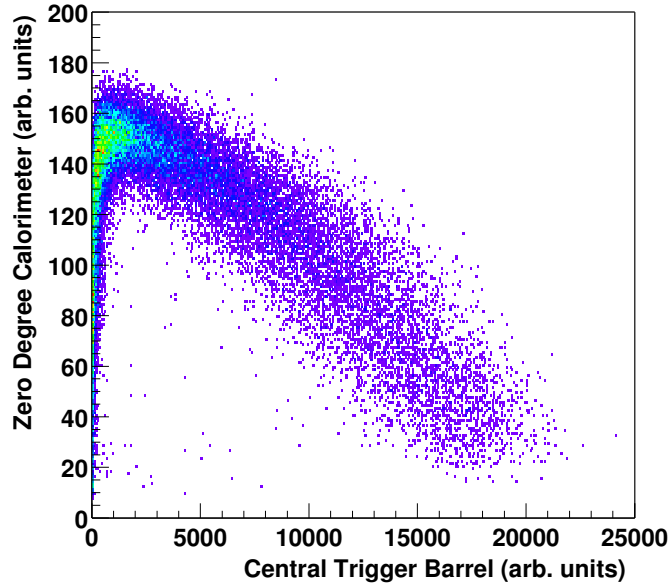


**Figure 2.7:** Correlation between the summed pulse heights of ZDCs and CTB for Au-Au events at 130 GeV/nucleon with reconstructed primary vertex using the TPC tracks.

interaction point has to be very close to the center at the collider intersection point. During the Au-Au run in 2001, RHIC delivered collisions, which spread around the nominal intersection point with  $\sigma \approx 75$  cm. Based on the ZDC information the primary vertex position was restricted in most of the trigger setups.

The hadronic minimum bias of the 2001 run trigger was defined at Level-0 as a coincidence between both ZDCs with summed signal heights above 40% of the single neutron peak. This corresponds to 95% of the geometric cross section. Smaller impact parameters were selected by requesting less energy in the forward region and a higher CTB signal to remove the second branch at low CTB. The hadronic central trigger for the 10% most central events of the 200 GeV/nucleon run applied the cuts  $\Sigma ZDCsignal < 80$  and  $\Sigma CTBsignal > 2000$  MIPS, where one minimum ionizing particle (MIP) generated a signal of five ADC counts. In addition, only events with a ZDC vertex  $|vertex_{ZDC}| < 35$  cm were selected.

## 2.5 The Relativistic Heavy Ion Collider

The Relativistic Heavy Ion Collider (RHIC) [40] was designed to collide ion beams up to a mass number of 197 (Au) with a maximum beam energy of 100 GeV/nucleon and polarized proton beams with a top energy of 250 GeV. Lighter ions and asymmetric beams can be accelerated and studied as well. The two concentric rings of the collider possess a total number of 1740 superconducting magnets and were installed in a tunnel of 3.8 km circumference. Figure 2.8 provides a schematic overview on the accelerator complex at Brookhaven National Laboratory. Some specific details on the sources and acceleration steps are also indicated. Beam collisions are possible at six intersection points, where the STAR experiment is placed at 6:00 o'clock.

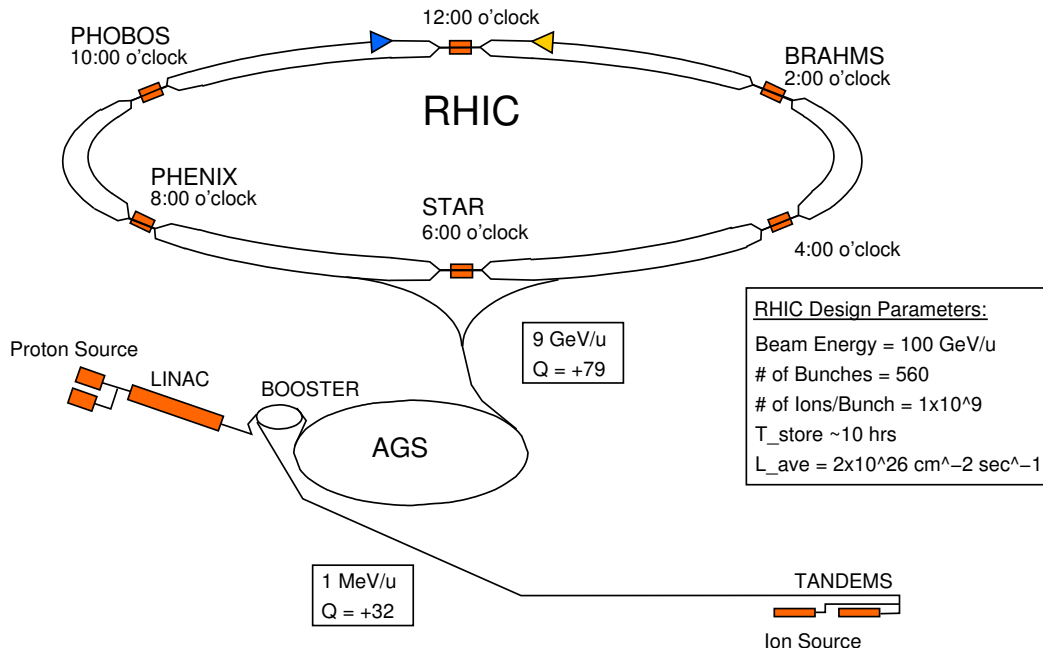


**Figure 2.8:** RHIC accelerator complex at Brookhaven National Laboratory. Ion beams are accelerated from the tandem Van de Graaf via the Booster and AGS prior the injection into RHIC. Details on the Au beam characteristic after each acceleration phase are given as well.

The gold beam is generated at the tandem Van de Graaf. This electrostatic accelerator is the source for over forty different types of ions ranging from hydrogen to uranium. Gold ions leave the tandem with a energy of 1 MeV/nucleon and partially stripped to a charge of +32, and are fed into the Booster. After 45 turns in the Booster, the kinetic energy of the gold ions reached 95 MeV/nucleon and the ions are stripped again by a 23 mg/cm<sup>2</sup>

foil to a charge +77. The Alternating Gradient Synchrotron (AGS) accelerates the beam to an energy of 9 GeV/nucleon. Prior to injection into RHIC, the gold ions are fully stripped of the remaining electrons to the charge +79. RHIC is filled with 60 bunches with about  $1 \times 10^9$  ions each. The design luminosity of the machine is  $2 \times 10^{26} \text{cm}^{-2} \text{sec}^{-1}$  with a beam lifetime of several hours. This luminosity corresponds to about 1400 minimum bias Au-Au collisions per second. For lighter systems the luminosity increases, reaching about  $1 \times 10^{31} \text{cm}^{-2} \text{sec}^{-1}$  for proton-proton collisions. High intensity proton beams are delivered by the Linear Accelerator (Linac) at a kinetic energy of 200 MeV before injected into the Booster.





# Chapter 3

## The Level-3 Trigger

As already mentioned in the previous chapter, the STAR trigger system is divided into four levels. The first three levels make use of only the fast detectors, which are read out on every RHIC bunch crossing at a rate of approximately 10 MHz. These trigger levels reduce the input rate down to the read-out rate of 100 Hz of the slow tracking detectors and trigger on global event characteristics, i.e. collision geometry. The task of the Level-3 trigger (L3) is a further reduction of the event rate, down to the available storage rate of about five events per second. The Level-3 trigger acts as an event filter based on the whole information of the tracking detectors. Performing a full online reconstruction of the event, i.e. reconstruction of about 1500 tracks in the TPC, therefore allows to trigger on physics observables, for example rare particles like  $J/\Psi$  or antinuclei. During the 2001 run only the TPC information was used, in addition to the CTB and ZDC information. The integration of the tracking detectors SVT and FTPC will be completed in preparation for the next run.

This chapter shall introduce the architecture and event reconstruction process of the Level-3 trigger. The trigger counters, crucial for a data analysis of the triggered events, shall be explained in detail. A extensive description of the Level-3 trigger and it's implementation is given in [41].

### 3.1 Architecture

The setup of the Level-3 trigger [34] is closely related to the STAR Data Acquisition (DAQ) system. The design of both systems was driven by the requirement to process events at an rate of 100 Hz, which leads to an input data rate of 20 GBytes/sec for the DAQ system. To achieve this processing rate, both systems are implemented as highly parallelized processor farms interconnected by a fast network. The L3 architecture splits into the Sector Level-3 part performing the track finding and the Global Level-3 part, which runs the trigger

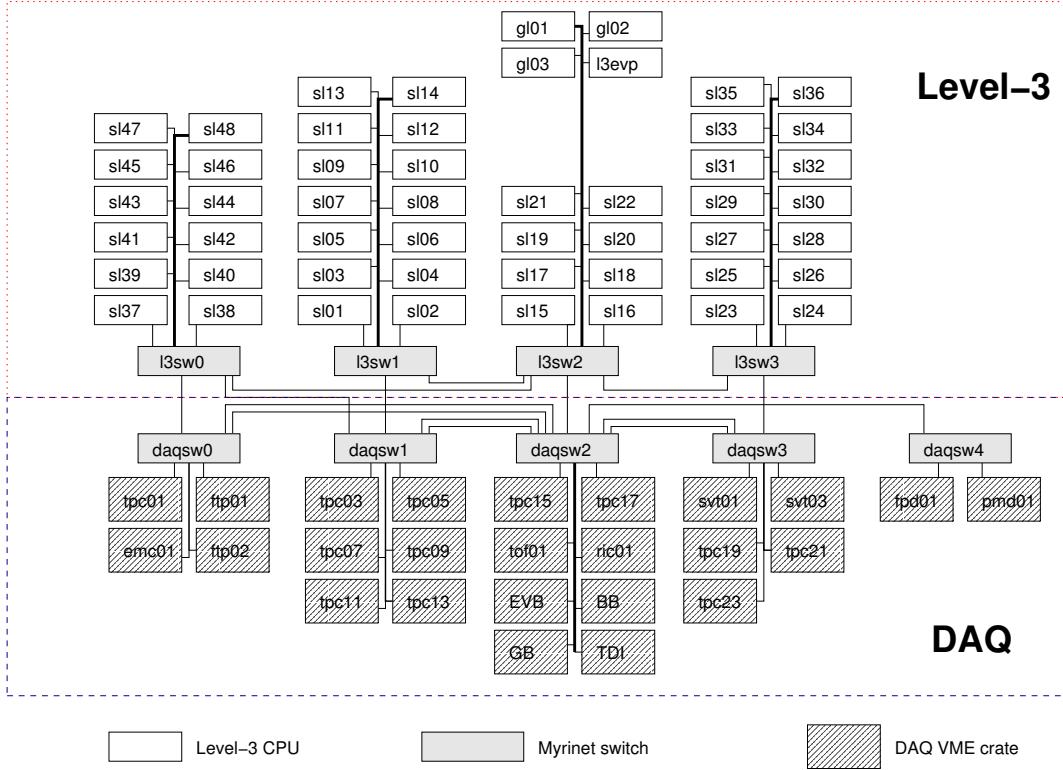


**Figure 3.1:** STAR Level-3 trigger and Data Acquisition architecture for the year 2001 data taking [34]. From top to bottom: Global Level-3 (three nodes labeled 'glXX'), Sector Level-3 (48 nodes, 'slXX') for track finding, network switches and DAQ VME crates hosting the detector receiver boards (twelve for the TPC labeled 'tpcXX' which run the cluster finder).

algorithms. The first step of event reconstruction, cluster finding, is integrated into DAQ. Figure 3.1, taken from [34], shows the setup for the year 2001 data taking. The components of DAQ and L3 will be described in the following paragraphs.

### 3.1.1 The STAR DAQ Architecture

The DAQ architecture is determined mostly by the TPC read-out electronics, which produces about 80% of the raw data volume. The DAQ systems for FTPCs and the SVT share the same architecture as the TPC part and use very similar hardware. In the context of this thesis, these parts can be neglected and only the relevant DAQ system for the TPC will be introduced. A more detailed description can be found here [35] and in the references therein.

The TPC data is digitized by the front-end electronics sitting on the detector end-caps and sent via optical fibers to the DAQ receiver boards. At the first stage of the DAQ system zero-suppression is applied to the raw data, and the cluster finding of the Level-3 trigger is performed. Six receiver boards are in place for one TPC sector, and the boards for two TPC sectors share one VME crate (in Figure 3.1 labeled as 'tpcXX'). These receiver boards carry three mezzanine cards with one Intel i960 CPU (33 MHz) and 4 MBytes dual-ported memory for buffering and pipelining raw data of twelve events on each of these cards. The i960 CPUs are used for data formatting and running the cluster finder, which will be described below. The cluster finder task for the whole TPC is therefore distributed onto 432 CPUs.

The global DAQ management is done by the Global Broker CPU, until the L3 decision is issued. The Global Broker receives the Level-0 trigger information at the same time as the data is shipped from the front-end electronics to the receiver boards and assigns Sector Level-3 processing nodes to this event. If L3 accepts the event for storage, the data is collected by the DAQ Event Builder CPU and sent to the RHIC Computing Facility, which manages the raw data storage for all RHIC experiments. Otherwise, if L3 rejects the event, the data is cleared from the receiver board buffers. See [41] for a detailed description of the DAQ/L3 event management and communication.

### 3.1.2 The Sector Level-3

The track finder task is run by the Sector Level-3 (SL3) processing farm. It consists of 48 Alpha 21264 CPUs (36 Compaq DS-10 466 MHz and 12 Compaq DS-10 600 MHz, labeled as 'slXX' in Figure 3.1), where each node can be dynamically assigned to one DAQ VME crate and the track finding in the two TPC sectors read-out by this crate. The set of 48 nodes therefore allows to process four events in parallel. Track finding in two TPC sectors consumes approximately 70 ms CPU time on an Alpha 466 MHz CPU for a central Au-Au event.

### 3.1.3 The Global Level-3

The Global Level-3 (GL3) system collects the tracking results from the SL3 nodes and issues the trigger *yes/no* decision to the DAQ Event Builder. The trigger decision is based on up to 32 different decision algorithms running simultaneously, whose results are combined by a logical OR. During the 2001 run three GL3 nodes ('glXX' in Figure 3.1) were used: a Pentium III 600 MHz, a dual Pentium III 800 MHz and a Alpha 21264 500 MHz CPU. Incoming events were distributed one-to-one onto these GL3 nodes.

Details on the trigger counters implemented in the GL3 system and the pre-

and postscaling of the trigger algorithms will be given in the next section, as they are relevant for a data analysis using L3 triggered events.

## 3.2 Pre-/Postscaling and Counters

In general, the DAQ/L3 event selection is divided into triggered, *biased* events, selected exclusively by physics algorithms, and randomly selected, *unbiased* events. These are triggered in L3 by the Pass-Thru-Algorithm (in the following called True-Algorithm), which returns a *yes*-decision for any event.

The trigger rate of each L3 algorithm can be adjusted by pre- and postscale factors. Prescaling reduces the number of (input) events seen by the algorithm, whereas postscaling reduces the number of triggered (output) events of the algorithm written to tape. Both pre- and postscaling of a trigger algorithm give the same results within statistical errors, except for the True-Algorithm, where it makes no difference. A pre-/postscale factor of 1 for the True-Algorithm prevents the enhancement of interesting events by L3, as all input events passing the reconstruction are written to tape, independent of the decision of any other algorithm. The pre-/postscale factors of the algorithms are run-time parameters and stored in the STAR database on a run-by-run basis. This way, they are also available in the STAR offline analysis framework.

In an ideal processing mode, the DAQ/L3 system stores every event on tape, which was triggered by a physics algorithm, and dynamically fills-up the remaining output bandwidth with unbiased events. This can be done by adjusting the pre-/postscale factor for the True-Algorithm according to the Level-0 input rate. However, during 2001 a dynamic scaling mechanism was not in place and the prescale factor was set to 1 for all physics algorithms and to 1, 2 or 5 for the True-Algorithm depending on the initial Level-0 trigger rate, i.e. the beam luminosity seen at the start of a run. Postscaling was not used and set to 1 for all algorithms. During 2001 the default run type for hadronic central collisions (*productionCentral*) ran without L3 trigger enhancement, a prescale factor 1 for the True-Algorithm. Correspondingly, the prescale factor of 2 (for the run type *productionCentral600*) and 5 (for *productionCentral1200*) allowed the trigger algorithms to enhance the event sample written to tape with interesting events.

For the purpose of normalization and cross section calculation the GL3 system keeps two global event counters,

- `nProcessed`, the number of processed events, i.e. all events seen so far (including *bad* events, see below), and
- `nReconstructed`, the number of events that passed reconstruction and is seen by the trigger algorithms,

and three for each trigger algorithm,

- $n_{\text{Processed}_{\text{alg}}}$ , the number of events processed by this algorithm,
- $n_{\text{Accept}_{\text{alg}}}$ , the number of events accepted by this algorithm, and
- $n_{\text{Build}_{\text{alg}}}$ , the number of events built and written to tape for this algorithm.

The difference between the global counters gives the number of *bad* events, that did not pass the L3 processing, e.g. due to missing data packets,

$$n_{\text{bad}} = n_{\text{Processed}} - n_{\text{Reconstructed}}. \quad (3.1)$$

The function of pre- and postscaling and the relation between global and algorithm counters can be illustrated with the following two equations: For a trigger algorithm the number of processed events is given by

$$n_{\text{Processed}_{\text{alg}}} = 1/\text{prescale}_{\text{alg}} \times n_{\text{Reconstructed}}, \quad (3.2)$$

and the number of events, which are built and written to tape, can be calculated from

$$n_{\text{Build}_{\text{alg}}} = 1/\text{postscale}_{\text{alg}} \times n_{\text{Accept}_{\text{alg}}}. \quad (3.3)$$

Here,  $\text{prescale}_{\text{alg}}$  and  $\text{postscale}_{\text{alg}}$  are the pre- and postscale factors of the given algorithm.

During the 2001 run each GL3 node kept it's own set of counters, independent of the other nodes, and every event written to tape contained the counter status of that GL3 node, which built the event. The total counters for each run, for example the total number of events seen by one algorithm on all GL3 nodes, were afterwards extracted during the offline calibration pass on the data and stored in the STAR database as well.

In the standard running mode during 2001, the Level-0 trigger delivered an event mix of different trigger types, e.g. hadronic central events mixed with events of the trigger for ultra-peripheral collisions. This requires special attention during data analysis, as the GL3 setup did not discriminate between the different event trigger types, but counted the total number of events. To separate the contributions to the GL3 counters, the Level-0 counters are needed. However, as no dynamic scaling was used in 2001, this can be overcome and the counters for hadronic central events can be extracted from the events on tape, without the need of Level-0 trigger counters.

The relevant counter for the data analysis, i.e. the normalization of the cross section, is  $n_{\text{Reconstructed}}$  (see Chapter 4.3), which allows to determine the number of processed events for each algorithm. Counting the unbiased hadronic central events  $n_{\text{unbiased}}$  on tape yields the counters of the True-Algorithm for this trigger type,

$$n_{\text{unbiased}} = n_{\text{Accept}_{\text{true}}} = n_{\text{Processed}_{\text{true}}}, \quad (3.4)$$

and, using Equation 3.2,

$$n_{\text{Reconstructed}} = \text{prescale}_{\text{true}} \times n_{\text{unbiased}}. \quad (3.5)$$

### 3.3 Event Reconstruction

The fast Level-3 event reconstruction process of the TPC data is very similar to the offline reconstruction described in Chapter 5. However, the L3 reconstruction is optimized for speed to achieve a high processing rate and therefore compromises resolution and efficiency. For example, an event rate of 50 Hz limits the processing time for event reconstruction and trigger decision to 200 ms, whereas the offline reconstruction process consumes more than 60 sec on a standard Intel x86 CPU. The performance comparisons of offline and L3 reconstruction, described in this section, were done with the *Embedding* technique, which will be explained in Chapter 5.4.

#### 3.3.1 Cluster Finding

The first step of the event reconstruction is the ionisation cluster finding. The ionisation of a particle track generates a two-dimensional charge signal in each padrow crossed by the track. These so-called clusters are spread over several neighboring pads and time bins. The cluster finder reconstructs the track hits in a each padrow by comparing time-bin sequences of above-threshold charge of one pad with sequences in adjacent pads of the same padrow. The hit position is defined as a mean in pad and time-bin direction, weighted by the charge measured in each pixel. The total charge sum of the cluster gives the ionisation measurement, which is needed for the calculation of the specific energy loss  $dE/dx$  of the particle track (see Chapter 5.3).

If tracks are close together the clusters may overlap. These complex clusters are split by the cluster finder along the local minima of the charge sequences in both time-bin and pad direction. Potentially merged clusters are only used for tracking and not for the  $dE/dx$  calculation, as the exact partitioning of the cluster charge between the contributing tracks is unknown. In a central Au-Au event typically 35 to 40% of the clusters are split by the cluster finder.

Figure 3.2 shows the cluster distribution in a typical AuAu event in the inner most padrow (number 1) and the outer most padrow (number 45). The symbols mark the hits reconstructed by the L3 cluster finder.

The resolution of the L3 cluster finder is very close to the resolution of the offline algorithm. Averaged over crossing and dip angles the L3 resolution is worse by only 3% [34].

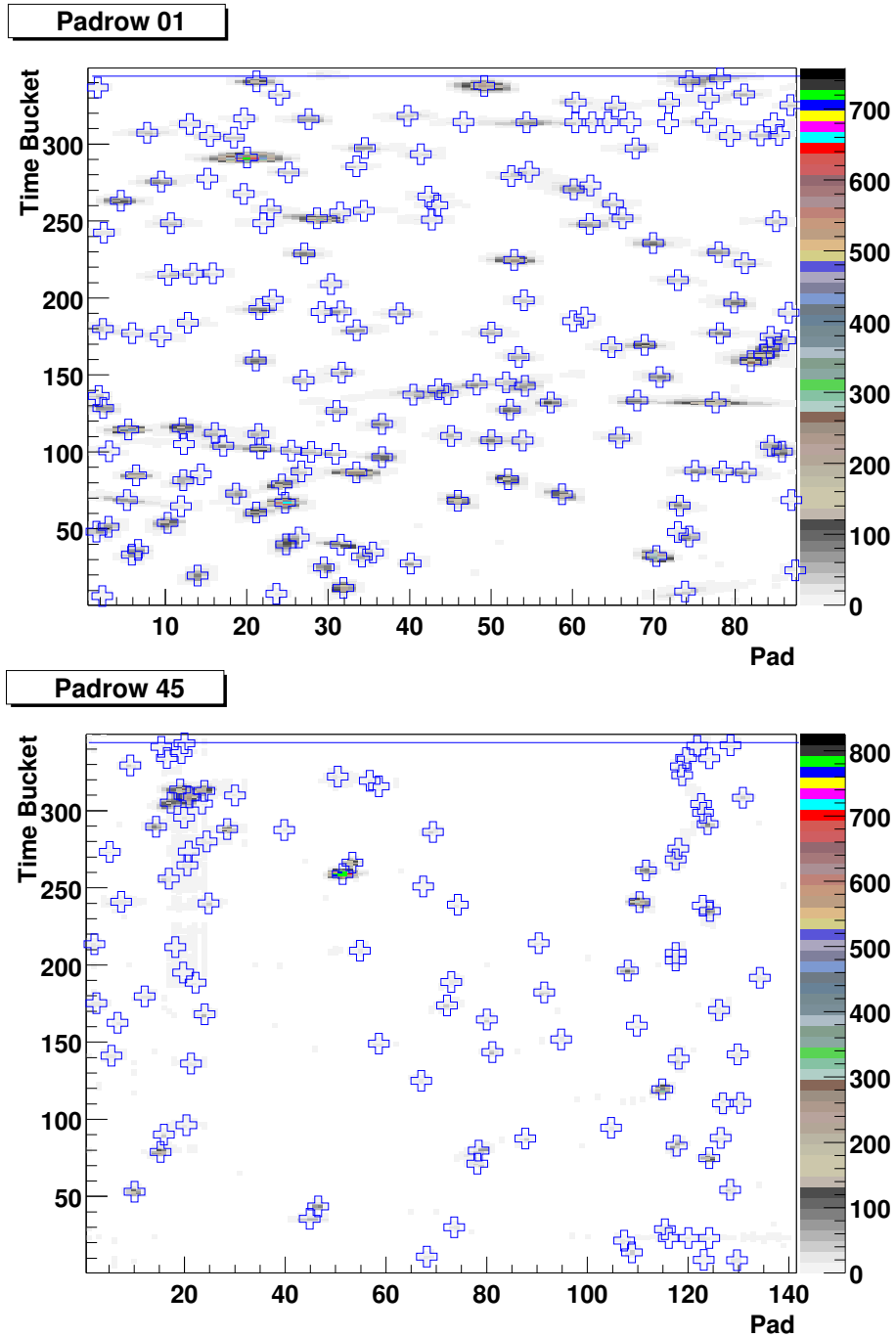


**Figure 3.2:** Level-3 cluster finder for a typical Au-Au event (here at 130 GeV/nucleon). Shown is the cluster distribution in two padrows (top: inner most row number 1, bottom: outer most row number 45), i.e. the observed charge signals in the pad/time-bin plane. The symbols mark the clusters found by the Level-3 cluster finder.

### 3.3.2 Track Finding

The second step of event reconstruction, track finding, associates first reconstructed hits (space-points) to track candidates and fits then a track model to the corresponding hit collections. This allows to extract the track information such as particle momentum. Before the tracks are reconstructed, the hit coordinates in native sector, padrow, pad and time-bin units are transformed into global Cartesian coordinates (see Appendix A). At this point the distortion corrections, for example for  $E \times B$  misalignment effects, can be applied. In L3 this is based on a look-up table, which contains the corrections obtained by the offline analysis (see Chapter 5.1.3), and can thus be done without the need of additional processing time.

The track finder algorithm [42] has been developed specifically for the L3 trigger project. It utilizes the *follow-your-nose* method with speed optimized track extension and fitting procedures, where a helix is taken as track model. By employing conformal mapping to the space-points in the transverse  $x, y$ -plane<sup>1</sup> in STAR, track reconstruction is reduced to finding straight lines in conformal space and the  $s, z$ -space<sup>2</sup>. A given space-point  $(x, y)$  is transformed into a conformal space-point  $(x', y')$  according to the equations  $x' = (x - x_0)/r^2$  and  $y' = (y - y_0)/r^2$ , whereas  $r^2 = (x - x_0)^2 + (y - y_0)^2$ . The transformation requires the knowledge of one starting point  $(x_0, y_0)$  on the track trajectory, where either the primary vertex (main interaction point) or the first point associated with the track can be used.

The helix parameters, i.e. the track information, can be extracted from the straight-line fits in conformal and  $s, z$ -space. The highest momentum resolution is achieved (see below), if a precisely known primary vertex is used in the transformation. However, the straight-line fit then fails in conformal space for secondary particle tracks, which emerge from decays and particle conversions. A greater flexibility is reached by applying an additional helix fit in real space, where both primary tracks originating from the main vertex and secondary particle tracks can be fit at the same time. The primary vertex position in the  $x, y$ -plane is well defined by the small beam size (the beam diameter is in the order of 1 mm), but along the beam line in  $z$  the vertex position is known online only with the resolution of the ZDC timing information (for central AuAu events a resolution  $\sigma_{ZDC} \approx 7$  cm without any corrections, and  $\approx 3.2$  cm with slewing correction [39]). Accordingly, the L3 track finder reconstructs the tracks using the nominal beam position in  $x, y$  as starting point in the conformal mapping, but refits the tracks in real space without the vertex

---

<sup>1</sup>A helix can be projected onto a circle in the transverse  $x, y$ -plane, perpendicular to the magnetic field axis.

<sup>2</sup>The helix parameter  $s$  is defined as the path length along the helix, measured from an arbitrary starting point. The  $z$ -axis is parallel to the magnetic field axis and the beam line in STAR, see Appendix A.



position as additional track point.

### Momentum Resolution

Figure 3.3 shows the transverse momentum resolution of both offline and L3 reconstruction for pions in central AuAu collisions with a magnetic field setting of 0.25 T (half field). This analysis was done with the embedding technique (see Chapter 5.4), whereas tracks were required to have at least 23 hits in the TPC.

For tracks fits, which do not include the primary vertex position as additional track point, the L3 resolution is up to 50% worse than the offline (*global*) track fit. As mentioned above, this was the default mode of L3 track reconstruction to allow a reasonable reconstruction of secondary tracks, e.g. in ultra-peripheral AuAu collisions. However, L3 can basically reach the same resolution as offline (within 3%), if the vertex position is included in the L3 track fit with the same precision as in the offline (*primary*) track fit.

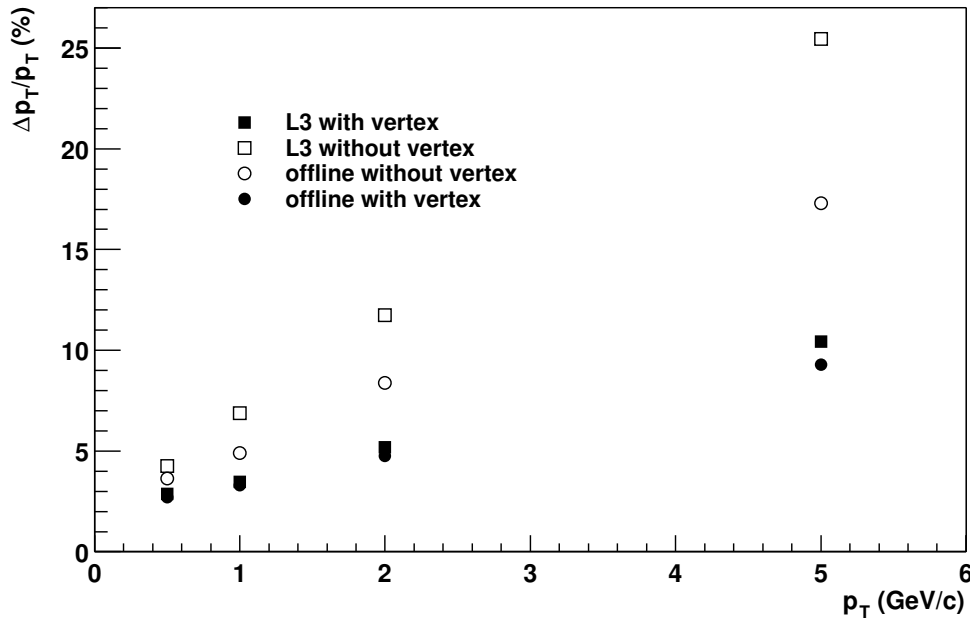


**Figure 3.3:** Transverse momentum resolution of Level-3 (squares) and offline (circles) for pions in central Au-Au collisions with a magnetic field of 0.25 T (half field). Tracks were required to have at least 23 hits in the TPC. Filled symbols show the resolution for fits, which include the primary vertex (*primary* track fit), and open symbols for fits without the vertex (*global* track fit).

## Efficiency

The detection efficiency of the TPC electronics is basically 100% and only limited by dead channels and the sector boundaries with no pad coverage. However, a finite resolution of the cluster finder and overlapping clusters reduces the tracking efficiency as a function of the collision geometry. The L3 tracking efficiency is further reduced by the TPC sector boundaries: Within the current DAQ/L3 setup, two sectors, i.e. one *supersector* corresponding to one DAQ VME-crate, are processed together on one SL3 node. Therefore, all tracks crossing the boundaries between these *supersectors* are split, including all tracks, which cross the central membrane.

The tracking efficiency as a function of transverse momentum for L3 and offline in central Au-Au events at half field is shown in Figure 3.4. For rather long tracks with at least 23 hits the effect of splitting reduces the L3 efficiency for events with a primary vertex far from the center of the detector. Then, most tracks crossing the central membrane are split into two long pieces. For events centered in the TPC, the L3 tracking efficiency reaches the offline efficiency within 5% for particles with transverse momentum  $p_t > 1$  GeV/c. During the 2001 heavy-ion run, the L0 trigger restricted the event vertex to  $\pm 35$  cm (see Chapter 6.1) and thus kept the L3 tracking efficiency close to the offline reconstruction.

### 3.3.3 Particle Identification

The particle identification, based on the specific energy loss  $dE/dx$  measured in the TPC, is available in Level-3 as well as in the offline analysis (see Chapter 5.3). The total cluster charge, summed up by the cluster finder, is converted into a ionisation measurement by taking the different amplification of inner and outer sector into account and dividing this by the track pathlength across the sensitive pad area, based on the track parameterization. Both offline and L3 reconstruction use the common *truncated mean* method to remove the Landau fluctuations of the ionisation measurements: The highest 30% of the measured ionisation samples are discarded, and the mean is calculated from the remaining 70%. Due to the time constraints, the pathlength across a padrow is approximated in L3 by a straight line, whereas the offline reconstruction uses the exact arc length. In addition,  $dE/dx$  is calculated by L3 only for tracks with at least 15 hits, adding less than 2 ms to the total processing time.

So far, the L3  $dE/dx$  is used uncalibrated, whereas the offline chain applies a gain calibration to further improve the  $dE/dx$  resolution. Since this method is only available at the offline stage, L3 could implement only a calibration *on the fly*, i.e. scaling the measured ionisation relative to a fixed value. However, already the uncalibrated  $dE/dx$  was sufficient for the trigger applications during 2001, e.g. the detection of  $Z = -2$  particles, which are clearly separated in

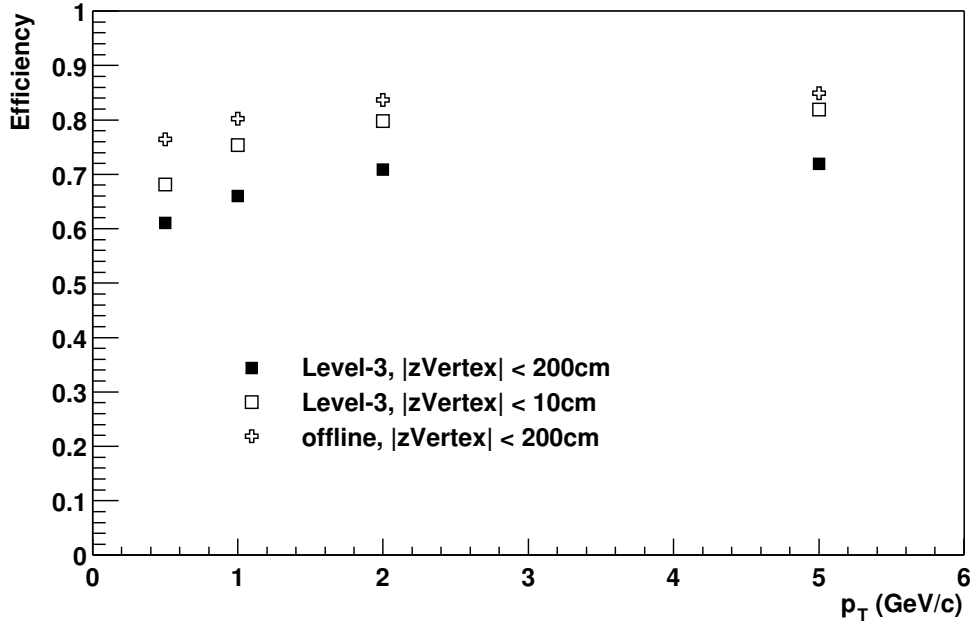


**Figure 3.4:** Tracking efficiency as a function of transverse momentum for pions in central Au-Au collisions with a magnetic field of 0.25 T (half field) and tracks with at least 23 hits in the TPC. Squares denote the Level-3 and circles the efficiency of the offline reconstruction chain.

the  $dE/dx$  spectrum (see the next chapter).

### 3.3.4 Vertex Reconstruction and Distance of Closest Approach

At the global L3 stage, the primary vertex is reconstructed to provide the trigger algorithms the information on the distance of closest approach (dca) of the tracks to the vertex. This allows to distinguish between primary tracks, originating from the primary vertex, and secondary tracks. Since no analytical solution exists for the reconstruction of the track origin in three dimensions and a time consuming numerical method would be necessary, the L3 reconstruction uses an analytical approximation: For each track, the point of closest approach to the nominal beam line at  $(0, 0)$  in the  $x, y$ -plane is taken as track origin. The primary vertex is then defined as mean of the  $x, y$  and  $z$  coordinates of the track origins. Iterating this method with the results in  $x$  and  $y$  of the previous calculation improves the resolution, but was restricted to two steps, due to the processing time constraint.

The distance between the track origin and the vertex is taken as distance of closest approach in the same way. The error of this approximation increases

for tracks with large dip angles and reaches up to 1 cm for long TPC tracks, but can be taken into account at the trigger algorithm level. The variation of the vertex in  $x$  and  $y$  is small and can be neglected in the calculation of the dca, due to the small beam size.

A comparison with the offline vertex gives a good estimate of the L3 vertex resolution. The offline vertex reconstruction is based on a numerical approximation of the track origins and reaches a vertex resolution in  $z$  of less than  $350 \mu\text{m}$  for central collisions [28]. Figure 3.5 shows the resolution in  $z$  of the L3 vertex relative to offline. The Gaussian fit yields a resolution of 0.3 cm, whereas the tail to the left side is an artifact of the method. Typical dca-cuts used in the analysis are in the order of 3 to 5 cm, the L3 vertex resolution has therefore only a small impact on the dca calculation.

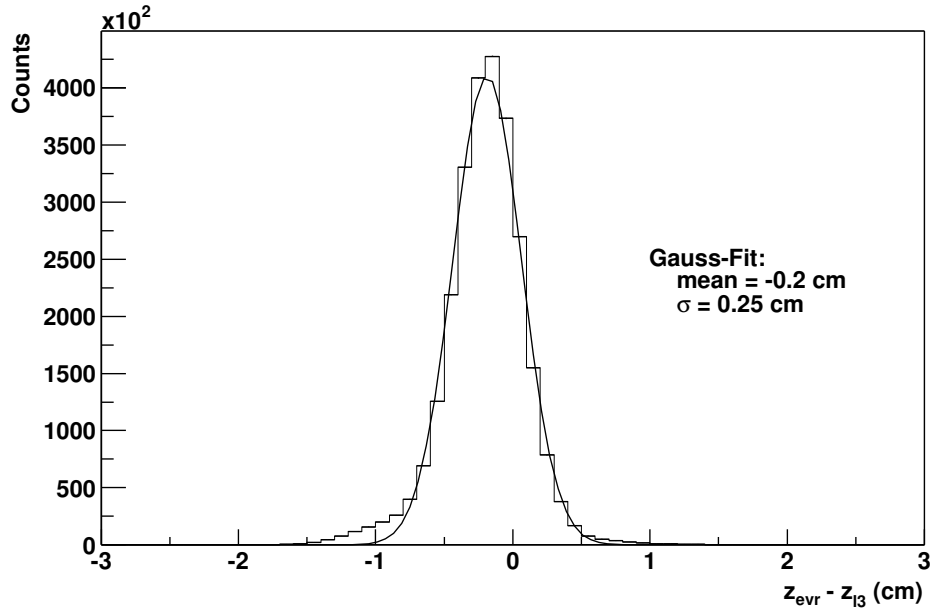


**Figure 3.5:** Level-3  $z$ -vertex resolution relative to the offline reconstructed vertex  $z_{evr}$  for central events. The shift of 0.2 cm is due to the different coordinate systems: The global coordinate system centered in the middle of the magnet is shifted with respect to the TPC coordinate system used by the Level-3 reconstruction.

# Chapter 4

## The $Z = -2$ Trigger Algorithm

The STAR Level-3 trigger is a unique tool for the study of rare signals with a large acceptance hadron detector. The full event reconstruction of L3 provides nearly the same information as the offline reconstruction and therefore allows to enhance rare signals, which are not accessible by the trigger detectors or the EMC information available to the lower trigger levels. During the AuAu run in 2001 the L3 trigger was used to trigger on rare signals for the first time. The three implemented algorithms selected events, which featured

- tracks with high transverse momentum ( $p_t > 2.0$  GeV/c) traversing the RICH detector [43],
- $\Upsilon \rightarrow e^+e^-$  candidates, reconstructed by an invariant mass calculation, or
- tracks with double negative charge ( $Z = -2$ ).

Up to 15% of the STAR DAQ storage rate was consumed by triggered, *biased* events during runs with high beam luminosity. The remaining storage rate was filled up with randomly selected, *unbiased* events, independent of the decision of the algorithms.

This chapter is dedicated to the  $Z = -2$  trigger algorithm. Double charged particles, i.e.  ${}^3\text{He}$  and  ${}^3\overline{\text{He}}$ , can be identified over almost the full momentum range by the energy loss  $dE/dx$  measurement in the TPC. However, the signal of double positive charged particles suffers from a large contribution of clusters, which are not emitted by the fireball but generated by hadronic interactions of particles in the detector material. This is not the case for the  $Z = -2$  signal, which can be extracted by the offline analysis with a signal-to-background ratio larger than 10 by applying tight track quality cuts. The  $dE/dx$  spectrum for 3.0 M central AuAu events at 200 GeV (see also Chapter 6) is shown in Figure 4.1, where a clear  ${}^3\overline{\text{He}}$  band can be seen.

The previous measurement of  ${}^3\overline{\text{He}}$  production in 130 GeV Au-Au collisions [44] of the first run of RHIC showed a rapidity density  $dN/dy$  of about  $5 \times 10^{-5}$ ,

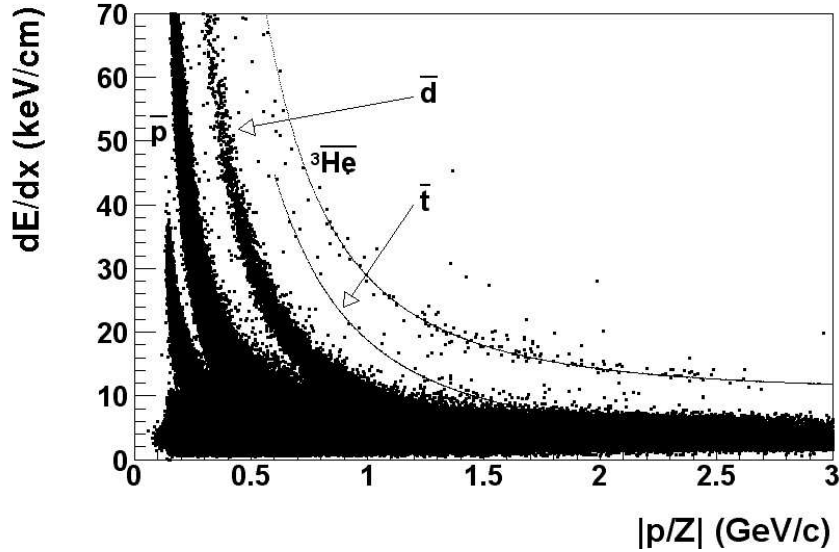


**Figure 4.1:** Energy loss  $dE/dx$  as a function of rigidity  $|p/Z|$  for negative charged particle tracks from the offline reconstruction. Included are the Bethe-Bloch expectations (see Chapter 5.3) for  $\bar{t}$  and  $\overline{{}^3\text{He}}$ .

which corresponds to a rate of approximately 50  $\overline{{}^3\text{He}}$  particles in one million central events. With the advantageous signal-to-background ratio, this rare signal represents a typical application for the Level-3 system in STAR.

The description and the results of the  $Z = -2$  trigger algorithm will be combined in this chapter, which shall first introduce the algorithm cuts, followed by the estimate of the trigger efficiency. The  $Z = -2$  signal enhancement seen in the offline analysis of the triggered events will show the *proof of principle* of the L3 trigger system. This chapter will include also a note on the normalization used in the analysis, which takes the triggered events into account.

## 4.1 Cuts

The  $Z = -2$  trigger algorithm applies basically the same cuts as the offline analysis: A cut on  $dE/dx$  for particle identification and track quality cuts to reduce background. To reach a trigger efficiency close to 100% compared to offline, these are less restrictive, compensating a weaker L3 reconstruction performance, but tight enough to keep the trigger rate of the algorithm at an acceptable level. Table 4.1 summarizes the cuts for both offline and L3. In the following, the cuts will be explained in detail. The discussion is based on those  $\overline{{}^3\text{He}}$  candidates, which were found by the offline as well as the L3 recon-

**Table 4.1:** Summary of the  $Z = -2$  cuts used in the L3 trigger algorithm and offline analysis. The event rate of candidates from the L3 algorithm and offline is given as well.

Cut	L3 Trigger	Offline
dE/dx	$0.7 < [dEdx]/I_{BB}$	$0.88 < [dEdx]/I_{BB} < 1.28$
nHits	$nHits \geq 23$	$nFitPoints \geq 30$
dca	$dca_{l3} < 7.5 \text{ cm}$	$dca_{global} < 3.0 \text{ cm}$
Rate	0.1%	<0.01%

$[dEdx]$ : measured ionisation

$I_{BB}$ : expected ionisation at the measured momentum

$nHits, nFitPoints$ : number of space-points used for the track fit (see text)

$dca$ : distance of closest approach to the main vertex

struction in about 3.0M central AuAu collisions recorded during the 2001 run period with full magnetic field.

### dE/dx Cut

The minimum  $dE/dx$  cut, shown in Figure 4.2, was set at 70% of the Bethe-Bloch expectation  $I_{BB}(p)$  for  ${}^3\overline{\text{He}}$ . In the offline analysis candidates were selected within  $3\sigma$  of the Gaussian  $Z$ -distribution (see Chapter 6.3), corresponding to a cut of  $0.88 \times I_{BB}(p) \leq [dE/dx] \leq 1.28 \times I_{BB}(p)$  in the  $dE/dx$  distribution. The L3 cut accounts for a worse  $dE/dx$  resolution, due to the shorter tracks allowed by the  $nHits$  cut (see below), and larger fluctuations in the uncalibrated  $dE/dx$ . For a possible detection of anti-alpha particles, so far never seen in an experiment, no maximum  $dE/dx$  cut was applied as a function of momentum. The  $dE/dx$  measurements for the  $Z = -2$  candidates found by the L3 reconstruction are included in Figure 4.2. The offset between the L3 measurement and the expectation seen at low rigidities is caused by the missing calibration.

### nHits Cut

The cuts on the number of space-points ( $nHits$ ) of the track and on the distance of closest approach ( $dca$ ) to the primary vertex are used to remove background in the  $Z = -2$  particle identification. The trigger rate is determined mostly by these cuts.

The  $nHits$  cut selects long tracks to assure a minimum momentum resolution and  $dE/dx$  resolution. However, a high  $nHits$  cut reduces the trigger efficiency

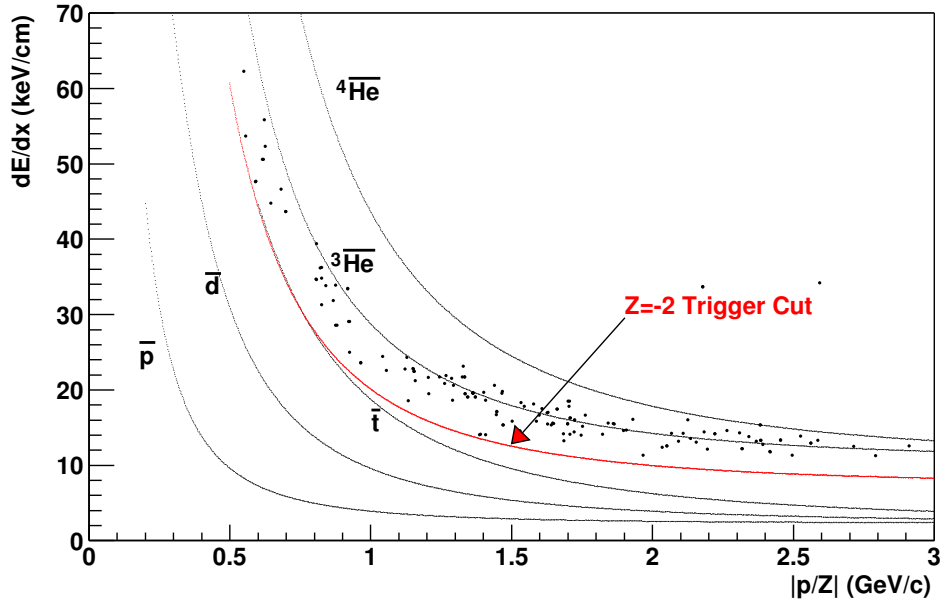


**Figure 4.2:**  $Z = -2$  trigger cut (red) in the  $dE/dx$  versus rigidity distribution. Black lines show the Bethe-Bloch curves for  $\bar{p}$ ,  $\bar{d}$ ,  $\bar{t}$ ,  ${}^3\bar{\text{He}}$  and anti-alpha ( ${}^4\bar{\text{He}}$ ). The  $Z = -2$  candidates reconstructed by the L3 algorithm are included as well.

at low transverse momenta, since the tracks are split at the *supersector* boundaries by the L3 reconstruction (see Chapter 3.3).

Figure 4.3 shows the  $nHits$  distribution for all  $Z = -2$  candidates of the L3 reconstruction, which pass the  $dE/dx$  cut. Please note, that a logarithmic scale is used on the ordinate. The enormous background originates mainly from false momentum calculation for secondary particle tracks, which do not come from the vertex (see below), and a corrupted  $dE/dx$ , caused by small space-point samples and merged clusters of tracks in close proximity.

The trigger algorithm was used with a cut of  $nHits \geq 23$ . The corresponding cut of the offline analysis was applied to the number of space-points used for the track fit (fit points), i.e.  $nFitPoints \geq 30$ . There, the primary vertex is included in the primary track fit and the space-point of pad row 13 excluded, together with outliers with large residuals (see Chapter 5.2). For L3 tracks is simply  $nFitPoints \equiv nHits$ . To judge the trigger cut, Figure 4.4 compares the distribution of number of fit points from the offline analysis to that of the L3 reconstruction. Here, only those candidates are included, which were found by both L3 and offline.



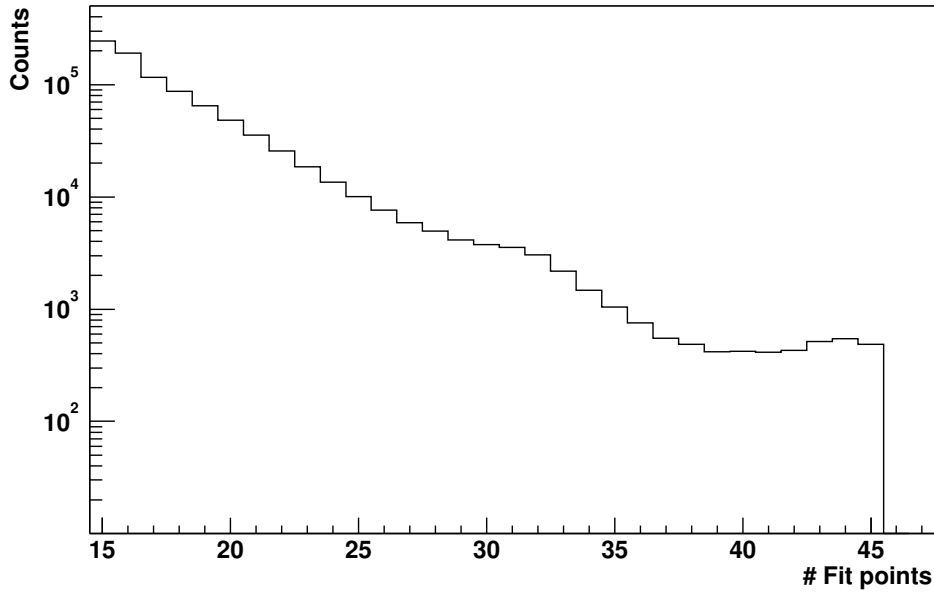


**Figure 4.3:** Number of space-points (fit points) of the Level-3 tracks passing the  $dE/dx$  trigger cut.

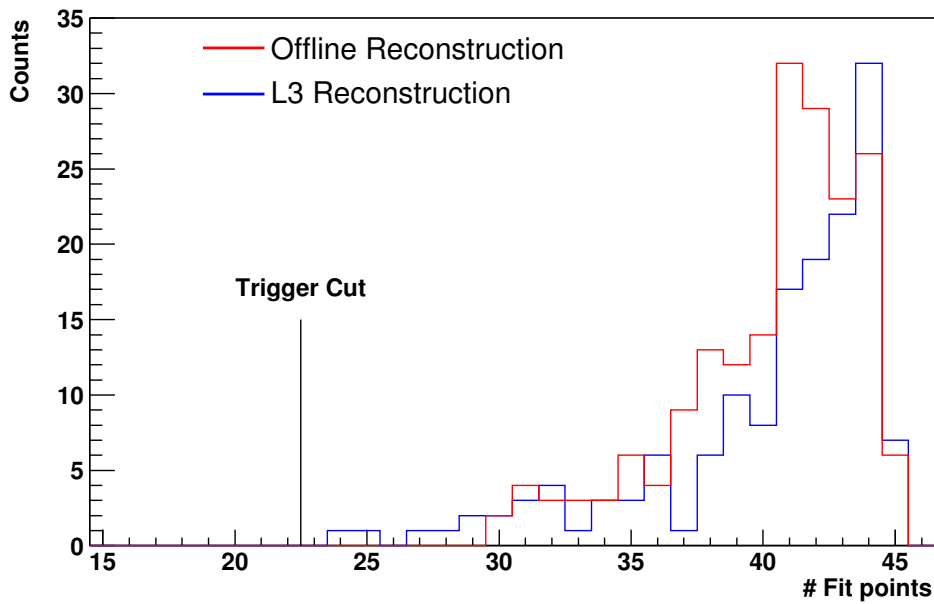


**Figure 4.4:** Number of fit points (see text) for the  $Z = -2$  candidates from the offline reconstruction (red) and Level-3 (blue). Only those candidates are included, which were found by both offline and L3. The trigger cut is set at  $nHits \geq 23$ , whereas offline requires  $nFitPoints \geq 30$ .

### dca Cut

The cut on the distance of closest approach ( $dca$ ) to the primary vertex removes secondary tracks. In Figure 4.5 the  $dca$  distribution is shown for all L3 tracks satisfying both the  $dE/dx$  and the  $nHits$  cut. The background is dominated by secondary particles with a very wide  $dca$  distribution.

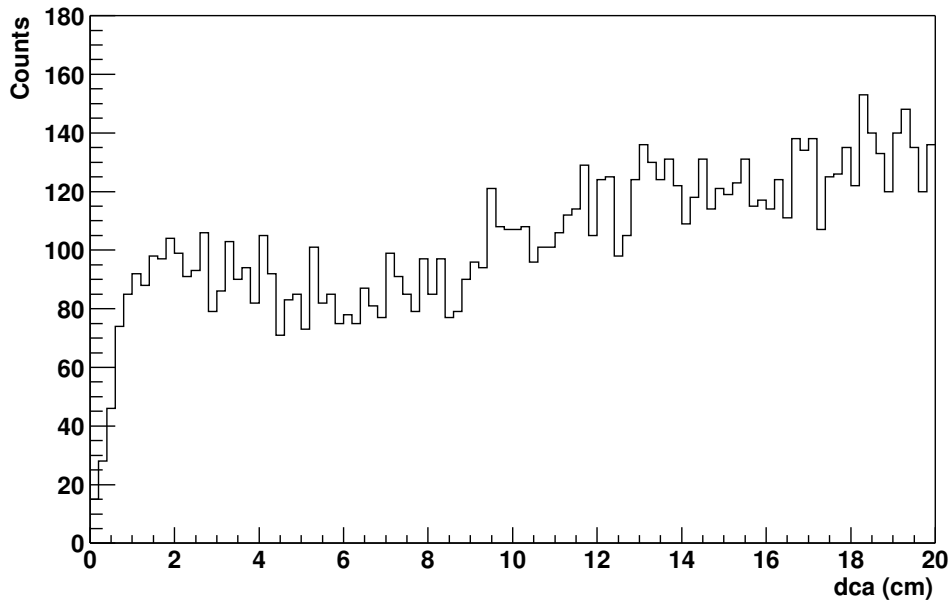


**Figure 4.5:** Distance of closest approach ( $dca$ ) of the Level-3 tracks satisfying the  $dE/dx$  and the  $nHits$  trigger cut.

To account for the uncertainty in the  $dca$  calculation of L3 (see Chapter 3.3.4), the trigger cut was kept less restrictive,  $dca_{l3} < 7.5$  cm, but nevertheless removed the largest fraction of the background. The definition of primary tracks in the offline analysis includes a cut of  $dca_{global} < 3.0$  cm, which is applied to the corresponding global track fit (again see Chapter 5.2). The  $dca_{l3}$  distribution for the L3 candidates, which match the offline found candidates, is shown in Figure 4.6.

## 4.2 Trigger Efficiency

The trigger efficiency of a L3 algorithm can be calculated either from a simulation or the unbiased event sample, relative to the offline reconstruction. The unbiased data sample with  $\approx 3.0$  M events provides sufficient statistics to extract the efficiency as a function of transverse momentum. A simulation using

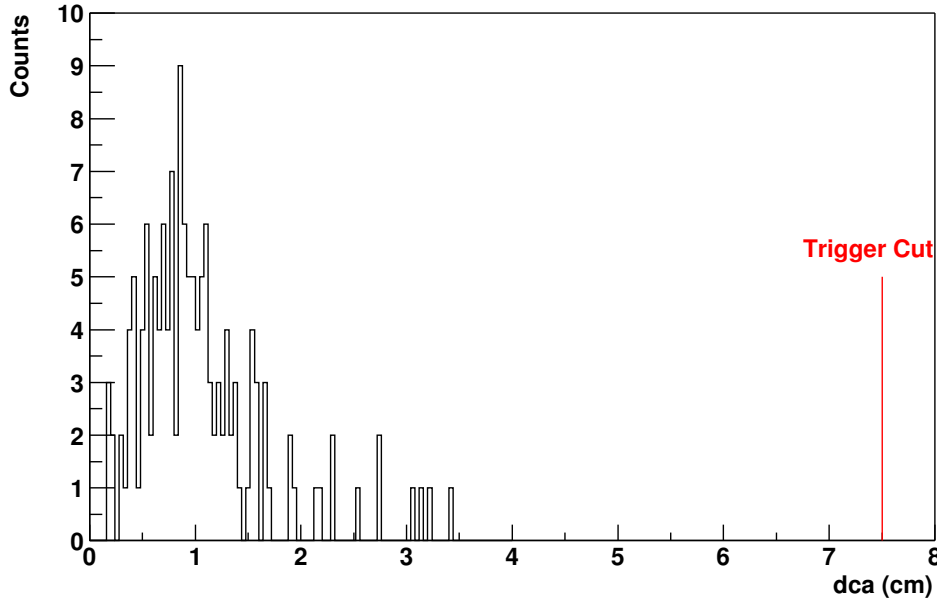


**Figure 4.6:** Distance of closest approach ( $dca_{l3}$ ) of the Level-3 tracks matching the offline reconstructed  $Z = -2$  candidates. The trigger cut is set at  $dca_{l3} < 7.5$  cm.

the Embedding technique was therefore not necessary. The trigger algorithm is used only to enhance the event sample for the rare signal extracted by the offline analysis. Accordingly, the trigger efficiency, which is defined relative to the offline reconstruction, can be applied later in the normalization of the yield extracted from both the unbiased events and the triggered events.

Based on an event-by-event comparison of the  $Z = -2$  candidates, which were found by the offline analysis and the L3 algorithm, the trigger efficiency is defined as

$$ef_{L3}(p_t) = \frac{\#RecoL3(p_{tOFF})}{\#RecoOFF(p_{tOFF})}, \quad (4.1)$$

where  $\#RecoL3$  and  $\#RecoOFF$  are the numbers of reconstructed  $Z = -2$  candidates from L3 and offline, respectively. The offline momentum is used in the nominator to avoid difficulties with the different momentum resolution of the L3 reconstruction, i.e. no requirement is made on the reconstructed momentum of the L3 candidates. Figure 4.7 shows the extracted  ${}^3\overline{\text{He}}$  raw yield as a function of offline transverse momentum for the offline reconstruction and the L3 algorithm, with the cuts given in Table 4.1. Here, only L3 candidates were counted, which match a reconstructed offline candidate in the same event. Dividing these two histograms yields the trigger efficiency,

displayed in Figure 4.8. The error bars in this plot are calculated based on *Bayesian* statistics (see Appendix B), since the standard approach is not valid for the given case of small numbers of  $\#RecoL3$  and  $\#RecoOff$  and at the limit of  $\#RecoL3 = \#RecoOff$ . The trigger efficiency reaches about 80% for  $p_t > 1$  GeV/c. Below that, the efficiency drops due to the track splitting at the boundaries of *supersectors*, as basically every track with transverse momentum  $|p_t/Z| < 0.75$  GeV/c is traversing more than one TPC sector.

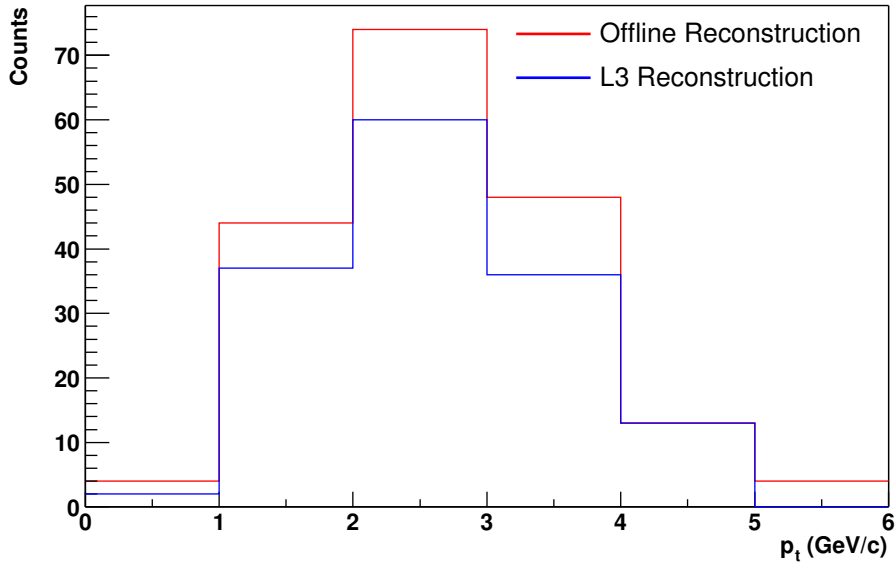


**Figure 4.7:**  ${}^3\overline{\text{He}}$  raw yield as a function of offline transverse momentum for the offline reconstruction (red) and the L3 algorithm (blue) with the cuts given in Table 4.1. Only L3 candidates are counted, which match a reconstructed offline candidate in the same event.

Unfortunately, the sample of offline  ${}^3\overline{\text{He}}$  candidates, where no matching L3 candidate was found, is not sufficient to study the trigger inefficiency in detail and to separate clearly the different contributions, such as L3  $dE/dx$  resolution or tracking efficiency. Only the distribution of  $nFitPoints$  for the  ${}^3\overline{\text{He}}$  tracks without L3 match, shown in Figure 4.9, indicates, that the shorter tracks are not found by L3.

### 4.3 Normalization

If the triggered events shall be included in the offline analysis to enhance the signal, the normalization of the yield needs to be done carefully. This section

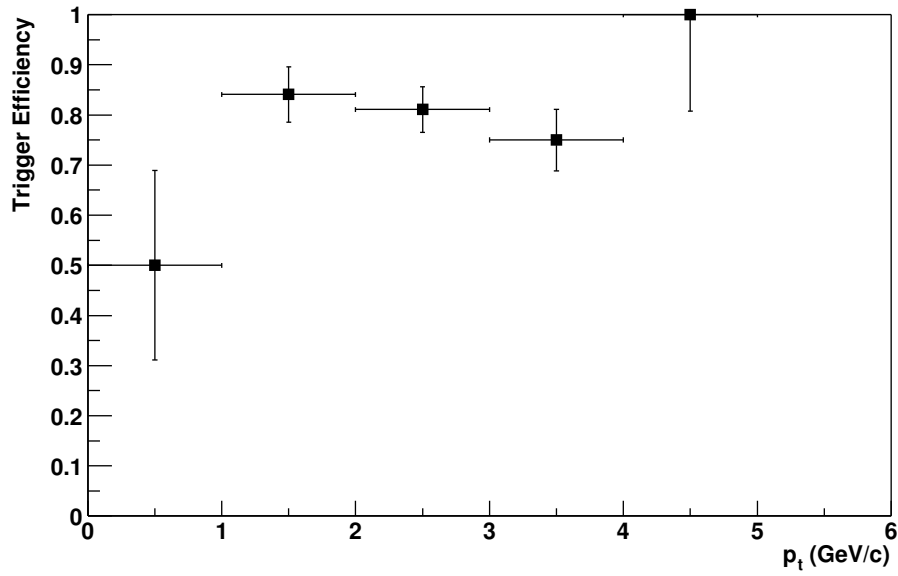


**Figure 4.8:**  $Z = -2$  trigger efficiency as a function of transverse momentum. The error bars are calculated using Bayesian statistics, the error bar of the highest bin is given as 95% lower limit.

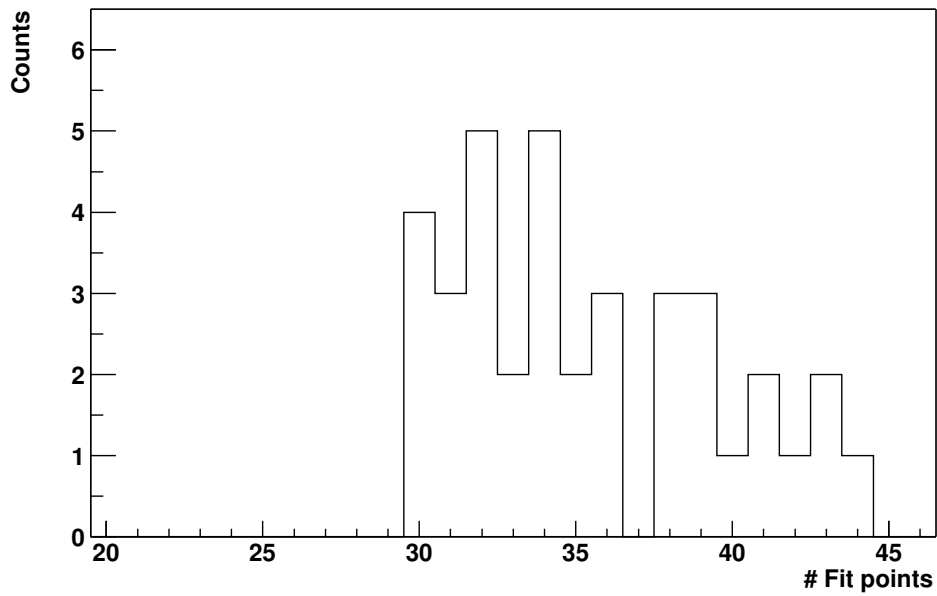


**Figure 4.9:** Number of fit points of offline  ${}^3\overline{\text{He}}$  candidates where no matching L3 candidate was found.

shall explain the details of this normalization, which is later applied to the yield extracted from both unbiased and triggered events, presented in the following section.

As the L3 trigger ran only in a mode of fixed prescaling, the necessary trigger counter can be calculated from the number of unbiased events  $n_{unbiased}$  stored on tape and seen in the offline analysis (see Chapter 3.2).

The total  ${}^3\overline{\text{He}}$  yield  $N_{total}$ , extracted by the offline analysis from both the unbiased and the triggered events, is normalized to the number of events  $n_{events}$  used in the analysis as

$$\frac{N_{total}}{n_{events}} = \frac{N_{unbiased} + N_{triggered}/eff_{L3}}{n_{unbiased} + n_{eventsL3only}} \quad (4.2)$$

with

$$N_{triggered} = N_{eventsL3only} \times eff_{L3}. \quad (4.3)$$

Here,  $N_{unbiased}$  is the yield extracted from the unbiased events and  $N_{triggered}$  the yield from the triggered events, respectively.  $n_{eventsL3only}$  gives the number of events, which were analyzed *only* online by L3 and *not* stored on tape, with the exception of the triggered events. Dividing the yield  $N_{triggered}$  from the triggered events by the trigger efficiency  $eff_{L3}$  gives the yield  $N_{eventsL3only}$ , that the offline analysis would see in those events.

The number of events  $n_{eventsL3only}$ , seen only by the trigger algorithm and not by the offline analysis, is related to the GL3 counter  $n_{Reconstructed}$ ,

$$n_{eventsL3only} = \frac{\text{prescale}_{\text{true}} - 1}{\text{prescale}_{\text{true}}} \times n_{Reconstructed}, \quad (4.4)$$

and thus to the number of unbiased events, using Equation 3.5,

$$n_{eventsL3only} = (\text{prescale}_{\text{true}} - 1) \times n_{unbiased}. \quad (4.5)$$

Here,  $\text{prescale}_{\text{true}}$  is the prescale factor of the True-Algorithm, which selects randomly the unbiased events.

Table 4.2 summarizes the number of events from the different run types of the hadronic central trigger of 2001 used in this analysis. In total, 3.3M unbiased events were recorded. The L3 trigger analyzed additional 0.7M events, about half of these with a trigger enhancement of 4, i.e., a prescale factor 5 for the True-Algorithm. Accordingly, approximately 4M events were scanned for the rare  ${}^3\overline{\text{He}}$  signal.

## 4.4 Results

In 3.36M recorded, unbiased events a  ${}^3\overline{\text{He}}$  raw yield of 193 was found. Therefore, with a  $Z = -2$  trigger efficiency of 80%, an absolute enhancement of

**Table 4.2:** Number of unbiased events and additional events analyzed by Level-3 for the hadronic central trigger (with full magnetic field setting).

run type	prescale <sub>true</sub>	$n_{unbiased}/10^6$	$n_{eventsL3only}/10^6$
productionCentral	1	2.925	0
productionCentral600	2	0.361	0.361
productionCentral1200	5	0.077	0.308
<b>total</b>		<b>3.363</b>	<b>0.669</b>

32  ${}^3\overline{\text{He}}$  particles is expected in 0.7M events scanned by L3. The offline reconstructed yield of 28 candidates from the 867 triggered events on tape is in rather good agreement with this expectation. Figure 4.10 shows the raw yield as a function of transverse momentum from the offline reconstruction of the unbiased and the triggered events. The enhancement in the  $dE/dx$  spectrum is displayed in Figure 4.11.

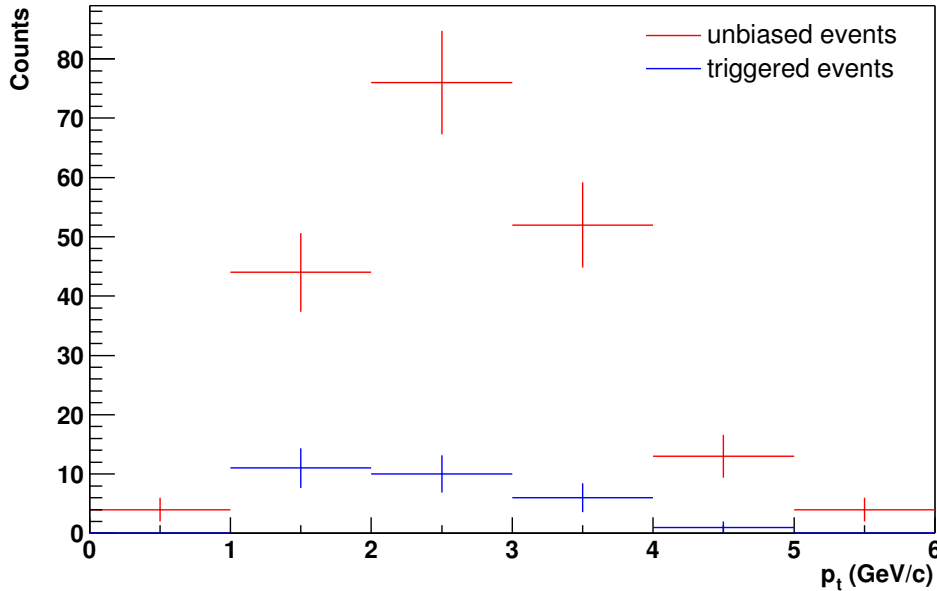


**Figure 4.10:**  ${}^3\overline{\text{He}}$  raw yield reconstructed offline from the 3.3M unbiased (red) and 867 triggered events (blue).

Finally, a comparison of the physics analysis results, with and without the triggered events included in the data sample, allows to test the capabilities of the Level-3 trigger system to improve physics observables. The details of

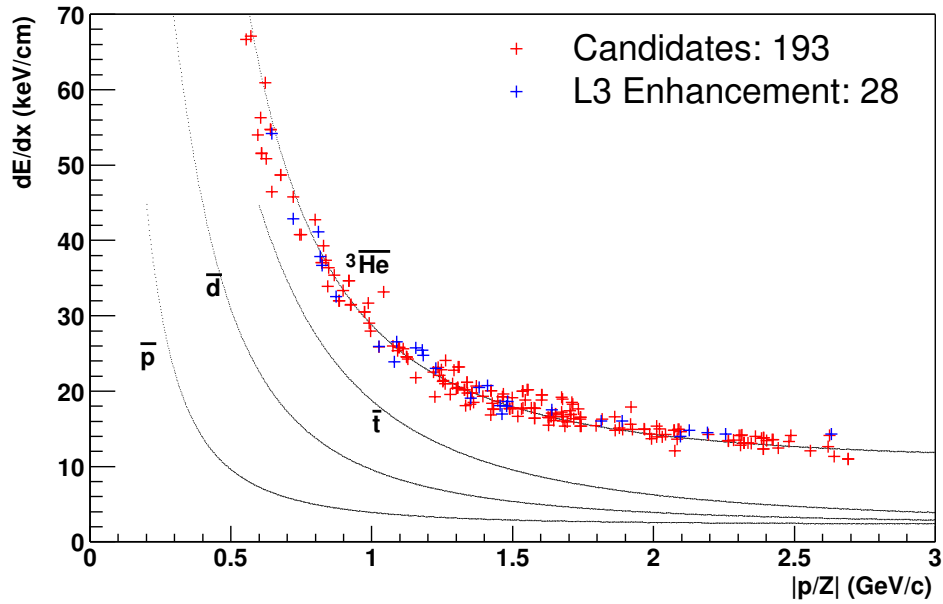


**Figure 4.11:**  $dE/dx$  distribution of the offline reconstructed  ${}^3\overline{\text{He}}$  candidates of the unbiased (red) and triggered (blue) event sample.

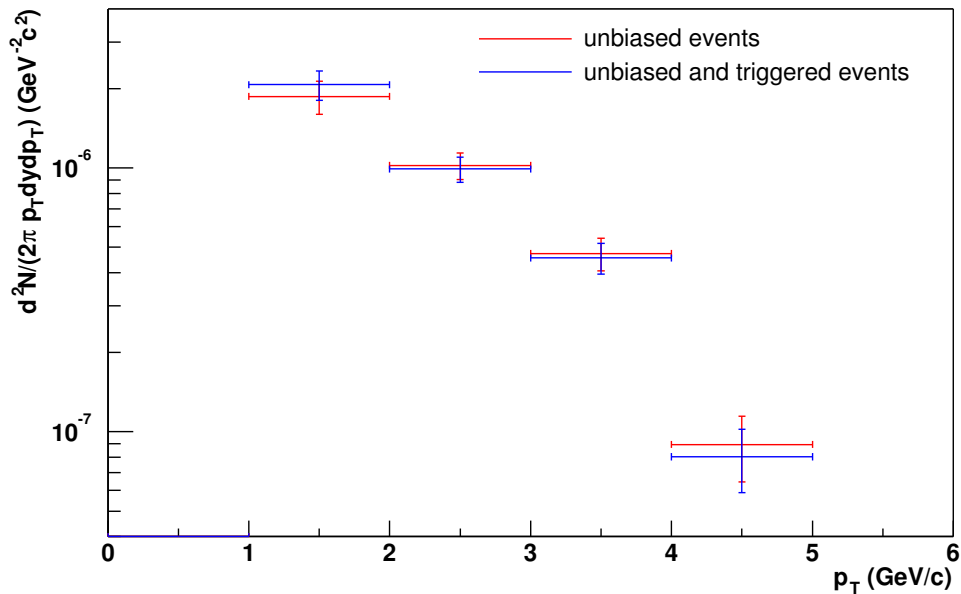


**Figure 4.12:**  ${}^3\overline{\text{He}}$  invariant yield as a function of transverse momentum reconstructed offline from the unbiased (red) and total (blue) event sample. Error bars give the statistical errors only.



the analysis of the  ${}^3\overline{\text{He}}$  transverse momentum spectrum will be described later (see Chapter 7.2), here, only the results shall be given. Figure 4.12 shows the offline reconstructed invariant multiplicity as a function of transverse momentum for the unbiased event sample and for the total event sample, where the triggered events are included. The error bars give the statistical uncertainties only. However, the uncertainty of the trigger efficiency is included for the total event sample. From the exponential fit (in the momentum range of sufficient statistics,  $1.0 < p_t < 4.0$  GeV/c) of the transverse mass distribution a rapidity density  $dN/dy$  at mid-rapidity of  $(6.24 \pm 0.50) \times 10^{-5}$  [ $(6.17 \pm 0.45) \times 10^{-5}$ ] and an inverse slope parameter  $T$  of  $(950 \pm 140)$  MeV [(865  $\pm$  115) MeV] can be extracted for the unbiased [total] event sample. Both results agree well within the statistical errors and show the capabilities of the Level-3 trigger system: With a trigger efficiency extracted from the large unbiased data set, the signal enhancement by 20% is already seen in a reduction of the statistical errors of the results.

Unfortunately, an extended use of the Level-3 trigger during the 2001 run period was prevented by the RHIC luminosity. Most of the time the corresponding Level-0 trigger rate for hadronic central collisions was equal to or smaller than the DAQ storage rate and therefore not sufficient to operate the Level-3 trigger for the enhancement of rare signals.

## 4.5 Outlook

If the beam luminosity is high enough — and the event rate higher than the DAQ storage rate — the efficient  $Z = -2$  trigger of L3 is able to enhance the  ${}^3\overline{\text{He}}$  signal and thus to provide a high statistics event sample for the offline analysis. At the same time, L3 brings the observation of those exotic clusters with  $Z = -2$  within the reach of the STAR, for which a very large data set is needed, i.e. 10M central events or more. First, the detection of anti-hypertritons  ${}^3_{\Lambda}\overline{\text{H}}$ , decaying partially into  ${}^3\overline{\text{He}} + \pi^-$ , and second, the observation of the anti-alpha  ${}^4\overline{\text{He}}$ . Both would be observed for the first time. The event sample collected so far could be sufficient for a first hint of the  ${}^3_{\Lambda}\overline{\text{H}}$ , whereas for the detection of  ${}^4\overline{\text{He}}$  a factor of 5 or 10 more events need to be scanned. For this large number of events, the L3 trigger becomes essential to reduce the amount of events for storage and the time consuming offline analysis.



# Chapter 5

## The Offline Reconstruction

The offline reconstruction software faces the challenging task of analyzing the raw detector information with a precision, sufficient for the goals of the STAR physics program. This involves not only the reconstruction of up to 1500 charged particle tracks seen in the TPC, but also particle identification and the reconstruction of the primary event vertex. STAR's Global Reconstruction Chain combines the reconstruction of the sub-detector data and can optimize therefore both precision and particle identification capabilities with a maximum use of the available information. In addition, a detailed knowledge about the running conditions is involved in reconstruction to calibrate the detector response and correct for the various distortion effects.

This chapter shall introduce the offline event reconstruction. It will focus on the TPC reconstruction, as relevant part for the data analysis presented in this thesis, and will give a short overview on the global event reconstruction including the primary vertex reconstruction. The event reconstruction was described earlier in [45], whereas the overall design is explained in [46].

### 5.1 Event Reconstruction in the TPC

As described already in Chapter 3.3, which introduced the event reconstruction of the Level-3 system, the reconstruction and analysis of the TPC raw data is a two-step process. First, the ionisation clusters are reconstructed by the cluster finder from the raw ADC values in each pad row. And second, the track finder reconstructs the charged particle tracks by finding the ionisation clusters along the track. Other than in the L3 reconstruction, the detector calibration and distortion corrections can be optimized in an iteration process, therefore maximizing the efficiency and resolution.

### 5.1.1 Cluster Finding

The cluster finder reconstructs the ionisation clusters from the charge distribution, which is measured on the pad plane as a function of drift time. The clusters are found in local coordinates (see Appendix A for the definition of the coordinates in STAR) by comparing sequences of ADC values above threshold with similar time bins in adjacent pads of a given pad row. Before that, the charge and time bin information for each pad is corrected for individual offsets and gain variations. The weighted mean of the cluster charge distribution in pad and time bin direction gives the cluster position.

Each cluster is scanned for local minima in the charge sequences in both pad and time bin direction to recognize overlapping clusters, which originate from more than one track. For single track clusters the total ionisation energy is given by the sum of the measured charge. Multiple track clusters are split and the charge divided. The position resolution with full magnetic field reaches 0.5 mm (2 mm) in pad row direction for small (large) pad row crossing angles and 1 mm (3 mm) in drift direction for small (large) dip angles (for details see [28]).

### 5.1.2 Track Finding

The track finder connects the ionisation clusters to form tracks, where it assumes a helix as track model. The track reconstruction starts at the outside of the TPC using cluster combinations of the outer pad rows as track seeds and employs the follow-your-nose method to reconstruct the full track length, similar to the L3 track finder. However, the full volume of the TPC is tracked at once, so no artificial sector boundaries and additional track splitting is introduced. The reconstructed TPC tracks are not directly used for analysis, but serve as track seeds for the global reconstruction chain, described below.

### 5.1.3 Distortion Corrections

Deviations from ideal conditions in the TPC, for example non-uniformities of magnetic and electric field and global misalignments, cause distortions of the electron drift path and therefore of the cluster position at the read-out plane. The distortions in the transverse plane (perpendicular to the magnetic field axis and the beam line in STAR) influence the transverse momentum measurement. These are typically below 1 mm and have biggest impact on high momentum tracks, which are nearly straight. Table 5.1 summarizes the distortion corrections applied to the data, whereas Figure 5.1, both taken from [28], shows the sum of the distortion corrections as a function of TPC radius and distance to the central membrane. The corrections reduce the relative error between a point and the track-model fit to 50  $\mu\text{m}$ , whereas the absolute error of

the space-point position is approximately  $500 \mu\text{m}$ .

**Table 5.1:** The distortion corrections applied to STAR data; their cause, and the magnitude of their effect on the data [28].

Cause of the Distortion	Magnitude of the Imperfection	Magnitude of the Correction
Non-uniform B field	$\pm 0.0040 \text{ T}$	0.10 cm
Geometrical effect between the inner and outer sub-sectors	Exact calculation based on geometry	0.05 cm (near pad row 13)
Cathode - non-flat shape and tilt	0.1 cm	0.04 cm
The angular offset between E and B field	0.2 mr	0.03 cm
TPC endcaps - non-flat shape and tilt	0.1 cm	0.03 cm
Misalignment between IFC and OFC	0.1 cm	0.03 cm
Space Charge build up in the TPC	$0.001 \text{ C} / \epsilon_0$	0.03 cm

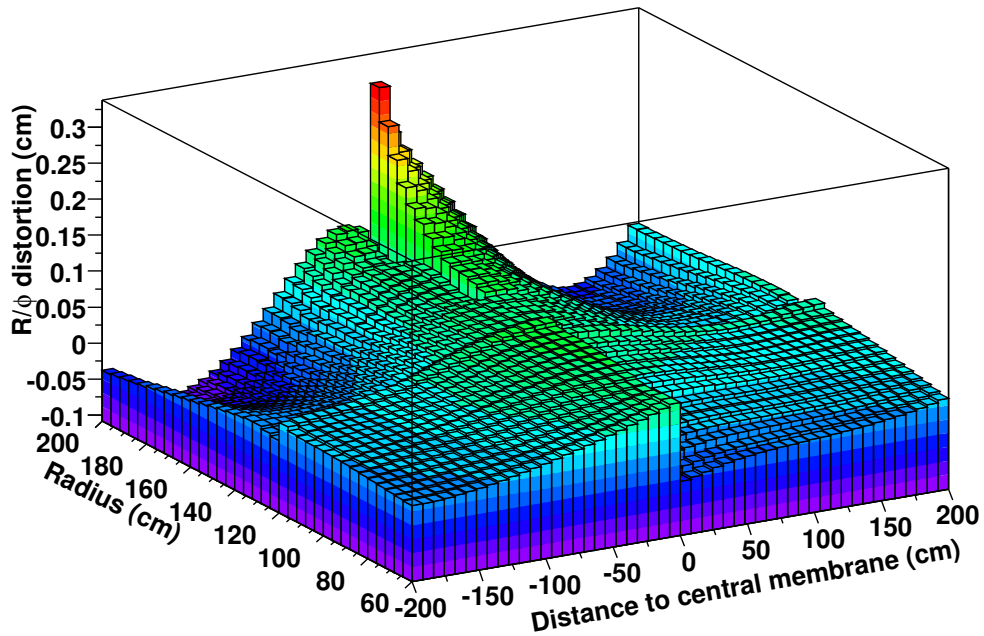


**Figure 5.1:** The sum of all distortion corrections as a function of radius and distance to the central membrane [28].

## 5.2 Global Event Reconstruction

The global reconstruction chain is designed to combine the information of all subsystems and to treat STAR as a single detector. Only this way, the momentum measurement and particle identification capabilities of STAR can be optimized. The reconstructed particle tracks are stored in Data Structure Tables (DSTs), where the information from all subsystems is collected and assigned to the tracks. As some of the subsystems beside the TPC, e.g. the SVT and EMC, were still in the commissioning phase during the 2001 run, the full integration of these detectors into the global reconstruction chain is still in progress. The three steps of the global reconstruction chain, relevant for the analysis presented in this thesis, are the global tracking, the primary vertex reconstruction and the primary track fit and shall be described briefly in this section.

### 5.2.1 Global Tracking

The global tracking algorithm is based on the Kalman Filter [47] approach. This allows a simultaneous track reconstruction and fitting — a technique widely used in High-Energy-Physics experiments. In STAR, the Kalman Filter refits the tracks found by the TPC track finder, taking multiple coulomb scattering and energy loss in the detector material into account (assuming the particle is a pion). Incorrectly assigned hits to the tracks are removed, based on the hit errors provided by the cluster finder. In addition, the Kalman Filter provides a natural way to include the effects of multiple scattering and energy loss in the track extrapolation from one detector to another.

Reconstructed tracks passing the Kalman Filter are called *global tracks*. The momentum resolution for global tracks is shown in Figure 3.3, where those are marked as offline tracks fitted without primary vertex. Figure 3.4 compares the tracking efficiency of the L3 track finder to the offline reconstruction after global tracking (see also [28]). So far, global tracks include only the TPC information.

### 5.2.2 Primary Vertex Reconstruction

Currently, no dedicated primary vertex detector is installed in STAR. The reconstruction chain finds the primary vertex by extrapolating the global tracks back to the origin. The global average is taken as primary vertex position. This algorithm [48] achieves a  $350 \mu\text{m}$  resolution for events with more than 1000 TPC tracks [28]. The vertex finding efficiency is found to be larger than 98% if more than 100 tracks are used. It is expected, that including the SVT information in the algorithm improves the resolution by a factor of ten.

### 5.2.3 Primary Track Fit

Adding the primary vertex to the track fit can significantly improve the momentum resolution, as the primary vertex is known much more precisely than the space-points measured in the TPC. All tracks with a distance of closest approach to the primary vertex of less than 3 cm are considered to be *primary tracks*, i.e. originating from the primary vertex. These tracks are refit with a helix track-model, where the primary vertex is included as an additional point. The transverse momentum resolution can be seen in Figure 3.3, where primary tracks are marked as offline tracks fitted with vertex. The best relative momentum resolution of 2% is reached for pions at a transverse momentum of 400 MeV/c (see also [28]). For the analysis presented in the following chapter only primary tracks were used. Tracks, for which the primary track fit failed, are flagged by the reconstruction software and excluded from the analyzed data sample.

## 5.3 Particle Identification with $dE/dx$

The track reconstruction in the magnetic field yields the charge and momentum  $p$  of the measured particles. However, this is not sufficient to identify the particle species. The measurement of the specific energy loss along the particle trajectory in the TPC gas provides the necessary additional information on the particle velocity  $v$ , and therefore on the particle mass  $m$ , since

$$v = \frac{pc^2}{E} = \frac{pc^2}{\sqrt{p^2c^2 + m^2c^4}}. \quad (5.1)$$

This section shall briefly introduce the underlying Bethe-Bloch equation for the specific energy loss, the measurement and the calibration in the TPC.

### 5.3.1 The Bethe-Bloch Equation

Charged particles lose energy in matter primarily by ionisation. The mean energy loss  $dE$  per unit path length  $dx$  was first calculated by Bethe and Bloch [49] and later modified by Fermi to include polarization effects in the traversed medium [50] for large velocities. The Bethe-Bloch equation is given by

$$\left\langle -\frac{dE}{dx} \right\rangle = K\rho z^2 \frac{Z}{A} \frac{1}{\beta^2} \left( \frac{1}{2} \ln \frac{2m_e c^2 \beta^2 T_{max}}{I(1-\beta^2)} - \beta^2 - \frac{\delta}{2} \right), \quad (5.2)$$

with

$m_e c^2$  : Rest energy of the electron

- $r_e$  : Classical electron radius
- $N_A$  : Avogadro's number
- $ze$  : Charge of incident particle
- $Z$  : Atomic number of the medium traversed
- $A$  : Atomic mass of the medium traversed
- $\rho$  : Density of the medium traversed
- $\beta$  :  $v/c$  of the incident particle
- $K/A$  :  $4\pi N_A r_e^2 m_e c^2 / A$
- $I$  : Mean excitation energy of the medium
- $T_{max}$  : Maximum kinetic energy transfer to a freed electron in a single collision
- $\delta$  : Density effect correction

At low momentum the energy loss is dominated by the overall  $1/\beta^2$  factor and decreases until about  $v = 0.96c$ , where a minimum is reached. Particles with this velocity are therefore called *minimum ionizing*. Beyond this point, the energy loss increases due to the logarithmic factor. Fermi's correction term  $\delta$  compensates this increase in the limit  $\beta \rightarrow 1$  and the Bethe-Bloch equation saturates in the *Fermi plateau*. Ionization of gas atoms with very high energy transfer to the freed electron generate a separate particle track of a so-called  $\delta$ -electron. These tracks cannot contribute to the ionisation energy loss anymore. To reflect this, a "cut-off" energy  $T_{max}$  is introduced [51] and energy transfers larger than  $T_{max}$  are discarded in the calculation.

### 5.3.2 Measurement and Calibration

In general, the amount of ionisation of the gas is measured in the TPC. One assumes, this is proportional to the energy loss and thus treats them as equivalent. The ionisation along the particle track is sampled in each pad row crossed by the track, in total up to 45 times. Due to the possibly large energy transfer in hard collisions between the traversing particle and the electrons of the gas molecules, these samples are not Gaussian distributed around it's most probable value, but follow a Landau distribution [52] with a long tail to high ionisation. The best estimate for the most probable value of the Landau distribution is the *truncated mean*, where the asymmetric tail is truncated and the mean of the remaining, almost Gaussian distribution is taken. In STAR the highest 30% of the ionisation samples are discarded. The truncated mean  $dE/dx$  value as a function of momentum for primary and secondary tracks is shown in Figure 5.2. The expected ionisation energy loss based on the Bethe-Bloch equation is included as well.



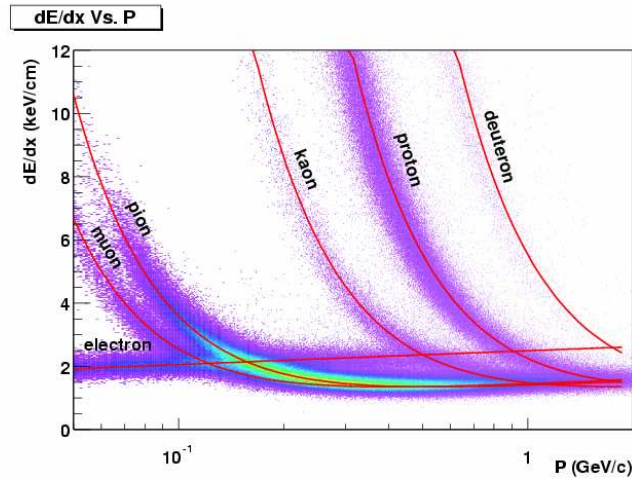


**Figure 5.2:** Particle identification via  $dE/dx$ : Truncated mean  $dE/dx$  as a function of momentum for primary and secondary particle tracks. Included are Bethe-Bloch expectations for the observed particle species.

Crucial for an effective particle separation is a high resolution of the  $dE/dx$  measurement in the TPC. This needs a careful calibration, which corrects for hardware effects and variations of the detector response as a function of time. The calibration [53] involves four steps and is based on both pulser data and comparisons with the expected Bethe-Bloch values.

The first step, gain correction on the pad level, is applied already at the cluster finder stage. This corrects for gain variations caused by the electronics and marks dead or noisy pads as unusable. The correction table was obtained from pulser data, where each channel of the read-out electronics was pulsed with an identical test signal.

The next steps are obtained from comparisons of the measured ionisation with the expected Bethe-Bloch value for pions. All global tracks with at least 30 fit points and a minimum track length of 40 cm in the TPC were included. These steps account for

- gain variations versus sector and row, which have not been accounted for by the pad-level correction,
- the time dependence of the gain correction, mainly due to pressure and gas mixture variations, and
- the drift distance correction, caused by absorption of drifting electrons in the gas.

The best achievable  $dE/dx$  resolution for the data set used in this analysis was found to be 7.6% for tracks with 31 ionisation samples after truncation (corresponding to 45 fit points and without any merged clusters in the sample). Figure 5.3 shows the resolution versus the number of ionisation samples ( $dE/dx$  points).

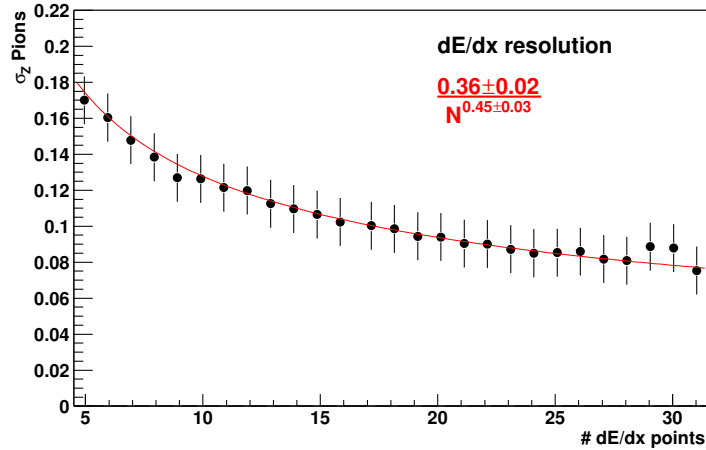


**Figure 5.3:**  $dE/dx$  resolution versus number of ionisation samples ( $dE/dx$  points).

## 5.4 Simulation

The estimates of momentum resolution and efficiency of the track reconstruction as well as estimates of efficiencies for the data analysis rely on a detailed simulation of the STAR detector. The common procedure uses GEANT [54] to simulate the detector signal for a given Monte Carlo input. Detector response simulators (for the TPC Response Simulator see [55]) generate raw data for this in the same form as the detector would produce under real conditions. This data can be then processed by the reconstruction chain in the same way as real data.

To estimate the resolution and reconstruction efficiencies under realistic conditions, the common *Embedding* technique is used. Here, a small number of simulated tracks is embedded into real events at the raw data level without significantly disturbing the event conditions and then pass the full reconstruction chain. Reconstructed and Monte-Carlo tracks are matched based on a geometrical comparison of the space-points of the tracks. The efficiencies are calculated from the ratio of the number simulated tracks in the reconstructed data to the number of tracks in the GEANT input.

# Chapter 6

## The Analysis of Antinuclei Spectra

The interpretation of nuclei and antinuclei spectra provides insight into the dynamics and size of the heavy-ion collisions at the late stage. This chapter shall describe, how the antideuteron and antihelium cross sections are extracted from the STAR data.

This thesis is based on the analysis of the reconstructed TPC data from the Au-Au run at  $\sqrt{s_{NN}} = 200$  GeV of year 2001. First, the identification of light clusters and the clean-up cuts applied to data will be introduced. Deuterons, tritons and helium-3 as well as their anti-particles can be identified clearly. However, positively charged clusters — unlike the corresponding antinuclei — suffer from a large, unknown contribution of clusters, which originate from hadronic interactions in the detector material instead of the fireball. A detailed analysis of the nuclei spectra is therefore out of the scope of this thesis.

The correction of the spectra includes background subtraction, energy loss, absorption, detector acceptance and efficiency. The uncertainties due to systematic effects are estimated by varying the cuts applied to the data and the parameters of the corrections. A description of the common choice of variables in heavy-ion physics will be given in Appendix A.

### 6.1 Data Set

This analysis is based on the STAR data recorded during the AuAu run of the year 2001 at RHIC's top energy of  $\sqrt{s_{NN}} = 200$  GeV. The data set consists of hadronic central triggered events (run types *productionCentral*, *productionCentral600* and *productionCentral1200*), which are unbiased by Level-3. The centrality selection of this trigger setting corresponds to the top 10% of the total hadronic cross section, measured via the multiplicity distribution observed in the TPC.

The total number of events in the data set is 3.3M, almost equally divided into both magnetic field polarities at 0.5 T (full field). The symmetry of the STAR

detector allows to treat the data of both field polarities as equivalent. The Level-0 trigger constrained the primary vertex position along the beam line to  $|z_{vertex}| < 35$  cm, based on the ZDC timing information. The resulting vertex distribution for this data set is shown in Figure 6.1.

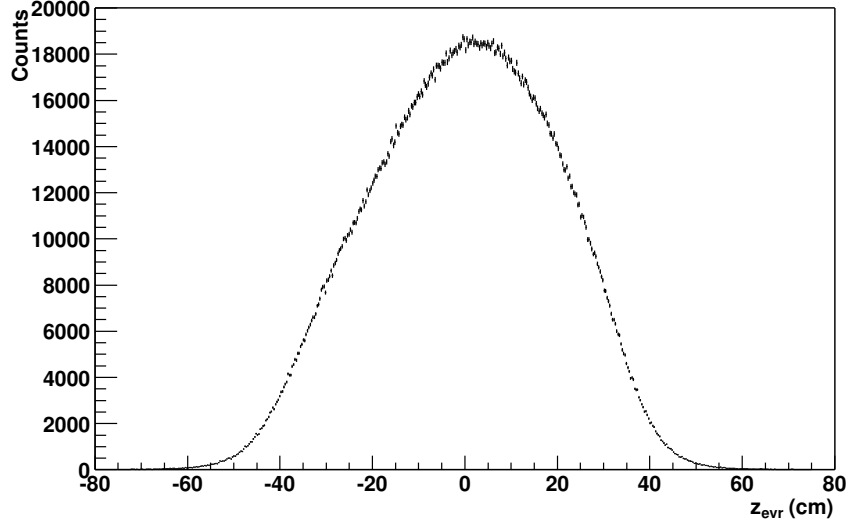
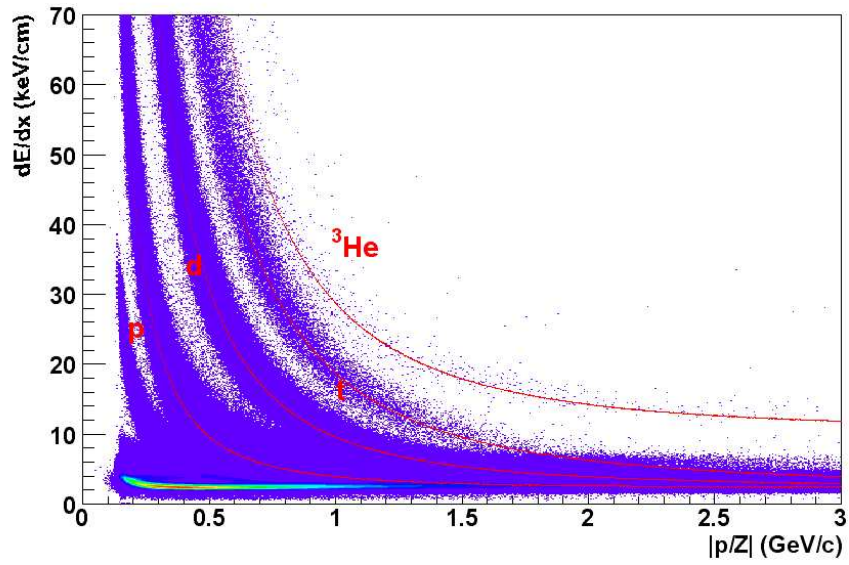


**Figure 6.1:** Primary vertex position in beam direction for the hadronic central Au-Au events included in the analysis.

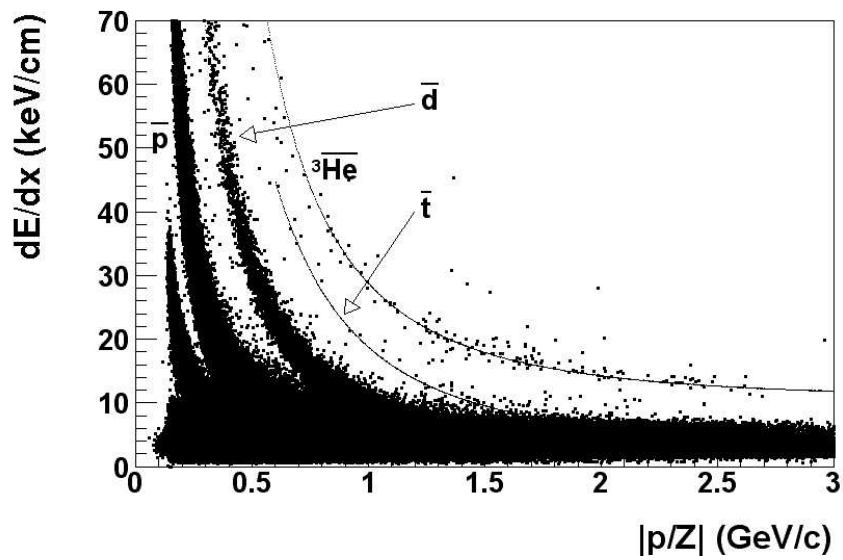
## 6.2 Antinuclei Identification

The identification of nuclei and antinuclei is possible with the ionisation energy loss measurement in the TPC. Figure 6.2 shows the  $dE/dx$  distributions for both positive and negative particle tracks, which pass the track quality cuts described below. Bands of  $d$ ,  $t$  and  ${}^3\text{He}$  as well as of their anti-particles can be recognized. Please note, that the rigidity  $|p/Z|$  is plotted and the momentum of helium-3 is twice as large. No clear antitriton band is observed. However, these are expected to have a similar momentum distribution as  ${}^3\overline{\text{He}}$  and thus reside mainly in a region where the separation power of  $dE/dx$  is not sufficient.

Unlike  $d$  and  $\bar{d}$ , whose identification is limited to the momentum range below 1 GeV/c (1.5 GeV/c for  $t$ ,  $\bar{t}$ ),  ${}^3\text{He}$  and  ${}^3\overline{\text{He}}$  candidates can be identified over almost the full momentum range, limited only by the detector acceptance and saturation effects in the TPC electronics for low momentum tracks.



(a)



(b)

**Figure 6.2:** (Anti)nuclei identification with  $dE/dx$ . Shown is the  $dE/dx$  distribution for positive (a) and negative (b) charged particle tracks, which pass the clean-up cuts (see text). Solid lines show the Bethe-Bloch expectations.

### 6.2.1 Cuts

Before the actual particle identification is performed, several cuts are applied to the data. These either restrict the momentum-rapidity range for the identification to a range of sufficient efficiency and particle identification, or require a minimum track quality, i.e. track length and reliable  $dE/dx$  calculation.

The antideuteron identification via  $dE/dx$  is limited to the momentum range below 1 GeV/c and middle rapidity  $|y| < 0.3$ . In addition, only events with a primary vertex in the region  $\pm 25$  cm along the beam line are included in the antideuteron analysis, as the centrality selection by the Level-0 trigger is less reliable outside of the ZDC triggered vertex range.

To make use of the full available event sample for the very small  ${}^3\overline{\text{He}}$  signal, the phase-space and primary vertex is not restricted for this analysis. In both the  $\overline{d}$  and the  ${}^3\overline{\text{He}}$  analysis only primary tracks were used, therefore including a cut on the distance of closest approach (dca) of the corresponding global track fit of less than 3 cm. Table 6.1 summarizes the cuts for the  $\overline{d}$  and  ${}^3\overline{\text{He}}$  analysis. The track quality cuts will be explained in the following paragraphs, illustrated by the Figures of the  ${}^3\overline{\text{He}}$  analysis.

**Table 6.1:** Summary of the cuts applied in the  $\overline{d}$  and  ${}^3\overline{\text{He}}$  analysis.

Cut	$\overline{d}$	${}^3\overline{\text{He}}$
$\# \text{ Fit points}$	$\geq 29$	$\geq 30$
$\frac{\# dE/dx \text{ points}}{\# \text{ Fit points}}$	$> 0.3$	$> 0.3$
$dca$	$dca_{global} < 3.0 \text{ cm}$	$dca_{global} < 3.0 \text{ cm}$
$p_t$	$0.4 < p_t < 1.0 \text{ GeV/c}$	—
$y$	$ y  < 0.3$	—
$z_{vertex}$	$ z_{vertex}  < 25 \text{ cm}$	—

#### nFitPoints Cut

The first track quality requirement is the number of ionisation clusters (space-points) used for the track fit. Here, a tight cut of at least 29 (30) out of 45 possible fit points is used for the  $\overline{d}$  ( ${}^3\overline{\text{He}}$ ) analysis. This cut assures, that a minimum track length was observed in the TPC, and therefore a reasonable momentum reconstruction. Figure 6.3 shows the number of fit points for the  ${}^3\overline{\text{He}}$  candidate tracks with a ratio of number of  $dE/dx$  points to fit points larger than 0.3 (see next paragraph). The cut is placed between the short — and possibly background — tracks and the long tracks with a reliable track model fit.

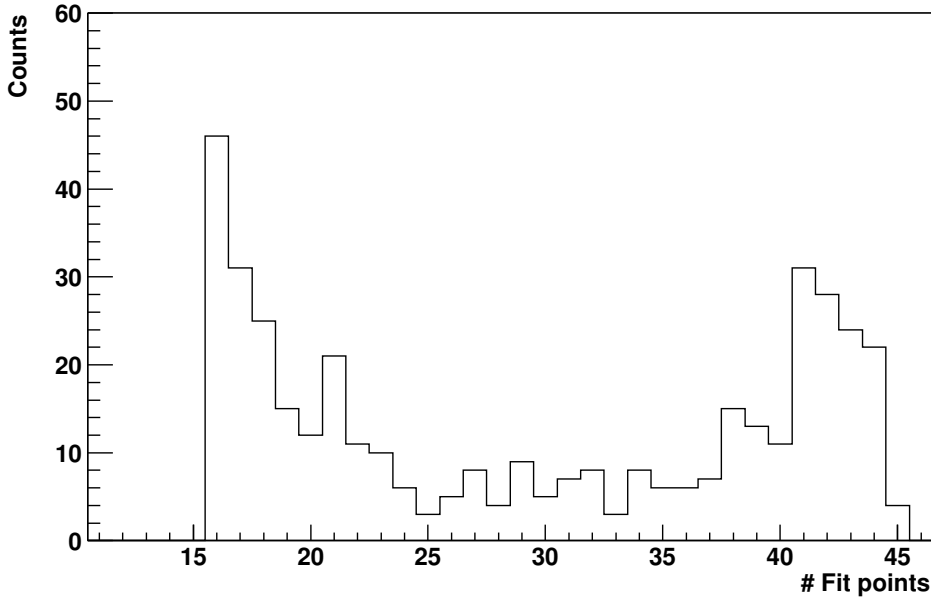


**Figure 6.3:** Number of fit points for the  ${}^3\overline{\text{He}}$  candidate tracks with a ratio of number of  $dE/dx$  to fit points larger than 0.3. The analysis cut requires at least 30 fit points.

#### **ndE/dxPoints/nFitPoints Cut**

The second track quality cut is intended to remove tracks from the candidate sample with an improper  $dE/dx$  calculation. Potentially merged ionisation clusters originating from more than one track are marked by the cluster finder. These are discarded in  $dE/dx$  calculation and only used for the track fit. Tracks with more than 30% potentially merged clusters in the  $dE/dx$  point sample after truncation are excluded from the analysis. The ratio of the number of  $dE/dx$  points to the number of fit points is shown in Figure 6.4 for all  ${}^3\overline{\text{He}}$  candidate tracks with at least 30 fit points. Please note, that a logarithmic ordinate is used. Tracks with an improper  $dE/dx$  and a very small number of relevant  $dE/dx$  points are removed by the cut at 0.3.

### **6.3 Antinuclei Yield and Corrections**

To extract the actual particle yield from the measured  $dE/dx$  distribution, the  $Z$  quantity is used, which is defined as

$$Z(i, \vec{p}) = \ln \left( \frac{dE/dx}{I_{BB}(i, \vec{p})} \right). \quad (6.1)$$

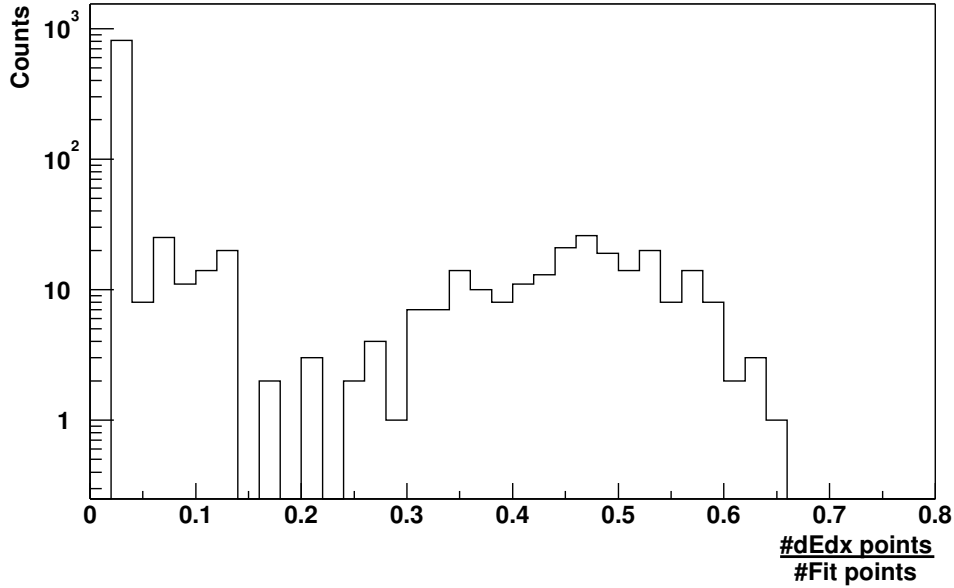


**Figure 6.4:** Ratio of number of  $dE/dx$  points to number of fit points for the  ${}^3\overline{\text{He}}$  candidate tracks with at least 30 fit points. A ratio larger than 0.3 is required by the analysis.

Here,  $I_{BB}(i, \vec{p})$  is the expected ionisation from the Bethe-Bloch Equation for the observed particle species  $i$  at the momentum  $\vec{p}$ . This quantity shows roughly a Gaussian distribution, which is centered at zero for the particle species in question, and therefore allows to separate signal and background contributions in a simple way.

The invariant cross section calculation for  $\overline{d}$  and  ${}^3\overline{\text{He}}$  includes several corrections of the measured particle yield. As GEANT does not contain a model for either  $\overline{d}$  or  ${}^3\overline{\text{He}}$  interactions in matter,  $d$  and  ${}^3\text{He}$  Embedding simulations are evaluated to understand the reconstruction efficiency, acceptance and energy loss. A correction for annihilation in the detector is added afterwards.

### 6.3.1 Energy Loss

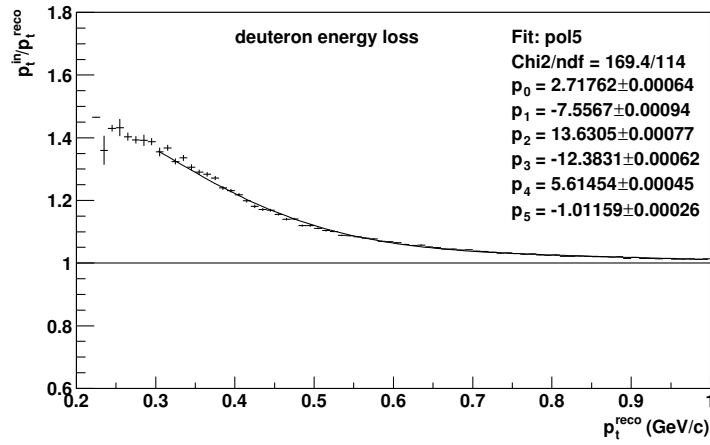
Before the particle yield can be extracted, the transverse momentum  $p_t$  measured in the TPC is corrected for energy loss. Each particle loses energy, due to multiple scattering in the detector material, before the TPC is reached. Figure 6.5 shows the energy loss as a function of reconstructed transverse momentum from the Embedding simulations for deuterons and helium-3.

The energy loss of deuterons reaches from 30% at 0.3 GeV/c to 3% at 0.7

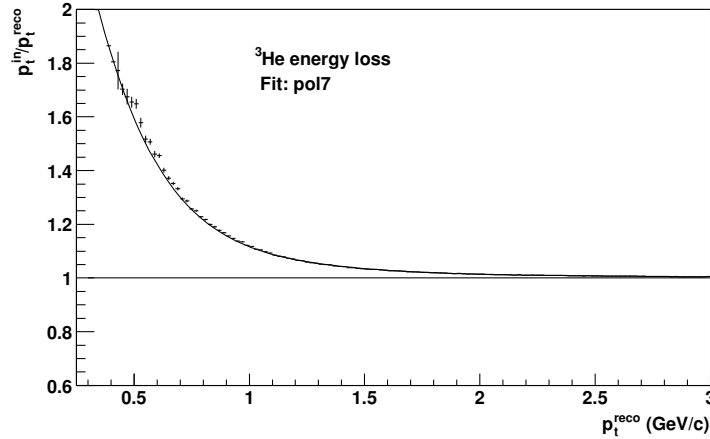


GeV/c. The polynomial parametrization included in Figure 6.5 is used to correct the measured transverse momentum. The rapidity dependence of this correction is weak (less than 10%) in the region investigated and can be therefore neglected.

Even so the energy loss for  ${}^3\text{He}$  is large at low momenta — approximately 50% at 0.5 GeV/c — the correction is less than 10% in the momentum and rapidity range relevant for the final analysis. For the large transverse momentum bins used in the analysis ( $p_t$  bin width 1 GeV/c), the effect of this correction is rather small and neglected in the analysis.



(a)



(b)

**Figure 6.5:** Energy loss correction: Ratio of input to reconstructed transverse momentum  $p_t^{in}/p_t^{rec}$  as a function of  $p_t^{rec}$  for  $d$  (a) and  ${}^3\text{He}$  (b).

### 6.3.2 Background Subtraction

#### Antideuteron Yield

The antideuteron yield is extracted in six  $p_t$  bins in the interval  $0.4 < p_t < 1.0$  GeV/c at mid-rapidity,  $|y| < 0.3$ . This is the region of high reconstruction efficiency (see next section) and sufficient particle identification. Figure 6.6 shows the  $Z$  distribution for each bin in  $p_t$ . It can be seen, that the background contribution from other particles ( $\bar{p}$  and  $\pi^-$ ) increases with increasing momentum. Extracting the yield beyond  $p_t = 0.9$  GeV/c becomes rather difficult.

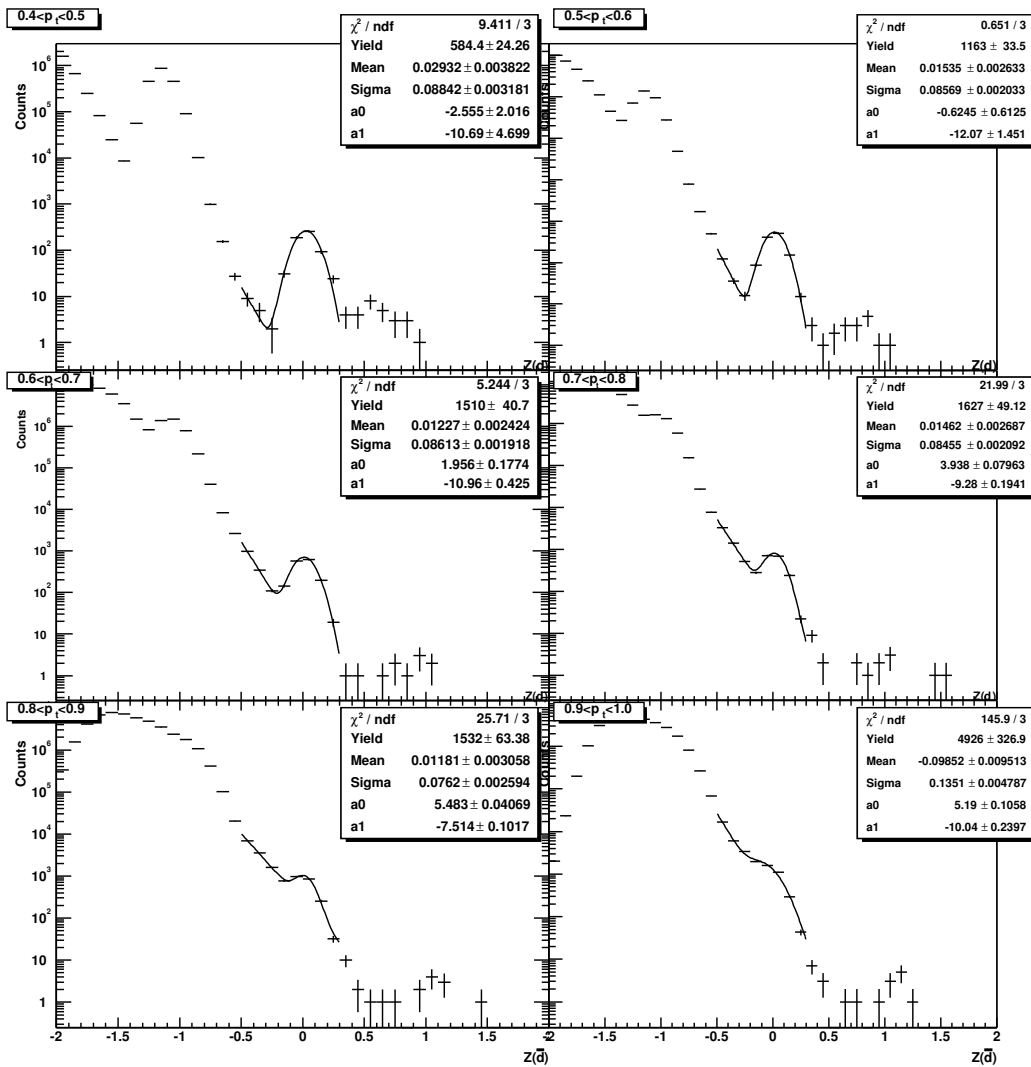


**Figure 6.6:**  $Z$  distribution for  $\bar{d}$  in the transverse momentum  $p_t$  bins between  $0.4 < p_t < 1.0$  GeV/c at mid-rapidity,  $|y| < 0.3$ . Also shown are the combined Gaussian+exponential fits, which model signal and background.

The  $Z$  distributions are fitted with a combined Gaussian signal and exponential background function,

$$f(x) = \frac{Yield}{\sqrt{2\pi}\sigma} \exp\left(-\frac{(x - Mean)^2}{2\sigma^2}\right) + \exp(a_0 + a_1x), \quad (6.2)$$

in the range  $-0.5 < Z < 0.3$ . These fits and the parameters are included in Figure 6.6. The  $\bar{d}$  yield, shown in Figure 6.7 is then extracted by integrating the Gaussian parametrization of the signal distribution. The integral of the exponential background function — in the region  $-0.3 < Z < 0.3$  of the observed signal — allows to estimate the signal-to-background ratio, see Figure 6.8.

The statistical uncertainty of the extracted yield is taken from the uncertainty, which is given by the  $\chi^2$ -fit of the parametrization (Equation 6.2). This includes therefore the contribution of the statistical uncertainty of the background estimate in the correct way. The assumption of the background shape in the  $Z$  distribution and the dependence of the background estimate on the fit range contribute to the systematic uncertainties. These will be discussed in the following section, where the effects of a variation of cuts and correction parameters on the extracted yield will be explored.

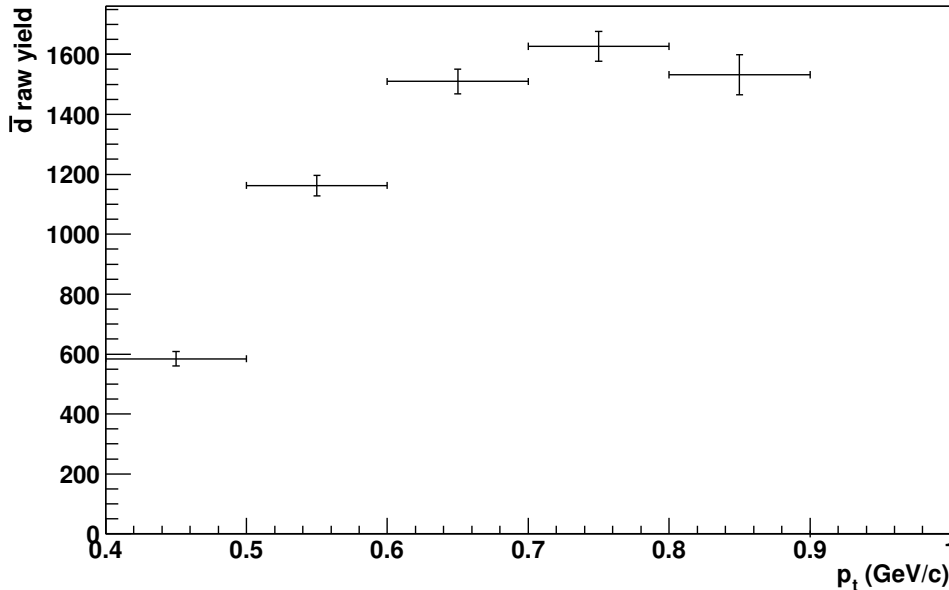
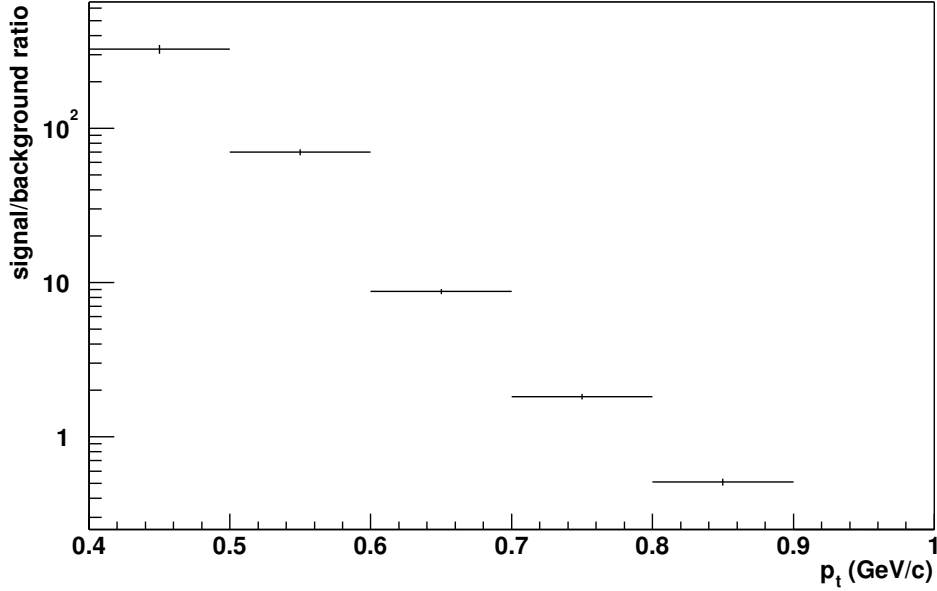


Figure 6.7:  $\bar{d}$  raw yield as a function of transverse momentum.



**Figure 6.8:**  $\bar{d}$  signal-to-background ratio as a function of transverse momentum.

### Antihelium-3 Yield

The statistics of the event sample is not sufficient to perform a similar analysis for the  ${}^3\bar{\text{He}}$  signal and to split the  $Z$  distribution into several  $p_t$  bins. However, the  $Z$  distribution for the whole momentum range, shown in Figure 6.9, can still be used to estimate the overall background contribution to the signal. Due to a minor miscalibration of the Bethe-Bloch parametrization, the  ${}^3\bar{\text{He}}$  signal is not exactly centered at zero.

One can see an almost clean separation of the  ${}^3\bar{\text{He}}$  signal and the background distribution. A small  $\bar{t}$  signal can be recognized as well. The distribution can be described by a combination of two Gaussians for the  ${}^3\bar{\text{He}}$  and  $\bar{t}$  signal plus exponential background. Figure 6.9 illustrates the good agreement of the fit with the data. Evaluating this parametrization yields a background and  $\bar{t}$  contribution to the  ${}^3\bar{\text{He}}$  signal of less than 10%.

The  ${}^3\bar{\text{He}}$  signal is therefore extracted within three sigma of the  $Z$  distribution (corresponding to a cut of  $0.88 \leq [dE/dx]/I_{BB} \leq 1.28$  in  $dE/dx$ ), whereas any background contribution is neglected. A total number of 193 candidates is observed, centered at zero rapidity with a mean transverse momentum of  $\langle p_t \rangle \approx 2.5$  GeV/c, as shown in Figure 6.10. This provides an order of magnitude more statistics than previous measurements by STAR at  $\sqrt{s_{nn}} = 130$  GeV [44] or at SPS [56].

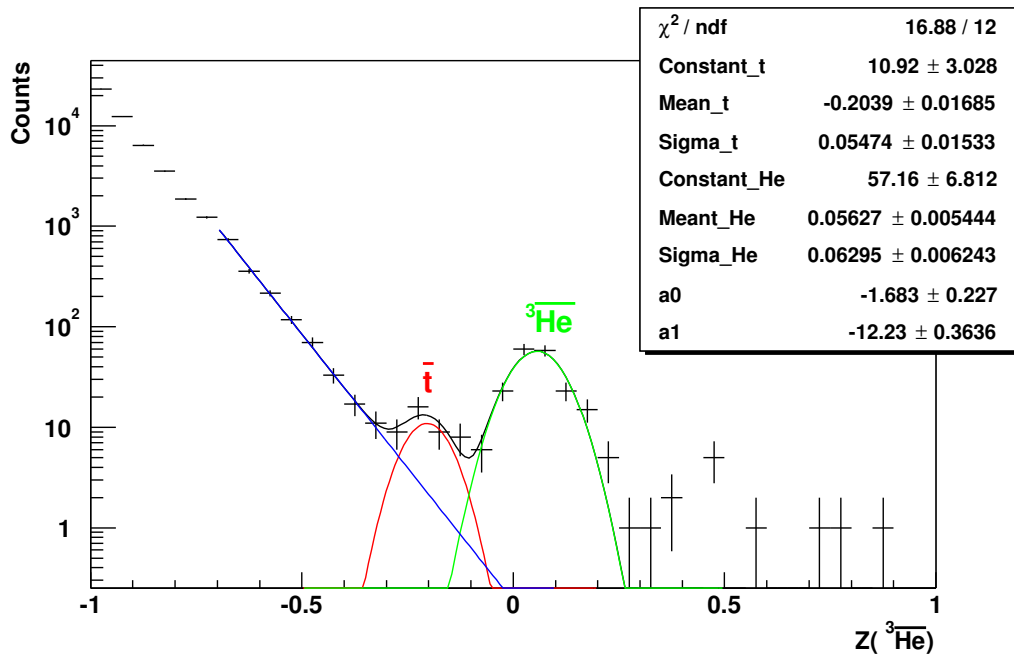


**Figure 6.9:**  $Z$  distribution of the  ${}^3\overline{\text{He}}$  signal. The distribution is fitted with a combination (black line) of two Gaussians for the  ${}^3\overline{\text{He}}$  (green) and  $\bar{t}$  (red) signal and an exponential background (blue).

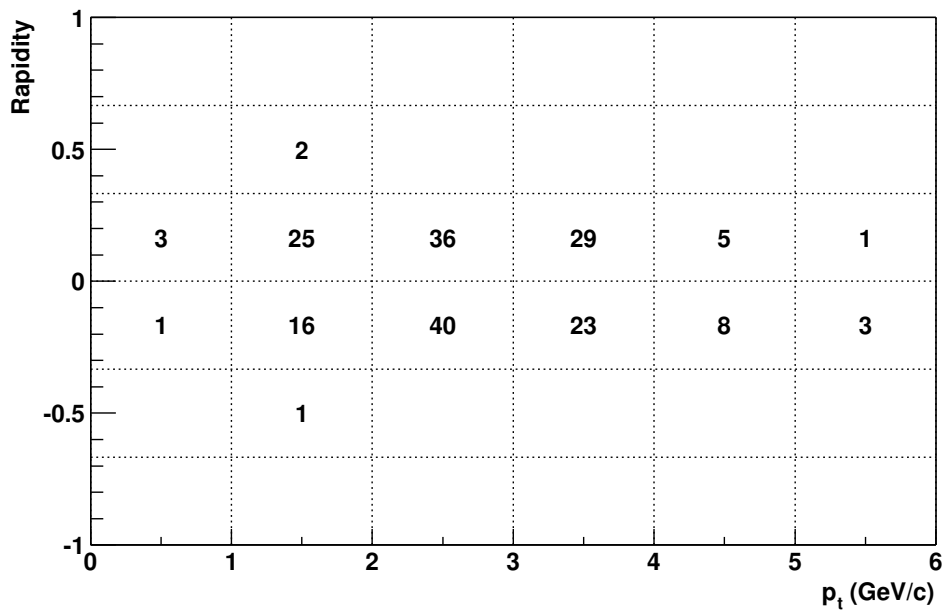


**Figure 6.10:**  ${}^3\overline{\text{He}}$  raw yield as a function of transverse momentum and rapidity.

### Deuteron and Triton Yield

The same analysis as for the  $\bar{d}$  can be used to investigate the observed  $d$  and  $t$  bands in the  $dE/dx$  spectra (see Figure 6.2). The  $Z(d)$  distribution in the same transverse momentum and rapidity region is shown in Figure 6.11. However, a large number of clusters originating from hadronic interactions in the detector material, e.g. the beam pipe and the SVT support structure, contribute to both the  $d$  and  $t$  signal of the fireball. These different contributions cannot be separated by the  $dE/dx$  (or  $Z$ ) measurement and additional cuts are needed, for example on the distance of closest approach to the vertex. Only the  ${}^3\text{He}$  signal at higher transverse momenta  $p_t > 2.5$  GeV/c might show a similar signal-to-background ratio as  ${}^3\bar{\text{He}}$ . The detailed study of the nuclei yield is out of the scope of this thesis and will be discussed elsewhere.

### 6.3.3 Acceptance and Efficiency

Both the geometrical acceptance and the reconstruction efficiency were evaluated with Embedding simulations of  $d$  and  ${}^3\text{He}$ . To assure similar event characteristics for the simulation, i.e. multiplicity and primary vertex distribution, a fraction of the analyzed data set was used. The input particle distributions, flat in rapidity and transverse momentum, undergo full offline reconstruction together with the real data. Matching input and reconstructed tracks are then required to have at least ten TPC points in common. In addition, each reconstructed track matched to the Monte-Carlo input is checked, whether it satisfies the track quality cuts (and the  $dE/dx$  cut for  ${}^3\text{He}$ ).

The efficiency is calculated as a function of transverse momentum and rapidity, retaining the same bin sizes as used for the extraction of the particle yields. It is defined as ratio of number of reconstructed tracks  $\#Reco$  to number of input tracks  $\#MCin$ ,

$$eff(p_t, y) = \frac{\#Reco(p_t^{in}, y^{in})}{\#MCin(p_t^{in}, y^{in})}, \quad (6.3)$$

where the input momentum is used in the numerator for the reconstructed tracks. This way, no requirement on the reconstructed momentum is made and difficulties due to energy loss avoided. By taking the input tracks without checking the minimum number of generated TPC hits, the geometrical acceptance is included in this definition. The efficiencies for  $d$  and  ${}^3\text{He}$  reconstruction are shown in Figures 6.12 and 6.13.

### 6.3.4 Absorption

Another important consideration is the absorption of emitted antinuclei, before they reach the TPC. This correction is based on the annihilation correction

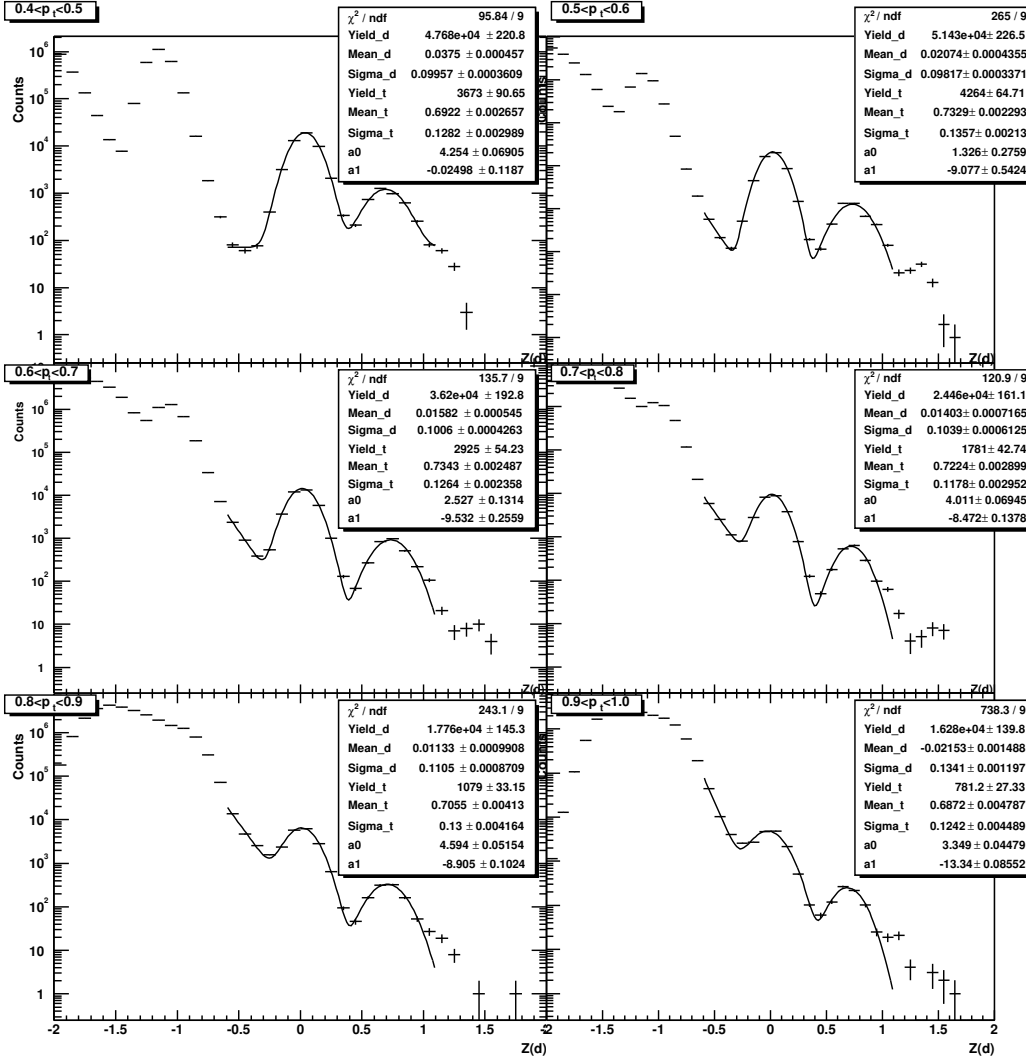


**Figure 6.11:**  $Z$  distribution for  $d$  in the transverse momentum  $p_t$  bins between  $0.4 < p_t < 1.0$  GeV/c at mid-rapidity,  $|y| < 0.3$ . The distributions are fitted with by two Gaussians for the  $d$  and  $t$  signals combined with an exponential background function.

used in STAR's antiproton analysis [57], where the absorption was studied with Monte Carlo simulations. This is not possible for  $\bar{d}$  and  ${}^3\bar{\text{He}}$ , as GEANT does not contain a model for antinuclei interactions in matter. Therefore, the correction relies on the assumption, how the antiproton/proton annihilation cross section  $\sigma_{\text{anni}}(\bar{p}p)$  scales with the nucleon number.

The absorption loss, considered in the antiproton analysis, is parameterized as a function of momentum,

$$\text{abs}(p) = 1 - e^{-\sigma_{\text{anni}}\rho_t p/p_t}, \quad (6.4)$$

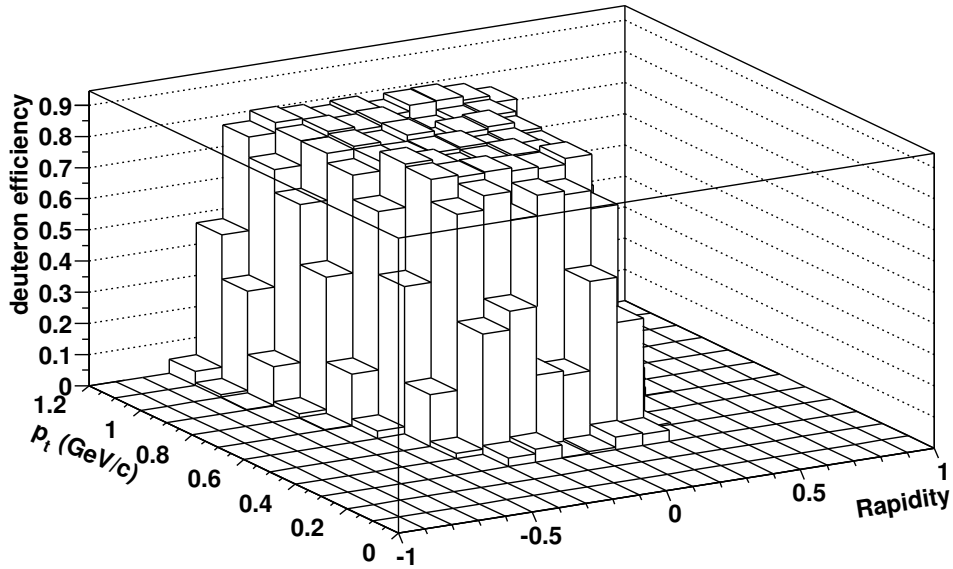


**Figure 6.12:** Deuteron reconstruction efficiency as a function of transverse momentum and rapidity.

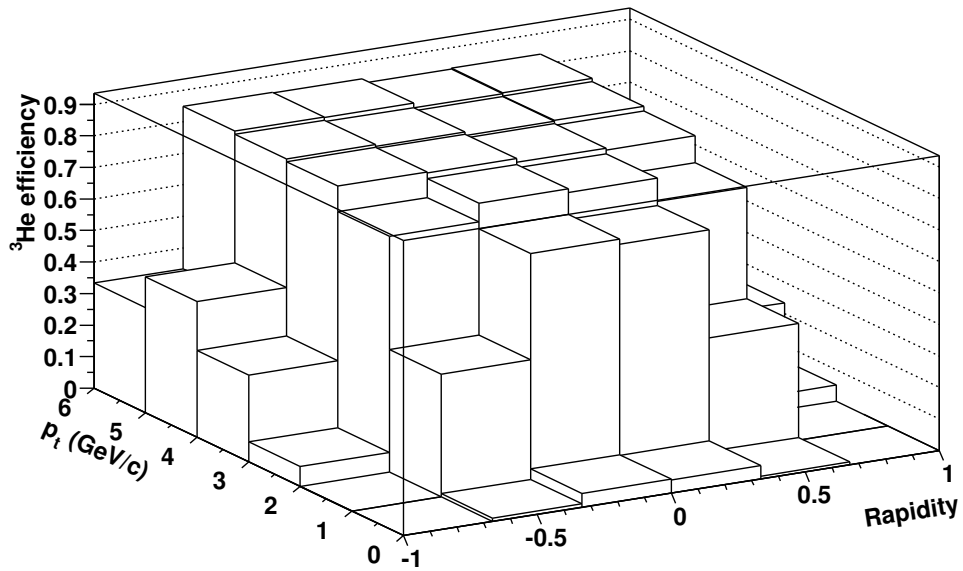


**Figure 6.13:**  $^3\text{He}$  reconstruction efficiency as a function of transverse momentum and rapidity.



where  $\rho_t$  is the density of nucleons in the detector material perpendicular to the beam pipe. Furthermore, a simple parametrization of the annihilation cross section is used, similar to the parametrization in UrQMD [58], which relates the annihilation cross section to the well known total cross section,

$$\sigma_{anni}(\bar{p}p) = 1.2 \sigma_{total}(\bar{p}p) / \sqrt{s}. \quad (6.5)$$

Here,  $s$  is the center-of-mass energy given in  $\text{GeV}^2$ . Figure 6.14, taken from [58], illustrates the antiproton/proton total, elastic and annihilation cross sections as well as the parametrizations used in UrQMD (for the total cross section see also [59]). In the relevant momentum region, the total cross section can be described as a function of the antiproton laboratory momentum  $p$  by

$$\sigma_{total}(\bar{p}p) = 120 p^{-0.65} \text{mb}. \quad (6.6)$$

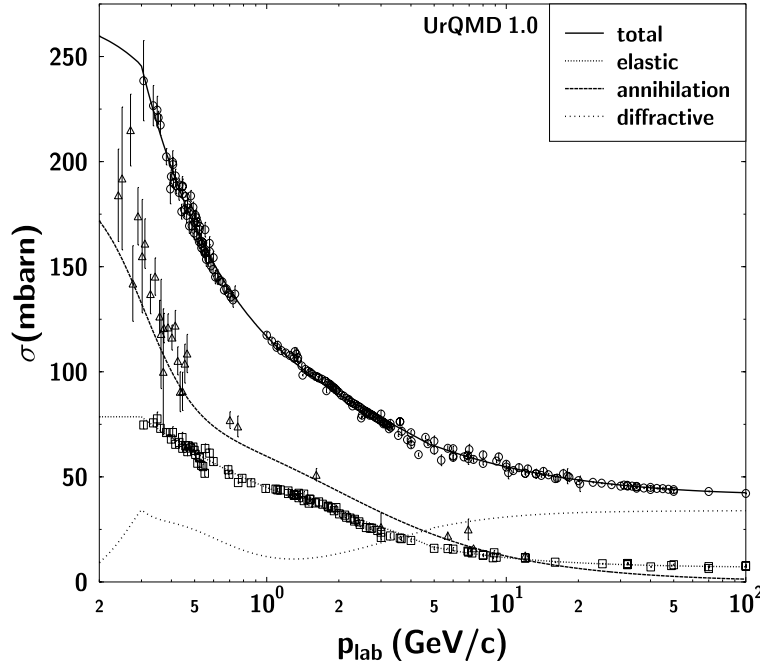


**Figure 6.14:** Antiproton/proton total, elastic and annihilation cross section. Lines show the parametrizations used in UrQMD [58].

The transverse nucleon density  $\rho_t$  is extracted from a fit to the simulation. From this, the antiproton absorption loss correction for the year 2001 data was calculated,

$$abs_{corr}^{\bar{p}}(p) = \exp\left(\frac{0.089}{\sqrt{1+\gamma}} p^{-0.65} \frac{p}{p_t}\right). \quad (6.7)$$

For the  $\bar{d}$  and  ${}^3\bar{\text{He}}$  absorption correction only the annihilation cross section itself is in question, as the amount of detector material faced is the same. Here, a parametrization from reaction data [60] is used, which predicts a scaling of the inelastic cross sections from  $pA$  to  $AA$  collisions as

$$\sigma_{inel}(d, {}^3\text{He}) \approx (\sqrt{2}, 2)\sigma_{inel}(p). \quad (6.8)$$

Assuming that the same relation holds for  $\bar{d}$  as well as  ${}^3\bar{\text{He}}$ , the exponential factor in Equation 6.7 is multiplied by a factor  $\sqrt{2}$  (2) to define the  $\bar{d}$  ( ${}^3\bar{\text{He}}$ ) absorption loss correction. At the same time, the momentum is divided by the nucleon number, to perform the calculation at the same velocity. Figure 6.15 shows the absorption correction functions function of transverse momentum at mid-rapidity for  $\bar{p}$ ,  $\bar{d}$  and  ${}^3\bar{\text{He}}$ , respectively. As the energy loss correction, the absorption correction varies by less than 10% in the transverse momentum and rapidity range relevant for the analysis. Accordingly, the rapidity dependence of the correction function is neglected for both  $\bar{d}$  and  ${}^3\bar{\text{He}}$ .

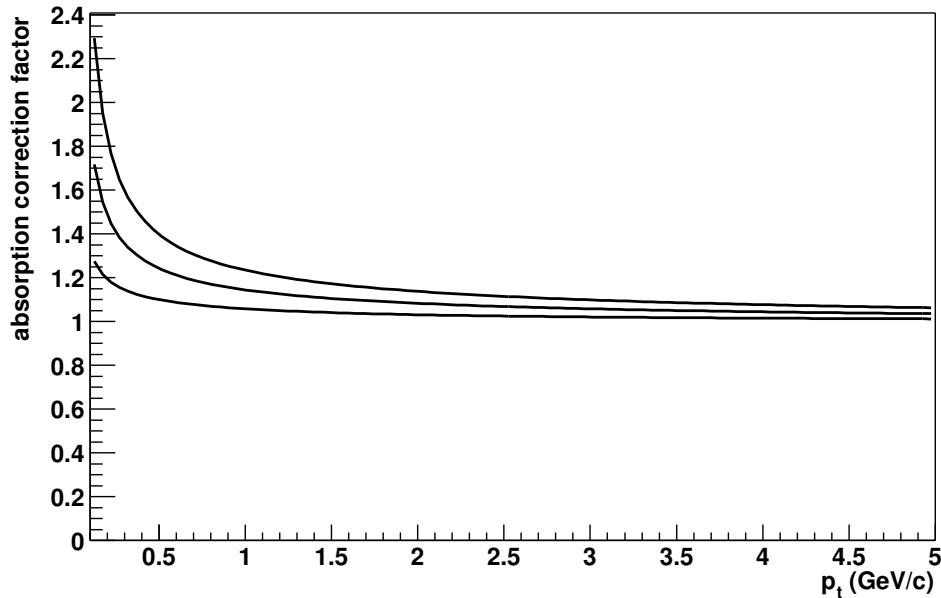


**Figure 6.15:** Absorption correction factor at mid-rapidity as a function of transverse momentum for  $\bar{p}$  (lower curve),  $\bar{d}$  (middle curve) and  ${}^3\bar{\text{He}}$  (upper curve).

## 6.4 Systematic Uncertainties

Before this chapter concludes with the resulting corrected  $\bar{d}$  and  ${}^3\overline{\text{He}}$  spectra, the uncertainties due to systematic effects need to be addressed. These are estimated by varying the parameters of cuts and corrections applied in the analysis of the  $\bar{d}$  and  ${}^3\overline{\text{He}}$  yields.

### 6.4.1 Antideuteron Analysis

Essential for the  $\bar{d}$  analysis is the extraction of the particle yield from the  $Z$  distribution. Several different functions were tested to fit the data, e.g. two Gaussians to fit both the antiproton and the  $\bar{d}$  signal at the same time. However, these fail to describe the data around the  $\bar{d}$  signal. To estimate the uncertainty of the background subtraction, the fit regions are varied. Table 6.2 shows the extracted  $\bar{d}$  yield for different fit ranges in  $Z$ , including the  $\chi^2$  value of the fit. One finds, that the yields are basically non-sensitive to the upper bound of the fit. Changing the lower bound changes the yield significantly only for the two highest transverse momentum bins. However, as the  $\chi^2$  value indicates, these fits are invalid.

**Table 6.2:** Uncorrected antideuteron yield for different fit ranges in  $Z$ .

$p_t$ (GeV/c)	$-0.5 < Z < 0.3$		$-0.5 < Z < 0.5$		$-0.6 < Z < 0.5$		$-0.7 < Z < 0.5$	
	yield	$\chi^2/ndf$	yield	$\chi^2/ndf$	yield	$\chi^2/ndf$	yield	$\chi^2/ndf$
0.45	584	9.4/3	565	14.0/5	585	16.7/6	586	19.5/7
0.55	1163	0.7/3	1163	4.1/5	1165	4.9/6	1162	6.01/7
0.65	1510	5.2/3	1509	6.4/5	1500	8.45/6	1512	16.3/7
0.75	1627	22.0/3	1621	27.7/5	1584	33.1/6	1787	389/7
0.85	1532	25.7/3	1611	43.8/5	0	1583/6	1.3e6	850/7

The uncertainty of the efficiency correction is estimated by changing the track quality cuts. Table 6.3 gives the corrected invariant yield (see next section) and the relative changes for a reduced  $n\text{FitPoints}$  and  $n\text{dEdxPoints}/n\text{FitPoints}$  cut. At the same time, the corresponding track cuts for the Embedding data were left constant. The invariant yield increases by less than 10% compared to the cuts used for the analysis.

As mentioned before, the  $n\text{dEdxPoints}/n\text{FitPoints}$  cut is used to remove tracks with a small number of clean ionisation clusters — possibly caused by two merged tracks reconstructed as a single track — from the data sample. This can be seen in the data, as the signal-to-background ratio decreases by a factor of two over the full momentum range, if this cut is reduced to 0.1

**Table 6.3:** Antideuteron invariant yield for different track quality cuts and constant cuts in Embedding (see text).

$p_t$ (GeV/c)	inv. yield $\times 10^3$	$nFitPoints$ $\geq 25$	$\frac{\# dE/dx \text{ points}}{\# Fit \text{ points}}$ $> 0.1$
0.45	4.18	+7.9%	+9.7%
0.55	3.25	+6.6%	+7.1%
0.65	3.19	+5.0%	+9.4%
0.75	2.97	+3.0%	+5.7%
0.85	2.46	-4.9%	<1%

**Table 6.4:** Antideuteron invariant yield for different correction parameters.

$p_t$ (GeV/c)	inv. yield $\times 10^3$	no energy loss	anni. scale factor	
			1.2	1.6
0.45	4.18	+28.2%	-3.3%	+5.0%
0.55	3.25	-3.4%	-3.0%	+4.4%
0.65	3.19	-8.8%	-2.5%	+4.1%
0.75	2.97	-6.5%	-2.4%	+3.4%
0.85	2.46	-3.7%	-2.0%	+3.3%

**Table 6.5:** Summary of the antideuteron systematic errors.

$p_t$ (GeV/c)	background estimate	energy loss and absorp. corr	efficiency corr. (track cuts)	total
0.45	3%	28%	10%	30%
0.55	<1%	5%	8%	9%
0.65	<1%	5%	8%	9%
0.75	10%	5%	5%	12%
0.85	40%	5%	5%	41%

To test the effect of the energy loss correction, the analysis was done without applying the correction. The variation, given in Table 6.4, is 30% for the lowest transverse momentum bin and less than 10% elsewhere.

The annihilation correction of the yield depends on the cross section scaling factor. Indeed, based on [60], the scale factor depends on the target material and ranges from 1.63 for hydrogen to 1.22 for nitrogen. Changing the scale factor within that range changes the yield by less than 5% (see Table 6.4).

The concluding estimates based on these checks are given in Table 6.5, together with a total systematic uncertainty for each transverse momentum bin. The uncertainty in the lowest bin is dominated by the large energy loss and absorption correction, whereas the highest bin suffers from the low signal-to-background ratio.

### 6.4.2 Antihelium-3 Analysis

The  ${}^3\overline{\text{He}}$  signal, observed within the  $dE/dx$  or the equivalent  $Z$  cut, is nearly background free — unlike the  $\overline{d}$  — and therefore no background contribution is subtracted. At the same time, 99% of the total signal is included in the  $\pm 3\sigma$  range. To test the uncertainty of the background assumption the  $dE/dx$  cut is widened, as the statistics in a single transverse momentum bin is not sufficient to perform a combined signal+background fit. The results in Table 6.6 show, that the yield increases only for the three lower bins in  $p_t$ . Except for  $p_t = 0.5$  GeV/c, the change is less than 5%, so the background is concentrated at low momentum. This is in agreement with the expectation of an antitriton contribution to the  ${}^3\overline{\text{He}}$  signal, which increases for decreasing  ${}^3\overline{\text{He}}$  momentum (see Figure 6.2).

**Table 6.6:** Antihelium-3 raw yield for different  $dE/dx$  cuts.

$p_t$ (GeV/c)	$-0.127 < Z < 0.25$ $0.88 < \frac{dE/dx}{I_{BB}} < 1.28$	$-0.2 < Z < 0.25$ $0.82 < \frac{dE/dx}{I_{BB}} < 1.28$	$-0.127 < Z < 0.4$ $0.88 < \frac{dE/dx}{I_{BB}} < 1.5$
0.5	4	9	4
1.5	44	46	45
2.5	76	78	78
3.5	52	52	53
4.5	13	13	13
5.5	4	4	4

The uncertainty of the efficiency corrections is again tested by varying the track quality cuts. The observed variations are on the same level as the statistical uncertainties. The efficiency uncertainty is therefore estimated to be similar to that of  $\overline{d}$ .

The absorption correction factor is larger for  ${}^3\overline{\text{He}}$  than for  $\overline{d}$  and might thus introduce a larger systematic uncertainty. However, this is the case only at the lowest transverse momentum bin, otherwise the uncertainty is at the same level as for the  $\overline{d}$  analysis.

Table 6.7 summarizes the systematic uncertainties for the  ${}^3\overline{\text{He}}$  analysis. The first bin suffers from the very large systematic uncertainty, which is caused by the unknown background contribution.

## 6.5 Results

Finally, the invariant yield for the observed antinuclei can be calculated with the given corrections. The invariant yield, integrated over the azimuthal angle

**Table 6.7:** Summary of the antihelium-3 systematic errors.

$p_t$ (GeV/c)	background estimate	energy loss and absorp. corr	efficiency corr. (track cuts)	total
0.5	100%	50%	20%	115%
1.5	5%	8%	8%	12%
2.5	5%	5%	8%	11%
3.5	2%	5%	5%	7%
4.5	<1%	5%	5%	7%
5.5	<1%	5%	5%	7%

$\phi$ , is defined as

$$\begin{aligned}
 E \frac{d^3 N}{dp^3} &= \frac{1}{2\pi} \frac{d^2 N}{p_t dy dp_t} \\
 &= \frac{1}{2\pi p_t} \frac{N(p_t, y) \times abs_{corr}(p_t)}{N_{event} \times eff(p_t, y) \times \Delta y \Delta p_t}, \quad (6.9)
 \end{aligned}$$

where  $N(p_t, y)$  is the raw yield in the  $(p_t, y)$  bin,  $N_{event}$  the total number of events in the analyzed data set,  $abs_{corr}(p_t)$  and  $eff(p_t, y)$  the absorption and efficiency corrections described in the previous sections, and  $\Delta y, \Delta p_t$  the bin width in rapidity and transverse momentum, respectively.

The invariant cross section  $E \frac{d^3 \sigma}{dp^3}$  can be calculated by multiplying Equation 6.9 with the total inelastic hadronic cross section  $\sigma_{hadronic}$  and the trigger probability  $\sigma_{trig}$ , i.e. centrality. The total hadronic inelastic cross section for AuAu collisions at  $\sqrt{s_{nn}} = 200$  GeV is 7.2 barn, derived from the Glauber Model.

The calculation of the invariant multiplicity spectra will conclude the description of the antinuclei analysis. The discussion of the results and their interpretation with respect to the introduced coalescence models will follow in the next chapter.

### 6.5.1 Antideuteron Invariant Yield

The  $\bar{d}$  invariant yield is extracted in the transverse momentum range  $0.4 < p_t < 0.9$  GeV/c and rapidity  $|y| < 0.3$  (thus  $\Delta y = 0.6$ ). As seen in the previous sections, the background contribution dominates the signal observed above  $p_t > 0.9$  GeV/c. The selected rapidity range restricts the analysis to the region with high reconstruction efficiency. The transverse momentum spectrum is shown in Figure 6.16. Here, the error bars include both statistical and systematic contributions. The results of the 130 GeV data are included for comparison. The invariant yield within the region of small uncertainties, i.e.  $0.5 < p_t < 0.8$  GeV/c, is found to be  $[3.14 \pm 0.05(stat.) \pm 0.18(sys.)] \times 10^{-3} (\text{GeV}/c)^{-2}$ .

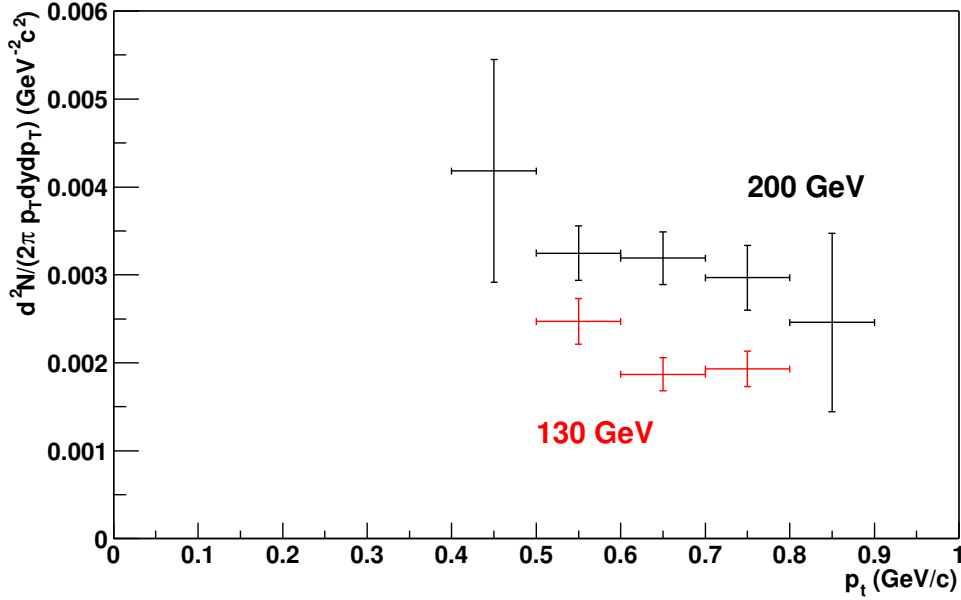


**Figure 6.16:** Antideuteron transverse momentum spectrum for 130 GeV (red) and 200 GeV (black) central AuAu data. The error bars include both statistical and systematic uncertainties.

### 6.5.2 Antihelium-3 Invariant Yield

For the first time in heavy ion physics the statistics of the antihelium-3 measurement is sufficient to calculate a differential invariant yield as a function of transverse momentum. The raw yield  $N_{3\overline{He}}(p_t, y)$  is therefore first corrected for efficiency  $eff(p_t, y)$  and integrated over rapidity to get the yield as a function of  $p_t$  only. Afterwards, the yield is corrected for absorption and normalized by the number of events and the bin width  $n \times \Delta y \Delta p_t$ . Here, the bin width includes all bins where STAR has acceptance, i.e.  $n = 4$  for  $p_t < 2$  GeV/c and  $n = 6$  for  $p_t > 2$  GeV/c (see Figure 6.13). The bin size used in the analysis is  $\Delta p_t = 1$  GeV/c and  $\Delta y = 1/3$ . The resulting transverse momentum spectrum is shown in Figure 6.17. Due to the unknown background contribution and very low statistics, the lowest and highest bins are discarded.

## 6.6 Antiproton Invariant Yield

The calculation of the coalescence parameters requires the antiproton spectra. Therefore, the antiproton analysis, done by O. Barannikova, shall be briefly introduced.

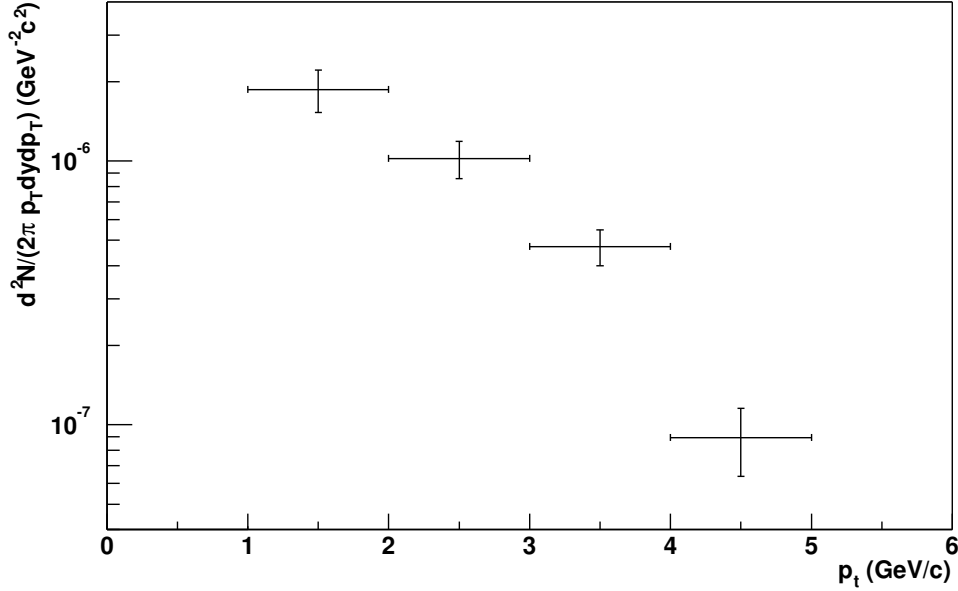


**Figure 6.17:** Antihelium-3 transverse momentum spectrum. The error bars include both statistical and systematic contributions.

The  $\bar{p}$  yield [61] is extracted in the same way from the  $dE/dx$  measurement as  $\bar{d}$ , in the transverse momentum region  $0.35 < p_t < 1.2$  GeV/c and rapidity  $|y| < 0.1$ . To determine the centrality dependence, this was done for 9 centrality bins using the minimum bias data set of AuAu collisions at 200 GeV (and full magnetic field). The invariant yield for the centrality bins 0 – 5% and 5 – 10% is shown in Figure 6.18. The error bars give the statistical uncertainties only, systematic uncertainties are less than 10%.

The distributions can be described by a Gaussian parametrization,

$$E \frac{d^3 N}{dp^3} = \frac{N}{2\pi\sigma} \exp\left(-\frac{p_t^2}{2\sigma^2}\right). \quad (6.10)$$

The fit parameters are  $N = 28.7 \pm 0.3$  [ $22.9 \pm 0.2$ ] and  $\sigma = 0.894 \pm 0.006$  [ $0.861 \pm 0.006$ ] for 0 – 5% [5 – 10%] centrality. A Boltzmann fit as a function of transverse mass  $m_t = \sqrt{m_0^2 + p_t^2}$  (see Chapter 7.2) cannot adequately describe the distribution in the full  $p_t$  region. The inverse slope depends strongly on the fit range and yields  $(710 \pm 40)$  MeV [( $570 \pm 30$ ) MeV] for 0 – 5% [5 – 10%] centrality, whereas the uncertainty due to the different fit regions is included. To allow a comparison of the antiproton results to the antinuclei results extracted for 0 – 10% centrality, the arithmetic mean of the invariant  $\bar{p}$  yields of the two centrality bins is taken in the following discussion of the results.



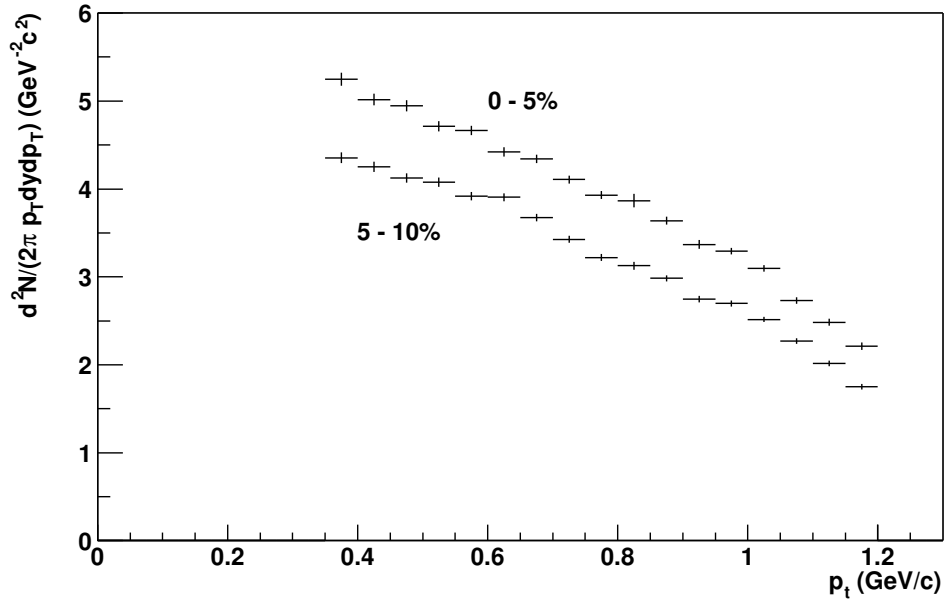


**Figure 6.18:** Antiproton transverse momentum spectra for the two centrality bins 0 – 5% (upper curve) and 5 – 10% (lower curve). The error bars are statistical only.

It is important to note, that the antiproton yield shown above is to some fraction disturbed by weak decaying strange baryons, e.g.  $\bar{\Lambda} \rightarrow \bar{p} + \pi^+$ , which generate a  $\bar{p}$  signal not originating from the fireball. This contribution cannot be fully excluded during the analysis, but is corrected afterwards based on the measured antihyperon yield. However, this is still an ongoing analysis. Here, an estimate based on the UrQMD model is used, as for the analysis of the 130 GeV data [44]. According to that model, only  $(55 \pm 10)\%$  of the measured  $\bar{p}$  originate from the fireball and not from weak decays. Unfortunately, the systematic uncertainty of the corrected  $\bar{p}$  yield is now dominated by the large uncertainty of this preliminary weak-decay correction.



# Chapter 7

## Discussion

As introduced in the first chapter, antinuclei are a rare, but very sensitive probe of the freeze-out conditions of heavy-ion collisions. This chapter shall therefore discuss the conclusions, which can be drawn from the presented antideuteron and antihelium-3 measurement.

A statistical analysis of the cluster yields can be used to estimate the global properties chemical potential and temperature at *kinetic* freeze-out. Here, the argumentation will follow along the same line as for the statistical analysis of the hadron gas found after the *chemical* freeze-out. The transverse momentum spectra carry additional information on the conditions at kinetic freeze-out, and will allow to address the question of transverse flow. Finally, in the interpretation of the coalescence parameters within the model of Scheibl and Heinz, “volumes of homogeneity” can be extracted and a comparison can be made to the results of HBT correlation measurements.

### 7.1 Antinuclei Abundance

Hadron detectors, like the STAR experiment, are sensitive to the thermodynamic conditions after chemical freeze-out, i.e. after inelastic collisions within the fireball ceased. The chemical freeze-out fixes the chemical composition, but the system undergoes further development — it further cools down by expansion until, finally, even elastic collisions cease and the system freezes-out kinetically. At this time, also the momentum distribution of the produced particles is fixed. Light clusters observed in the detector are produced just before kinetic freeze-out, as the small binding energy, e.g. 2.2 MeV for the deuteron, makes them very fragile objects, which are likely to break-up in the frequent collisions occurring earlier.

The hadron production in  $AA$ , as well as in elementary  $e^+e^-$  and  $pp$  collisions, can be very successfully described by statistical models, which are based on the tools of statistical physics: the grand-canonical ensemble with global

baryon, strangeness and charge conservation, as introduced in the first chapter. Following this picture, originally going back to Hagedorn [7], the particle yields are statistically populated in apparent thermal and chemical equilibrium according to the available phase-space at freeze-out temperature  $T$  and chemical potential  $\mu_b$ . Applied to STAR data at 130 and 200 GeV, the statistical analysis [12, 62] yields a temperature of approximately 175 MeV and a chemical potential of 45 MeV at chemical freeze-out. For a recent overview of the statistical analysis for the different systems and energies see for example [64]. Now, does the same statistical behavior hold true for the nuclei produced just before kinetic freeze-out through final-state coalescence?

Following the introduction in Chapter 1.1.1, the invariant multiplicity for particles with a chemical potential  $\mu$  and energy  $E$  in thermal and chemical equilibrium is given by

$$\frac{d^3N}{dp^3} = \frac{gV}{(2\pi)^3} \exp\left(-\frac{E - \mu}{T}\right), \quad (7.1)$$

based on the grand-canonical ensemble. Here,  $V$  and  $T$  are the volume and temperature of the source,  $g$  is the spin degeneracy factor. It is further assumed, that the chemical potentials of baryons  $\mu_b$ , antibaryons  $\mu_{\bar{b}}$  and (anti)-nuclei  $\mu_{A,\bar{A}}$  with mass number  $A$  are related as

$$\mu_{\bar{b}} = -\mu_b \quad \text{and} \quad \mu_{A,\bar{A}} = A \cdot \mu_{b,\bar{b}}. \quad (7.2)$$

Figure 7.1 shows the invariant yield for protons, antiprotons, nuclei as well as antinuclei as a function of mass number  $A$  from the NA52 minimum bias measurement [56, 65] at SPS energy and the STAR results at top RHIC energy. The statistical behavior, which follows the exponential distribution of Equation 7.1, is striking. The lines in Figure 7.1 represent a fit of the function (with proton mass  $m_p$ )

$$\frac{d^3N}{dp^3} = C \exp\left(-\frac{(m_p \pm \mu_b)A}{T}\right) \quad (7.3)$$

to the data, yielding a temperature of 130 MeV and a chemical potential of about 5 MeV for the STAR results. The uncertainties of both  $T$  and  $\mu_b$  are in the order of 15 MeV. A comparison of the results from AGS [66], SPS and RHIC is given in Table 7.1, which shows a temperature saturation and an almost vanishing chemical potential as a function of collision energy.

Indeed, the results imply, that nuclei and antinuclei freeze-out chemically, governed by the available phase-space in the same way as the hadronization process. As expected, the freeze-out temperature of clusters is lower, since the chemical freeze-out of clusters coincides with the kinetic freeze-out of the fireball.

This analysis made no assumptions on the details of the coalescence process itself, but is based exclusively on the statistical view of the hadronization and clusterization process. The coalescence model [23], which will be discussed

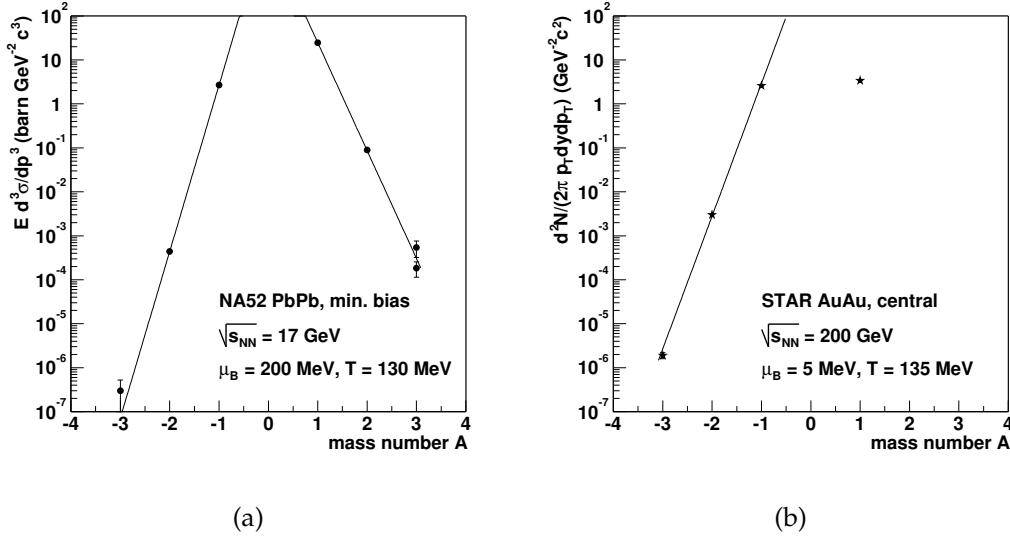


**Figure 7.1:** Proton, antiproton and cluster invariant yield as a function of mass number  $A$ . Left figure (a) shows NA52 minimum bias PbPb data at SPS energy [56, 65]. The STAR data is shown in the right figure (b).

in the last section of this chapter, treats the cluster formation in detail and includes a dynamically expanding source. This is not complementary, but a refinement of the statistical view and based on similar assumptions.

**Table 7.1:** Freeze-out temperature  $T$  and chemical potential  $\mu_b$  from the statistical analysis of the proton, antiproton and cluster abundance for different collision energies. The uncertainties are in the order of 10 to 15 MeV.

	$\sqrt{s_{NN}}$ (GeV)	$T$ (MeV)	$\mu_b$ (MeV)
AGS: E864, central AuPt	4.6	110	500
SPS: NA52, min. bias PbPb	17	130	200
RHIC: STAR, central AuAu	130	135	15
RHIC: STAR, central AuAu	200	135	5

## 7.2 Inverse Slope and Mean Transverse Momentum

The shape of the transverse momentum spectra of the emitted particles is determined at the kinetic freeze-out and carries information on the dynamics at this stage. The spectra are commonly characterized by a Boltzmann fit in

transverse mass  $m_t = \sqrt{m^2 + p_t^2}$  (see Equation 1.9 in Chapter 1.1.1),

$$E \frac{d^3 N}{dp^3} = \frac{dn/dy}{2\pi T^*(m + T^*)} e^{-\frac{m_t - m}{T^*}}, \quad (7.4)$$

where the fit parameters are the inverse slope  $T^*$  and the rapidity density  $dn/dy$ . The inverse slope  $T^*$  can be interpreted as an effective temperature of the hadronic system at freeze-out, constant for all particle species in  $pp$  collisions,

$$T_{pp}^* \simeq a, \quad (7.5)$$

and found to be almost linearly mass dependent for  $AA$  collisions [67],

$$T_{pp}^* \simeq a + bm. \quad (7.6)$$

Here,  $a$  can be taken as a common kinetic freeze-out temperature for both systems and is identical with the freeze-out temperature extracted from the statistical analysis of the cluster yields described above. The mass dependent blue-shift of the temperature parameter of the transverse mass spectra, observed in  $AA$  collisions is well understood and a direct consequence of the collective transverse motion (see for example [68], which originally goes back to the idea of blast waves [69]). This is caused by the pressure gradient between the vacuum and the hot and dense matter which cools by an explosion-like expansion. Due to their mass, the momentum spectra of (anti)nuclei should therefore exhibit the largest blue-shift of the inverse slope parameter.

Polleri [25] showed, that cluster spectra are not only sensitive to collective flow, but also to the phase-space density of the underlying nucleon source. The mass dependence of the cluster inverse slope can only be reproduced in the coalescence picture, if a box-like density profile for the protons is assumed, instead of a Gaussian profile. Otherwise, the inverse slope for the cluster of  $A$  nucleons depends only on the nucleon mass  $m_n$  instead of  $A \cdot m_n$ , leading to a constant slope for all clusters contrary to the observations. Unlike a box-like profile, a Gaussian profile gives too much weight to the region in the middle of the fireball where the transverse flow is weak.

The limited momentum coverage of the antideuteron identification prevents a meaningful fit of the Boltzmann function (Equation 7.4) to the transverse momentum spectrum. Figure 7.2 shows the antihelium-3 transverse momentum spectrum, where the exponential function in  $m_t$  is fitted to the data in the region with high statistics (black curve), i.e.,  $1.0 < p_t < 4.0$  GeV/c. The fit yields an inverse slope  $T^* = 950 \pm 140$  MeV and a rapidity density of  $(6.2 \pm 0.5) \times 10^{-5}$ . The uncertainties include both the statistical and systematic contributions. If the last data point at  $p_t = 4.5$  GeV/c is included in the fit (red curve), the parameters change to  $750 \pm 60$  MeV and  $(5.8 \pm 0.4) \times 10^{-5}$ . The  ${}^3\overline{\text{He}}$  inverse slope is indeed much larger than the  $\bar{p}$  slope of about  $650 \pm 50$

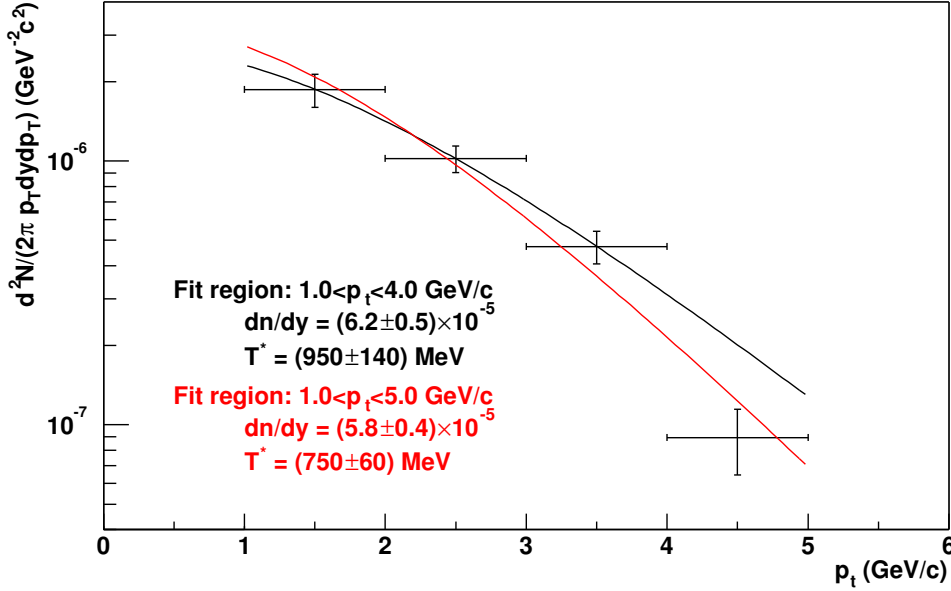


**Figure 7.2:** Antihelium-3 transverse momentum spectrum with the Boltzmann exponential fit (see text). The error bars include both statistical and systematic errors.

MeV (see Chapter 6.6). Again, this can be taken as a clear indication of collective transverse flow, similar to the SPS results, e.g. the deuteron slope measured by NA49 [70] or NA44 [67], and supports Polleri's conclusion of an underlying box-like density profile for antiprotons.

In general, the inverse slope depends strongly on the fitted momentum region. This is not the case for the mean transverse momentum  $\langle p_t \rangle$ , which can be extracted from the parameterization providing the best description of the spectra. The mean transverse momentum for  ${}^3\overline{\text{He}}$ , extracted from the Boltzmann parameterization, is  $\langle p_t \rangle = 2.6 \pm 0.4$  GeV/c, whereas the variation due to the possible fit regions is included in the uncertainty.

Figure 7.3 illustrates the mass dependence of  $\langle p_t \rangle$  (the values for  $\pi$ ,  $K$  and  $\overline{p}$  are taken from [61]). To first order, a linear mass dependence is observed with a common average transverse velocity  $\langle v_t \rangle$  for the observed hadrons,

$$\langle p_t \rangle = m \langle \gamma_t v_t \rangle, \quad (7.7)$$

where  $\gamma_t = (1 - \langle v_t \rangle^2)^{-1/2}$ . This behavior is reproduced by hydrodynamical models in a natural way, as these models describe the dynamical evolution of the fireball by the equations of ideal fluid dynamics [71]. However, even microscopic cascade models like RQMD [72] can — to some extent — reproduce this behavior.

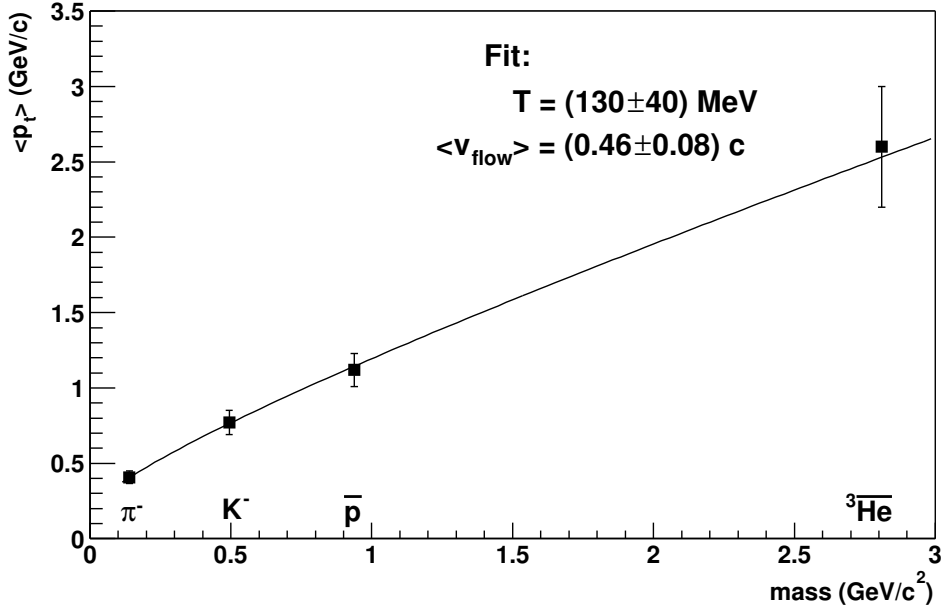


**Figure 7.3:** Mass dependence of the mean transverse momentum for AuAu collisions at 200 GeV and 10% centrality [61]. The error bars include systematic uncertainties (10% for  $\pi$ ,  $K$  and  $\bar{p}$ ). The line shows a fit to the data based on simple assumptions (see text).

The transverse velocity is a superposition of the average thermal velocity in transverse direction and the collective flow velocity. Extracting both the freeze-out temperature and the collective flow velocity profile from single-particle spectra is generally not possible, as temperature and velocity are correlated [68]: A small velocity and high freeze-out temperature can fit the  $m_t$  spectra equally well as a high velocity with a lower freeze-out temperature. The ambiguity can be resolved by a combination of different analyzes, for example  $m_t$  spectra and Hanbury-Brown Twiss correlation measurements [73, 74].

However, collective flow in the final phase-space distribution of the fireball clearly dominates the shape of the cluster spectra. Therefore, the  ${}^3\overline{\text{He}}$  measurement provides the unique opportunity to determine directly an upper limit for the average transverse flow velocity, since the average thermal velocity becomes small and  $\langle v_t \rangle_{{}^3\overline{\text{He}}} \gtrsim \langle v_{\text{flow}} \rangle$ . Using Equation 7.7 yields a limit of  $\langle v_{\text{flow}} \rangle \lesssim (0.68 \pm 0.06)c$ .

To be more precise, one can treat the hadron gas as an ideal gas in thermodynamical equilibrium, so the mean kinetic energy in transverse direction at temperature  $T$  is  $kT = mc^2(\langle \gamma_{\text{therm}} \rangle - 1)$  with  $\gamma_{\text{therm}} = (1 - \langle v_{\text{therm}} \rangle^2)^{-1/2}$ . Here,  $\langle v_{\text{therm}} \rangle$  is the average velocity of the thermal motion in transverse direction.



Now, using the relativistic addition of the velocities  $\langle v_{flow} \rangle$  and  $\langle v_{therm} \rangle$ , one can express — in a rather lengthy expression —  $\langle p_t \rangle$  as a function of temperature, average transverse flow velocity and the particle mass:

$$\langle p_t \rangle = \frac{m \left( \sqrt{\frac{T(2m+T)}{(m+T)^2}} + \langle v_{flow} \rangle \right)}{\left( 1 + \sqrt{\frac{T(2m+T)}{(m+T)^2}} \langle v_{flow} \rangle \right) \sqrt{1 - \frac{\left( \sqrt{\frac{T(2m+T)}{(m+T)^2}} + \langle v_{flow} \rangle \right)^2}{\left( 1 + \sqrt{\frac{T(2m+T)}{(m+T)^2}} \langle v_{flow} \rangle \right)^2}}}} \quad (7.8)$$

Together with the  ${}^3\overline{\text{He}}$  value, the  $\langle p_t \rangle$  measurement in STAR covers a mass region of almost 3 GeV/c<sup>2</sup> and a fit of Equation 7.8 to the data, treating  $T$  and  $\langle v_{flow} \rangle$  as free parameters, becomes feasible. The result is illustrated in Figure 7.3. One finds a temperature of  $(130 \pm 40)$  MeV and a average transverse flow velocity of  $(0.46 \pm 0.08) c$ . The good agreement with the statistical analysis and previous combined HBT/ $m_t$  spectra analyzes at SPS [73, 74] and RHIC [75] is surprising and indicates the validity of the assumptions.

The thermalization of the system manifests not only in the absolute yield of hadrons and nucleon clusters, as seen above, but also in the distribution of the mean transverse momentum and therefore in the shape of the spectra, together with the collective transverse flow. However, the agreement with SPS data is also remarkable. Naively, one expects a larger collective transverse flow at RHIC, due to the much larger initial energy density compared to SPS.

Similar transverse flow velocities at SPS and RHIC were predicted by hydrodynamical model calculations [71], where a first-order phase transition from a partonic to a hadronic phase and — at RHIC — an kinetic freeze-out occurring early after hadronization were assumed. Dumitru and Rischke argued, that the partonic phase takes much longer at RHIC until it decays into the hadronic phase, but favor also a very early kinetic freeze-out occurring almost immediately after hadronization. Accordingly, in this picture a larger transverse flow cannot be developed at RHIC during the short intermediate phase.

### 7.3 Coalescence Parameter

The coalescence parameter  $B_A$  relates the invariant yields of clusters with mass number  $A$  to that of (anti)protons and is defined by the equation

$$E_A \frac{d^3 N_A}{d^3 p_A} = B_A \left( E_p \frac{d^3 N_p}{d^3 p_p} \right)^A, \quad \text{with } p_p = p_A/A. \quad (7.9)$$

The presented  $\bar{d}$  and  ${}^3\overline{\text{He}}$  spectra, together with the simultaneous  $\bar{p}$  measurement, allow to calculate both  $B_2$  and  $B_3$  as a function of transverse momentum. As only  $\bar{p}$  produced directly by the source participate in antinuclei coalescence, the  $\bar{p}$  yield is corrected for contributions from antihyperon decays

(see Chapter 6.6). The actual  $\bar{p}$  yield is taken from the  $p_t$ -Gaussian parameterization and extrapolated outside of the measured  $p_t$  range, if necessary. Tables 7.2 and 7.3 summarize the calculated coalescence parameters  $B_2$  and  $B_3$ , respectively. The given uncertainties include the statistical and systematic contributions. The uncertainty of the coalescence parameters is dominated by the preliminary weak-decay correction of the  $\bar{p}$  yield. Compared to this, the uncertainty caused by the extrapolation can be neglected. At the  $\bar{d}$  transverse momentum of  $p_t = 0.75$  GeV/c a  $B_2 = (0.41 \pm 0.2) \times 10^{-3}$  GeV<sup>2</sup>/c<sup>3</sup> and, at the mean transverse momentum  $p_t = 2.5$  GeV/c of the observed  ${}^3\overline{\text{He}}$  sample,  $B_3 = (0.15 \pm 0.1) \times 10^{-6}$  GeV<sup>4</sup>/c<sup>6</sup> is found.

**Table 7.2:**  $B_2$  as a function of the  $\bar{d}$  transverse momentum for the  $\bar{d}$  and  $\bar{p}$  invariant yields. The  $\bar{p}$  yield is corrected for weak-decay contributions. Both statistical and systematic uncertainties are included.

$p_t$ (GeV/c)	$\bar{d}$ , $E \frac{d^3N}{dp^3}$ (GeV <sup>-2</sup> c <sup>2</sup> )	$\bar{p}$ , $E \frac{d^3N}{d(p/2)^3}$ (GeV <sup>-2</sup> c <sup>2</sup> )	$B_2 \times 10^3$ (GeV <sup>2</sup> c <sup>-3</sup> )
0.55	$(3.2 \pm 0.3) \times 10^{-3}$	$(2.8 \pm 0.5)^*$	$0.41 \pm 0.2$
0.65	$(3.2 \pm 0.3) \times 10^{-3}$	$(2.75 \pm 0.5)^*$	$0.42 \pm 0.2$
0.75	$(3.0 \pm 0.4) \times 10^{-3}$	$2.7 \pm 0.5$	$0.41 \pm 0.2$
0.85	$(2.5 \pm 1.0) \times 10^{-3}$	$2.6 \pm 0.5$	$0.4 \pm 0.2$

\*  $\bar{p}$  yield extrapolated based on the  $p_t$ -Gauss fit (see Chapter 6.6)

**Table 7.3:**  $B_3$  as a function of the  ${}^3\overline{\text{He}}$  transverse momentum for the  ${}^3\overline{\text{He}}$  and  $\bar{p}$  invariant yields. The  $\bar{p}$  yield is corrected for weak-decay contributions. Both statistical and systematic uncertainties are included.

$p_t$ (GeV/c)	${}^3\overline{\text{He}}$ , $E \frac{d^3N}{dp^3}$ (GeV <sup>-2</sup> c <sup>2</sup> )	$\bar{p}$ , $E \frac{d^3N}{d(p/3)^3}$ (GeV <sup>-2</sup> c <sup>2</sup> )	$B_3 \times 10^6$ ((GeV <sup>2</sup> c <sup>-3</sup> ) <sup>2</sup> )
1.5	$(1.9 \pm 0.3) \times 10^{-6}$	$2.5 \pm 0.5$	$0.12 \pm 0.1$
2.5	$(1.0 \pm 0.2) \times 10^{-6}$	$1.9 \pm 0.4$	$0.15 \pm 0.1$
3.5	$(0.47 \pm 0.07) \times 10^{-6}$	$1.2 \pm 0.2$	$0.27 \pm 0.15$
4.5	$(0.09 \pm 0.03) \times 10^{-6}$	$(0.7 \pm 0.1)^*$	$0.26 \pm 0.15$

\*  $\bar{p}$  yield extrapolated based on the  $p_t$ -Gauss fit (see Chapter 6.6)

The coalescence parameter  $B_3$  clearly increases as a function of transverse momentum, illustrated by Figure 7.4, whereas in the small momentum region for  $\bar{d}$   $B_2$  is consistent with a constant value. This behavior is expected and a direct

consequence of the different slopes of the  ${}^3\text{He}$  and  $\bar{p}$  transverse momentum spectra and therefore of collective flow. To the extent, that the single particle spectra can be described by exponential functions in  $m_t$ , the coalescence parameter  $B_A$  follows also an exponential behavior as a function of the cluster transverse mass  $M_t = Am_t$ ,

$$B_A \propto \exp\left(\frac{M_t}{1/T_{\bar{p}}^* - 1/T_A^*}\right), \quad (7.10)$$

where  $T_{\bar{p}}^*$ ,  $T_A^*$  are the inverse slopes of the  $\bar{p}$  and cluster spectra.

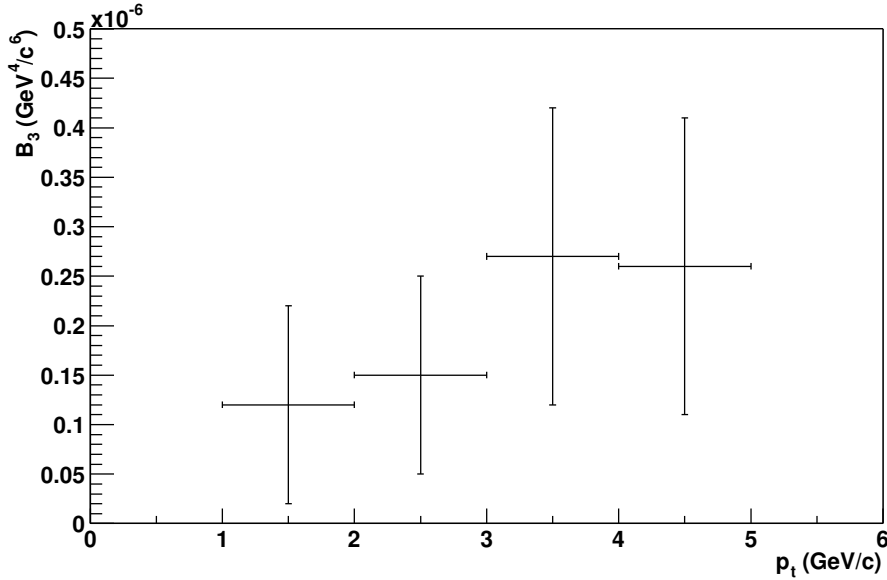


**Figure 7.4:**  $B_3$  as a function of transverse momentum.

From Equation 7.1 (see also Chapter 1.2.1) it becomes obvious, that the coalescence parameter is inversely proportional to the freeze-out volume in coordinate space,

$$B_A \propto \frac{1}{V^{A-1}}. \quad (7.11)$$

As introduced in the first chapter, an analytical expression for the source volume as a function of the coalescence parameter can be given [19]. The fireball expansion plays an important role in the coalescence process, as seen above, so it does not seem reasonable to use the simple thermal model to extract an absolute value for the freeze-out volume. However, it can serve as a common basis for a qualitative comparison of the coalescence parameters at different collision energies, which will be discussed in the following paragraph. The last section of this chapter then shall come back to the question of system size, as

the coalescence parameters are interpreted in the model of Scheibl and Heinz, which explicitly includes a transverse and longitudinal expanding source.

### 7.3.1 Collision Energy Dependence

Figure 7.5 illustrates the collision energy  $\sqrt{s_{NN}}$  dependence of the coalescence parameters  $B_2$  and  $B_3$ . Here, the values extracted from matter are marked with open symbols, filled symbols show values from antimatter. Only data (taken from [44, 66, 67, 70, 76, 78, 79, 80, 81]) from central and semi-central collisions are included, with the Exception of the NA52 [65] results, which were measured without centrality requirement (minimum bias).

The qualitative trend for both  $B_2$  and  $B_3$  is very similar: The coalescence parameter stays constant for small systems up to FNAL energies, i.e.  $pp$  and  $pA$  collisions (see [82]), indicated by the lines in Figure 7.5. In  $AA$  collisions, however, the values decrease for increasing collision energy. This can be attributed to the increasing reaction volume following Equation 7.11. Unlike in  $pp$  and  $pA$  collisions, where the reaction volume is of similar size as the intrinsic cluster size, nucleons in  $AA$  collisions, which are close in momentum space, are not necessarily close in coordinate space.

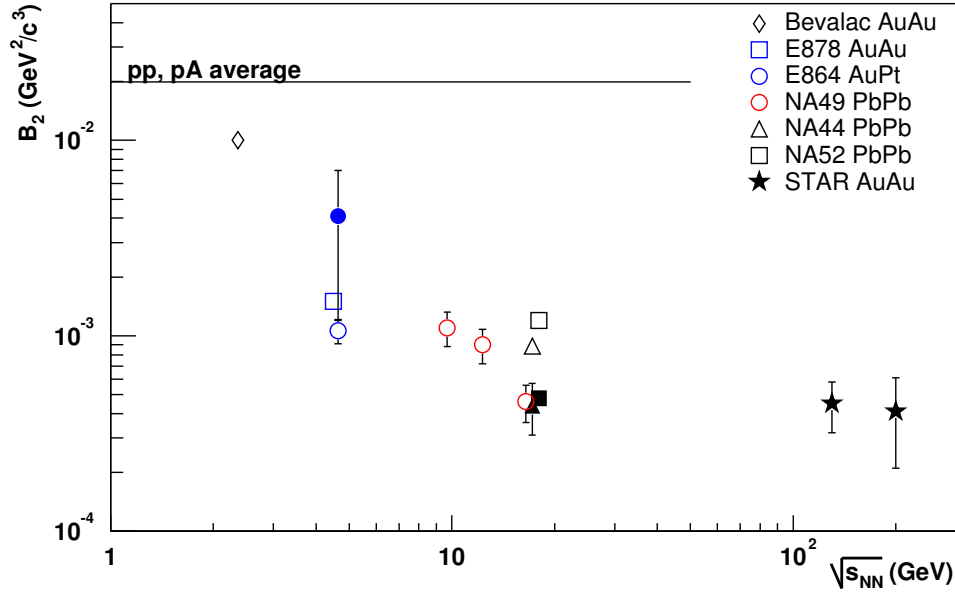
Another important aspect are the space-momentum correlations induced by collective flow, which causes particles in the same region in coordinate space to have similar momentum. These correlations therefore increase the coalescence rate. As the observed mean transverse momenta are consistent with a similar transverse flow velocities at RHIC and SPS, those concurring effects do not cancel each other, at least not for the coalescence rate of antihelium-3, where a clear decrease in  $B_3$  between SPS and RHIC can be seen.

It is worth to note, that the coalescence parameters  $B_2$  and  $B_3$  (see Figure 7.5) from matter and antimatter agree within the given error bars. This is expected from the statistical picture, where clusters freeze-out into thermal and chemical equilibrium, making no difference between clusters of matter and antimatter.

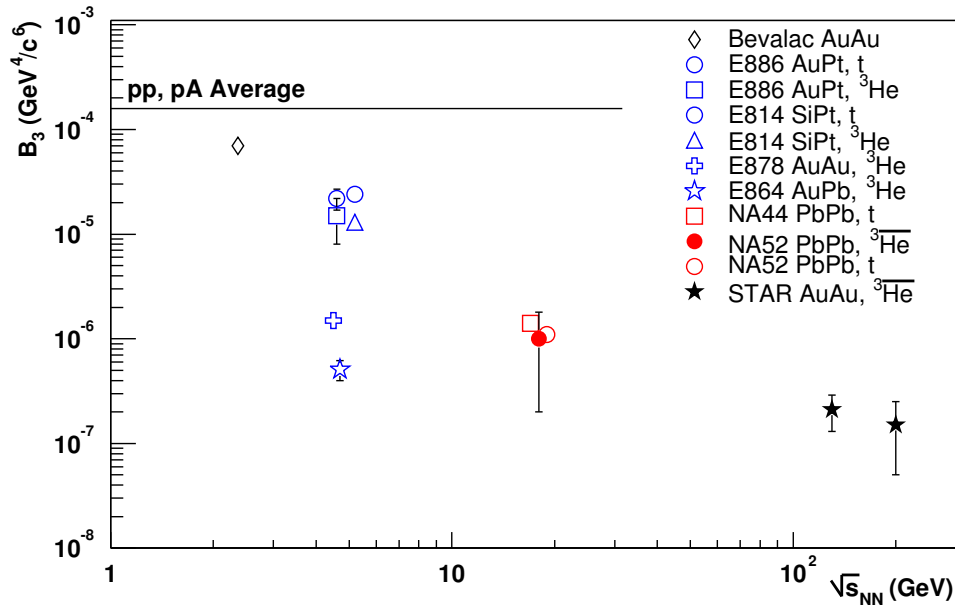
To complete the discussion of the coalescence parameters the recent results of the PHENIX experiment at RHIC (presented here [83]) should be mentioned. PHENIX measured the deuteron and antideuteron invariant yield up to  $p_t = 3.5$  GeV/c in minimum bias Au-Au data at the same beam energy as STAR. The  $B_2$  values from both  $d$  and  $\bar{d}$  are compatible with the STAR result and show a very similar  $p_t$  dependence as  $B_3$  of this analysis.

## 7.4 Volume of Homogeneity

The coalescence model of Scheibl and Heinz [23] (see Chapter 1.2.2) includes a transverse and longitudinal expanding source in the thermodynamic ansatz



(a)



(b)

**Figure 7.5:** Coalescence parameters  $B_2$  (a) and  $B_3$  (b) as a function of collision energy. Open symbols show values extracted from nuclei and filled symbols values from antinuclei. The lines indicate the average of  $B_2$ ,  $B_3$ , which are observed in  $pp$  and  $pA$  collisions, independent of the collision energy.

introduced by Mekjian [19]. However, the coalescence process is treated quantum mechanically with the density matrix (Wigner function) approach, which allows to account for energy conservation in a proper way. Polleri's result of a box-like density profile of the underlying proton and antiproton source is confirmed by the Scheibl and Heinz model.

The coalescence parameters are in this framework expressed in terms of the "volume of homogeneity", which is otherwise extracted from HBT interferometry. As the homogeneity volume [15] describes the size of fireball regions, where particles of a given momentum are emitted at kinetic freeze-out, this common relation between HBT and coalescence measurements is not surprising.

Following the notation of Scheibl and Heinz already introduced in the previous section, where the cluster transverse mass is  $M_t = A \cdot m_t$  with the nucleon transverse mass  $m_t$ , the coalescence parameter  $B_2$  and  $B_3$  are in this model given by

$$B_2 = \frac{3\pi^{3/2}\hbar^3\langle C_{\bar{d}} \rangle}{2m_t V_{hom}(m_t)} e^{2(m_t-m)(1/T_{\bar{p}}^* - 1/T_{\bar{d}}^*)}, \quad (7.12)$$

$$B_3 = \frac{2\pi^3\hbar^6\langle C_{^3\overline{\text{He}}} \rangle}{\sqrt{3}m_t^2 V_{hom}^2(m_t)} e^{3(m_t-m)(1/T_{\bar{p}}^* - 1/T_{^3\overline{\text{He}}}^*)}. \quad (7.13)$$

The homogeneity volume  $V_{hom}$  is defined by the HBT radii  $R_{\perp}$  and  $R_{\parallel}$  as

$$V_{hom}(m_t) = R_{\perp}^2(m_t)R_{\parallel}(m_t). \quad (7.14)$$

Here,  $\langle C_{\bar{d}} \rangle = 0.8$  and  $\langle C_{^3\overline{\text{He}}} \rangle = 0.7$  (taken from [23]) are the quantum mechanical correction factors to the classical form of Equations 7.12 and 7.13 (see Equation 1.17) and related to the internal structure of the  $\bar{d}$  and  $^3\overline{\text{He}}$ . The exponential factor arises from the box-like transverse density profile of the nucleons, it vanishes for a Gaussian profile. Again,  $T_{\bar{p}}^*$ ,  $T_A^*$  are the inverse slopes of the  $\bar{p}$  and cluster spectra.

According to Scheibl and Heinz, the effective volume  $V_{eff}$  for clusters with transverse mass  $M_t$  occurring in the classical approach depends explicitly on the nucleon number  $A$  and is related to  $V_{hom}$  as

$$V_{eff}(A, M_t) = \left(\frac{2\pi}{A}\right)^{3/2} V_{hom}(m_t). \quad (7.15)$$

To extract the homogeneity volume  $V_{hom}$  for  $\bar{d}$  from Equation 7.12, the exponential factor can be neglected, since the yield is measured at very low transverse momentum. The unknown  $\bar{d}$  inverse slope is therefore not needed. For both  $\bar{d}$  and  $^3\overline{\text{He}}$  similar homogeneity volumes are found:  $V_{hom,\bar{d}} = (124 \pm 50) \text{ fm}^3$  and  $V_{hom,^3\overline{\text{He}}} = (121 \pm 40) \text{ fm}^3$  (at the  $^3\overline{\text{He}}$  transverse momentum  $p_t = 2.5 \text{ GeV}/c$ ).

Figure 7.6 compares the homogeneity volumes extracted from the coalescence analysis to the pion HBT correlation results [84], as a function of the transverse momentum  $m_t$  for the 200 GeV and 130 GeV data. Within a hydrodynamical model, the HBT radii  $R_{HBT} \propto V_{hom}^{1/3}$  are predicted to drop as  $1/\sqrt{m_t}$ , as a consequence of the transverse flow [15]. Therefore, the pion HBT results were fitted with an power law  $V_{hom} \propto 1/m_t^a$  yielding  $a = 0.9 \pm 0.1$ . Even so the coalescence analysis results agree well with the HBT results within the error bars, they do not seem to follow the same  $m_t$  dependence. However, it is not clear, that the space-time geometry for pions and antinucleons should be the same and quantitative comparisons should be made carefully. More interesting would be a comparison with proton-proton correlations, for example shown by Murray for SPS data [85], but this is still an ongoing analysis in STAR.

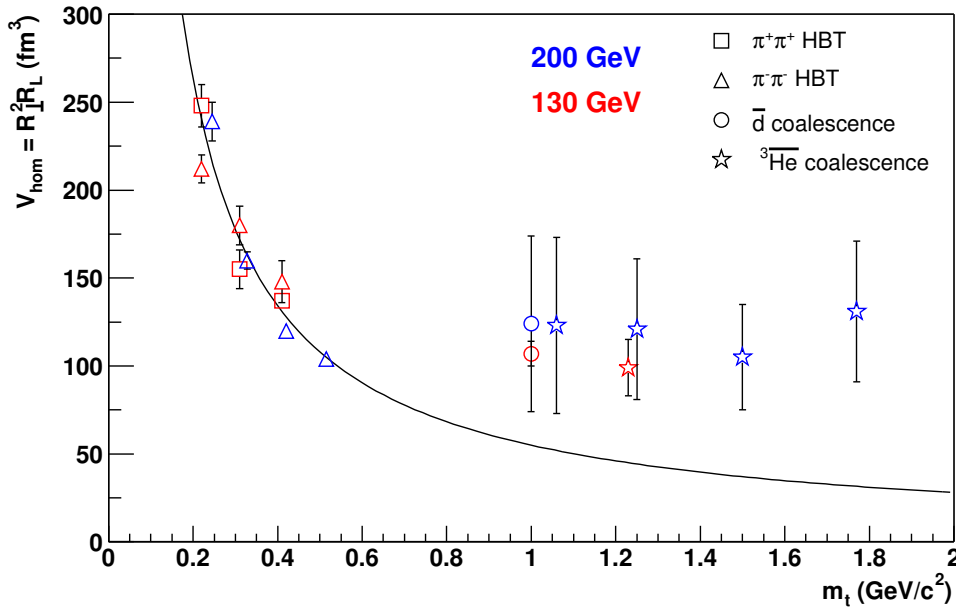


**Figure 7.6:** Homogeneity volume as a function of transverse mass extracted from pion HBT and the coalescence analysis. Red symbols show the results for the STAR AuAu data at  $\sqrt{s_{NN}} = 130$  GeV and blue symbols the results for 200 GeV. The HBT results were taken from [84].

Table 7.4 summarizes the results for the homogeneity volumes extracted from the presented antinuclei analysis of the STAR data at 200 GeV and from the previous analysis at 130 GeV. The NA44 results for  $d$  and  $t$  measurements [67] in central PbPb collisions at SPS are included in Table 7.4. Compared to SPS, the homogeneity volume increases at RHIC's top energy by about a factor of two.

This increase in the volume of homogeneity is the only difference seen in this analysis between the kinetic freeze-out conditions at SPS and RHIC, besides a lower baryon chemical potential. Both systems freeze-out at approximately the same temperature of 130 MeV and with similar collective transverse flow velocities of 0.5c. Does this imply a change in the transverse density profile of nucleons at RHIC, in the sense of a more box-like profile than at SPS, or in the duration of the system evolution and particle emission? The details will have to be answered by the theoreticians of this field.

**Table 7.4:** Homogeneity volume  $V_{hom}$  and effective volume  $V_{eff}$  (see text) extracted from the coalescence analysis of 17 GeV PbPb data [67] and 130 GeV[44], 200 GeV AuAu data in the framework of Scheibl and Heinz [23]. As before the errors for the RHIC data points include both statistical and systematical uncertainties, whereas the SPS values include statistical uncertainties only.

$\sqrt{s_{NN}}$ (GeV)	$A$	cluster $p_t$ (GeV/c)	$B_A \cdot 10^4$ (GeV <sup>2</sup> c <sup>-3</sup> ) <sup>A-1</sup>	$T_A^*$ (MeV)	$V_{hom}$ (fm <sup>3</sup> )	$V_{eff}$ (fm <sup>3</sup> )
17	$d$	0.7-1.55	$8.84 \pm 0.13$	$376 \pm 17$	$67 \pm 3$	$373 \pm 16$
17	$t$	0.68-1.6	$0.014 \pm 0.002$	$747^{+\infty}_{-380}$	$60 \pm 4$	$182 \pm 12$
130	$\bar{d}$	0.75	$4.5 \pm 1.3$		$107 \pm 7$	$600 \pm 40$
130	${}^3\bar{\text{He}}$	2.4	$0.0021 \pm 0.0012$	$700 \pm 250$	$99 \pm 16$	$299 \pm 50$
200	$\bar{d}$	0.75	$4.1 \pm 2$		$124 \pm 50$	$723 \pm 200$
200	${}^3\bar{\text{He}}$	2.5	$0.0015 \pm 0.001$	$950 \pm 140$	$121 \pm 40$	$366 \pm 120$

inverse slope  $T_A^*$  not measured for  $\bar{d}$



# Chapter 8

## Summary and Conclusion

This thesis presented the measurement of antideuteron and antihelium-3 production in central AuAu collisions at  $\sqrt{s_{NN}} = 200$  GeV center-of-mass energy at RHIC. The analysis is based on STAR data, about  $3 \cdot 10^6$  events at top 10% centrality. Within the data sample a total number of about 5000 antideuterons and 193 antihelium-3 were observed in the STAR TPC at mid-rapidity. The specific energy loss measurement in the TPC provides antideuteron identification only in a small momentum window, antihelium-3 however can be identified nearly background free with almost complete momentum range coverage.

Following the statistical analysis of the hadronic composition at chemical freeze-out of the fireball, the antinuclei abundances were analyzed in terms of the same statistical description. Now applied to the clusterization of the fireball, the statistical analysis yields a fireball temperature of  $(135 \pm 10)$  MeV and chemical potential of  $(5 \pm 10)$  MeV at kinetic freeze-out. In the same way as the hadronization, the clusterization process is phase-space dominated and clusters are born into a state of maximum entropy.

The large sample of observed antihelium-3 allowed for the first time in heavy-ion physics to calculate a differential multiplicity and invariant cross section as a function of transverse momentum. As expected, the collective transverse flow in the fireball flattens the shape of the transverse momentum spectrum and leads to the high inverse slope parameter of  $(950 \pm 140)$  MeV of the antihelium-3 spectrum.

With the extracted mean transverse momentum of antihelium-3, the collective flow velocity in transverse direction could be estimated. As the average thermal velocity is small compared to the mean collective flow velocity for heavy particles, the mean transverse momentum of antihelium-3 by itself constrains the flow velocity. Here, a simple ideal-gas approximation was fitted to the distribution of the mean transverse momentum as a function of particle mass and provided direct access to the kinetic freeze-out temperature and the flow velocity. A concept, which is complementary to the combined analysis of momentum spectra and two-particle HBT correlation methods commonly used

to extract these parameters, and a cross check for the statistical analysis. The upper limit for the transverse collective flow velocity from the antihelium-3 measurement alone is  $\langle v_{flow} \rangle \lesssim (0.68 \pm 0.06)c$ , whereas the ideal-gas approximation yields a temperature of  $(130 \pm 40)$  MeV and  $\langle v_{flow} \rangle = (0.46 \pm 0.08)c$ . The results indicate, that the kinetic freeze-out conditions at SPS and RHIC are very similar, except for a smaller baryon chemical potential at RHIC.

The simultaneous inclusive measurement of antiprotons allowed to study the cluster production in terms of the coalescence picture. With the large momentum coverage of the antihelium-3 momentum spectrum, the coalescence parameter  $B_3$  could be calculated as a function of transverse momentum. Due to the difference between antiproton and antihelium-3 inverse slopes,  $B_3$  increases with increasing transverse momentum — again a direct consequence of collective transverse flow.

Both  $B_2$  and  $B_3$  follow the common behavior of decreasing coalescence parameters as a function of collision energy. According to the simple thermodynamic coalescence model, this indicates an increasing freeze-out volume for higher energies and is confirmed by the interpretation of the coalescence parameters in the framework of Scheibl and Heinz. Their model includes a dynamically expanding source in a quantum mechanical description of the coalescence process and expresses the coalescence parameter as a function of the homogeneity volume  $V_{hom}$  accessible also in two-particle HBT correlation analyzes. The values for the antideuteron and antihelium-3 results agree well with the homogeneity volume from pion-pion correlations, but do not seem to follow the same transverse mass dependence. A comparison with proton-proton correlations may clarify this point and provide an important cross check for this analysis. Compared to SPS the homogeneity volume increases nearly by a factor of two.

The analysis of the antinuclei emission at RHIC allowed to study the kinetic freeze-out of the created fireball. The results show, that the temperature and mean transverse velocity in the expanding system does not change significantly, when the collision energy increases by one order of magnitude. Only the source volume, i.e. the homogeneity volume, increases. That leaves open questions for the theoreticians to the details of the system evolution from the initial hot and dense phase — the initial energy density is a factor of two to three higher at RHIC than at SPS — to the final kinetic freeze-out with similar conditions. At the same time, the results are important constraints for the theoretical descriptions.

The successful implementation of the Level-3 trigger system in STAR opens the door for the measurement of very rare signals. Indeed, in the coalescence physics perspective, the first observations of anti-alpha  ${}^4\overline{\text{He}}$  nuclei and anti-hypertritons  ${}^3_{\Lambda}\overline{\text{H}}$  will come within the reach of STAR, in addition to a high statistics sample of antihelium-3.

# Appendix A

## Coordinates, Variables and Definitions

### Coordinate Systems in STAR

The global Cartesian coordinate system of STAR, in which the particle trajectories and momenta are measured, is located at the center of the solenoid. The  $z$  direction is defined by the axis of the solenoid and parallel to the beam line, positive  $z$  points westward. The  $x$  axis is chosen perpendicular and positive  $x$  points approximately south, away from the center of RHIC accelerator ring. Accordingly, positive  $y$  points up.

Other coordinate systems relevant for the track reconstruction in the TPC, are the local TPC coordinates and hardware coordinates. The local TPC coordinates are identical with the global coordinates but shifted to the center of the TPC. The raw data, however, is coded in hardware coordinates. These are defined by the numbering scheme of the TPC geometry and data acquisition, i.e. sector number, pad row, pad number and time bin, and are the natural coordinates for the charge cluster reconstruction.

### Choice of Variables

The common choice of variables in heavy-ion physics is a made with respect to invariance under Lorentz transformations in beam direction. As the phase space of the produced particles is defined by the momentum components  $p_x$ ,  $p_y$  and  $p_z$ , the most convenient choice is first the transverse momentum  $p_t$ , i.e. the component perpendicular to the beam axis, and the azimuthal angle  $\Phi$ ,

$$p_t = \sqrt{p_x^2 + p_y^2} \quad (\text{A.1})$$

$$\Phi = \arctan \frac{p_y}{p_x}. \quad (\text{A.2})$$

Unlike  $p_t$ , the momentum component in beam direction  $p_z$  is not invariant and the rapidity  $y$  is chosen to describe this degree of freedom,

$$y = \frac{1}{2} \ln \left( \frac{E + p_z}{E - p_z} \right), \quad (\text{A.3})$$

where the total energy  $E$  of the particle with mass  $m$  is given by

$$E = \sqrt{p_x^2 + p_y^2 + p_z^2 + m^2}. \quad (\text{A.4})$$

The rapidity is a measure of the particle velocity and a boost along the beam axis corresponds to a simple shift in rapidity.

Another common variable, used in addition to the transverse momentum, is the transverse mass  $m_t$ , defined as

$$m_t = \sqrt{p_x^2 + p_y^2 + m^2}. \quad (\text{A.5})$$

Using these definitions, the invariant cross section  $E \frac{d^3\sigma}{dp^3}$  can be written as

$$E \frac{d^3\sigma}{dp^3} = \frac{d^3\sigma}{d\phi dy p_t dp_t} = \frac{d^2\sigma}{2\pi dy p_t dp_t}. \quad (\text{A.6})$$

For the second form, the identity  $dy/dp_z = 1/E$  was used. The third form represents the average over  $\Phi$  and accounts for the azimuthal symmetry of central collisions.

# Appendix B

## Efficiency Uncertainties with Bayesian Statistics

### Motivation

The common efficiency determination from both real data and Monte-Carlo data is an example for a binomial process, where a number of trials  $N$  and successes  $n$  are collected and the efficiency  $\epsilon$  then estimated from the ratio  $\epsilon = n/N$ . According to the binomial distribution the probability for  $n$  successes is given by

$$P(n|N, \hat{\epsilon}) = \frac{N!}{n!(N-n)!} \hat{\epsilon}^n (1 - \hat{\epsilon})^{N-n} \quad (\text{B.1})$$

with the true efficiency  $\hat{\epsilon}$ . The expectation value  $\mu$  and standard deviation  $\sigma_n$  for this distribution, found after many runs with  $N$ , trials are

$$\mu = N\hat{\epsilon}, \quad (\text{B.2})$$

$$\sigma_n = \sqrt{N\hat{\epsilon}(1 - \hat{\epsilon})}. \quad (\text{B.3})$$

The standard method to estimate the uncertainty  $\sigma_\epsilon$  of the efficiency  $\epsilon$  is then taken as

$$\sigma_\epsilon = \frac{\sigma_n}{N} = \sqrt{\frac{\epsilon(1 - \epsilon)}{N}}. \quad (\text{B.4})$$

This definition works fine for large  $N$ . However, it breaks down for small  $n$ , where the distribution of observed  $n$  becomes very asymmetric. For the extremes  $n = 0$  and  $n = N$  the calculated errors vanish in this definition. Clearly, a more rigorous approach is needed.

### The Bayesian Approach

The Bayesian statistics [86] provide a general solution in a straightforward way. Necessary for this approach is the definition of a initial probability density  $P_0(\epsilon|N)$  of the unknown efficiency  $\epsilon$ . From the Bayesian Theorem one can

then derive the probability density  $P(\epsilon|n, N)$  for  $\epsilon$ , given the observed  $n$  successes in  $N$  trials,

$$P(\epsilon|n, N) = \frac{P(n|\epsilon, N)P_0(\epsilon|N)}{P(n|N)}. \quad (\text{B.5})$$

Here,  $P(n|N)$  is the probability for the observation of  $n$ , given  $N$ , for any allowed value of  $\epsilon$ . A priori any value of  $\epsilon$  is equally likely and a uniform initial probability density can be assumed, therefore Equation B.5 gives

$$\begin{aligned} P(\epsilon|n, N) &= \frac{\frac{N!}{n!(N-n)!}\epsilon^n(1-\epsilon)^{N-n}P_0(\epsilon)}{\int_0^1 \frac{N!}{n!(N-n)!}\epsilon^n(1-\epsilon)^{N-n}P_0(\epsilon)d\epsilon} \\ &= \frac{\epsilon^n(1-\epsilon)^{N-n}P_0(\epsilon)}{\int_0^1 \epsilon^n(1-\epsilon)^{N-n}P_0(\epsilon)d\epsilon} \\ &= \frac{\epsilon^n(1-\epsilon)^{N-n}}{\int_0^1 \epsilon^n(1-\epsilon)^{N-n}d\epsilon}. \end{aligned} \quad (\text{B.6})$$

In this case, both  $n$  and  $N$  are integer numbers and the integral (the  $\beta$  function) in the denominator is simply equal to  $n!(N-n)!/(N+1)!$ . The final probability density is accordingly

$$\begin{aligned} P(\epsilon|n, N) &= \frac{(N+1)!}{n!(N-n)!}\epsilon^n(1-\epsilon)^{N-n} \\ &= (N+1)P(n|\epsilon, N). \end{aligned} \quad (\text{B.7})$$

The maximum probability occurs for this distribution at the value  $\epsilon = n/N$ . The expectation value and variance are

$$\mu = \frac{n+1}{N+2}, \quad (\text{B.8})$$

$$\begin{aligned} \sigma_\epsilon^2 &= \frac{(n+1)(N-n+1)}{(N+3)(N+2)^2} \\ &= \mu(1-\mu)\frac{1}{N+3}. \end{aligned} \quad (\text{B.9})$$

When both  $n$  and  $N$  become large, and  $0 \ll n \ll N$ , the asymptotic properties then recover the well known values (Equation B.4):

$$\mu \approx \epsilon = \frac{n}{N}; \quad (\text{B.10})$$

$$\sigma_\epsilon^2 \approx \frac{\epsilon(1-\epsilon)}{N}. \quad (\text{B.11})$$

This approach includes the special cases  $n = 0$  and  $n = N$ , where the results are given as upper and lower limits, respectively. From Equation B.6 one finds the following solutions:

- $n = N$

$$P(n = N|\epsilon, N) = \epsilon^N \quad (\text{B.12})$$

$$P(\epsilon|n = N, N) = (N + 1) \cdot \epsilon^N \quad (\text{B.13})$$

The cumulative distribution function  $F(\epsilon) = P(X \leq \epsilon) = \int_{-\infty}^{\epsilon} P(\epsilon')d\epsilon'$  is then

$$F(\epsilon|n = N, N) = \epsilon^{N+1} \quad (\text{B.14})$$

and for the 95% lower limit

$$F(\epsilon_0|n = N, N) = 0.05, \quad (\text{B.15})$$

$$\epsilon_0 = \sqrt[N+1]{0.05}. \quad (\text{B.16})$$

Thus, an increasing  $N$  constrains  $\epsilon$  more and more around 1.

- $n = 0$

$$P(n = 0|\epsilon, N) = (1 - \epsilon)^N \quad (\text{B.17})$$

$$P(\epsilon|n = 0, N) = (N + 1) \cdot (1 - \epsilon)^N \quad (\text{B.18})$$

$$F(\epsilon|n = 0, N) = 1 - (1 - \epsilon)^{N+1} \quad (\text{B.19})$$

and for the 95% upper limit

$$F(\epsilon_0|n = 0, N) = 0.95, \quad (\text{B.20})$$

$$\epsilon_0 = 1 - \sqrt[N+1]{0.05}. \quad (\text{B.21})$$





# List of Figures

1.1	Nuclear matter and quark matter at high densities . . . . .	2
1.2	Phase diagram of strongly interacting matter . . . . .	3
1.3	Fireball evolution after a central heavy ion collision . . . . .	5
1.4	Phase diagram from the statistical analysis of hadron yields . . . . .	8
2.1	Perspective view of the STAR detector . . . . .	15
2.2	Cut-away side view of the STAR detector configuration 2001 . . . . .	16
2.3	Schematic view of the STAR TPC . . . . .	18
2.4	Schematic cross-section view of the TPC read-out plane . . . . .	19
2.5	Anode pad plane layout of one full sector . . . . .	20
2.6	Acceptance of the STAR detector components for the run 2001 . . . . .	22
2.7	Correlation between summed pulse height of ZDCs and CTB . . . . .	23
2.8	Accelerator complex at BNL . . . . .	24
3.1	STAR Level-3 and DAQ architecture for the year 2001 . . . . .	28
3.2	Level-3 cluster finder in inner most and outer most TPC padrow . . . . .	33
3.3	Transverse momentum resolution for Level-3 and offline reconstruction with and without the primary vertex . . . . .	35
3.4	Tracking efficiency as a function of transverse momentum in central Au-Au collisions for Level-3 and offline . . . . .	37
3.5	Level-3 $z$ -vertex resolution relative to offline . . . . .	38
4.1	Offline $dE/dx$ for negative charged particle tracks . . . . .	40
4.2	$Z = -2$ trigger cut in $dE/dx$ versus rigidity distribution . . . . .	42
4.3	Number of space-points of the Level-3 tracks passing the $dE/dx$ trigger cut . . . . .	43
4.4	Number of fit points for the $Z = -2$ candidates from offline and Level-3 . . . . .	43
4.5	Distance of closest approach to the primary vertex of the Level-3 tracks satisfying the $dE/dx$ and the $nHits$ trigger cut . . . . .	44
4.6	Distance of closest approach to the primary vertex of the Level-3 tracks matching the offline reconstructed $Z = -2$ candidates . . . . .	45
4.7	${}^3\overline{\text{He}}$ raw yield as a function of offline transverse momentum for the offline reconstruction and the L3 algorithm . . . . .	46

4.8	$Z = -2$ trigger efficiency as a function of transverse momentum	47
4.9	Number of fit points of offline ${}^3\overline{\text{He}}$ candidates where no matching L3 candidate was found. . . . .	47
4.10	${}^3\overline{\text{He}}$ raw yield reconstructed offline from the unbiased and triggered events . . . . .	49
4.11	$dE/dx$ distribution of the offline reconstructed ${}^3\overline{\text{He}}$ candidates of the unbiased and triggered event sample . . . . .	50
4.12	${}^3\overline{\text{He}}$ invariant yield as a function of transverse momentum reconstructed offline from the unbiased and total event sample . .	50
5.1	Sum of distortion corrections . . . . .	55
5.2	Particle identification based on the ionisation $dE/dx$ in the TPC	59
5.3	$dE/dx$ resolution versus number of ionisation samples . . . . .	60
6.1	Primary vertex position for the hadronic central events . . . . .	62
6.2	Nuclei and antinuclei identification with $dE/dx$ . . . . .	63
6.3	Number of fit points for the ${}^3\overline{\text{He}}$ candidate tracks with a ratio of number of $dE/dx$ to fit points larger than 0.3 . . . . .	65
6.4	Ratio of number of $dE/dx$ points to number of fit points for the ${}^3\overline{\text{He}}$ candidate tracks with at least 30 fit points . . . . .	66
6.5	$\overline{d}$ and ${}^3\overline{\text{He}}$ energy loss correction . . . . .	67
6.6	$Z$ distribution for $\overline{d}$ . . . . .	68
6.7	$\overline{d}$ raw yield as a function of transverse momentum . . . . .	69
6.8	$\overline{d}$ signal-to-background ratio . . . . .	70
6.9	$Z$ distribution of the ${}^3\overline{\text{He}}$ signal . . . . .	71
6.10	${}^3\overline{\text{He}}$ raw yield as a function of transverse momentum and rapidity	71
6.11	$Z$ distribution for $d$ . . . . .	73
6.12	Deuteron reconstruction efficiency . . . . .	74
6.13	Helium-3 reconstruction efficiency . . . . .	74
6.14	Antiproton/proton total, elastic and annihilation cross section .	75
6.15	Absorption correction for $\overline{p}$ , $\overline{d}$ and ${}^3\overline{\text{He}}$ . . . . .	76
6.16	Antideuteron transverse momentum spectrum . . . . .	81
6.17	Antihelium-3 transverse momentum spectrum . . . . .	82
6.18	Antiproton transverse momentum spectra . . . . .	83
7.1	$p$ , $\overline{p}$ and cluster invariant yield as a function of mass number . .	87
7.2	Antihelium-3 inverse slope . . . . .	89
7.3	Mass dependence of the mean transverse momentum . . . . .	90
7.4	$B_3$ as a function of transverse momentum . . . . .	93
7.5	Coalescence parameters $B_2$ and $B_3$ as a function of collision energy	95
7.6	Homogeneity volume as a function of transverse mass extracted from pion HBT and the coalescence analysis . . . . .	97

# List of Tables

2.1	Summary of the STAR TPC parameters . . . . .	21
4.1	Summary of the $Z = -2$ cuts and event rate of the L3 and offline reconstruction . . . . .	41
4.2	Number of unbiased events and additional events analyzed by Level-3 for the hadronic central trigger (with full magnetic field)	49
5.1	The distortion corrections applied to STAR data; their cause, and the magnitude of their effect on the data [28]. . . . .	55
6.1	Summary of the cuts applied in the antinuclei analysis . . . . .	64
6.2	Uncorrected Antideuteron yield for different fit ranges . . . . .	77
6.3	Antideuteron invariant yield for different track quality cuts . . . . .	78
6.4	Antideuteron invariant yield for different correction parameters . . . . .	78
6.5	Antideuteron systematic errors . . . . .	78
6.6	Antihelium-3 raw yield for different $dE/dx$ cuts . . . . .	79
6.7	Antihelium-3 systematic errors . . . . .	80
7.1	Freeze-out temperature $T$ and chemical potential $\mu_b$ from the statistical analysis of the proton, antiproton and cluster abundance	87
7.2	$B_2$ for the measured $\bar{d}$ and $\bar{p}$ invariant yields . . . . .	92
7.3	$B_3$ for the measured ${}^3\overline{\text{He}}$ and $\bar{p}$ invariant yields . . . . .	92
7.4	Homogeneity volumes and effective volumes extracted from the coalescence analysis for 17, 130 and 200 GeV data . . . . .	98



# Bibliography

- [1] J. C. Collins and M. J. Perry, Phys. Rev. Lett. **34** (1975) 1353
- [2] N. K. Glendenning, Phys. Rev. Lett. **63** (1989) 2629
- [3] E. Learmann, Nucl. Phys. **A610** (1996) 1c
- [4] J. W. Harris and B. Müller, Annu. Rev. Nucl. Part. Sci. **46** (1996) 71
- [5] CERN press release (2000), available at  
<http://cern.ch/CERN/Announcements/2000/NewStateMatter>
- [6] H. J. Specht, Nucl. Phys. **A698** (2002) 341c
- [7] R. Hagedorn, Nuovo Cimento **35** (1965) 395
- [8] J. Letessier and J. Rafelski, *Hadrons and Quark Gluon Plasma*, Cambridge University Press (2002)
- [9] P. Koch, B. Müller and J. Rafelski, Phys. Rep. **142** (1986) 167; F. Becattini, Z. Phys. C **69** (1996) 485; J. Letessier, J. Rafelski and A. Tounsi, Nucl. Phys. **A590** (1995) 613; P. Braun-Munzinger, P. Heppe and J. Stachel, Phys. Lett. **B465** (1999) 15
- [10] R. Stock, Nucl. Phys. **A661** (1999) 282
- [11] P. Braun-Munzinger, Nucl. Phys. **A681** (2001) 119
- [12] P. Braun-Munzinger, D. Magestro, K. Redlich and J. Stachel, Phys. Lett. **B518** (2001) 41
- [13] U. Heinz, Nucl. Phys. **A661** (1999) 140c
- [14] S. Mrówczyński, Phys. Lett. **B248** (1990) 459; Phys. Lett. **B277** (1992) 43; Phys. Lett. **B345** (1995) 393
- [15] For a detailed description of this method and the application to heavy ion collisions see for example U. A. Wiedemann and U. Heinz, Phys. Rep. **319** (1999) 145

- [16] S. T. Butler and C. A. Pearson, *Phys. Rev.* **129** (1963) 839
- [17] A. Schwarzschild and C. Zupancic, *Phys. Rev.* **129** (1963) 854
- [18] H. H. Gutbrod *et al.*, *Phys. Rev. Lett.* **37** (1976) 667
- [19] A. Mekjian, *Phys. Rev. Lett.* **38** (1977) 640; *Phys. Rev.* **C17** (1978) 1051;  
S. Das Gupta and A. Mekjian, *Phys. Rep.* **72** (1981) 131
- [20] W. L. Llope *et al.*, *Phys. Rev.* **C52** (1995) 2004
- [21] H. Sato and K. Yazaki, *Phys. Lett.* **98B** (1981) 153
- [22] R. Mattiello, H. Sorge, H. Stöcker and W. Greiner, *Phys. Rev.* **C55** (1997) 1443
- [23] R. Scheibl and U. Heinz, *Phys. Rev.* **C59** (1999) 1585
- [24] R. Hagedorn, *Phys. Rev. Lett.* **5** (1960) 276
- [25] A. Polleri, J. P. Bondorf and I. N. Mishustin, *Phys. Lett.* **B419** (1998) 19;  
A. Polleri, R. Mattiello, I. N. Mishustin and J. P. Bondorf, *Phys. Lett.* **B473** (2000) 193
- [26] C. Adler *et al.*, STAR Coll., nucl-ex/0206004, *subm. to Phys. Rev. Lett.*
- [27] F. Bergsma *et al.*, *The STAR Detector Magnet Subsystem*, to be published in [36]
- [28] M. Anderson *et al.*, *The STAR Time Projection chamber: A Unique Tool for Studying High Multiplicity Events at RHIC*, to be published in [36]
- [29] K. H. Ackermann *et al.*, *The Forward Time Projection Chamber (FTPC) in STAR*, to be published in [36]
- [30] R. Bellwied *et al.*, *The STAR Silicon Vertex Tracker: A Large Area Silicon Drift Detector*, to be published in [36]
- [31] A. Bream *et al.*, *Identification of High  $p_t$  Particles with the STAR-RICH Detector*, to be published in [36]
- [32] M. Beddo *et al.*, *The STAR Barrel Electromagnetic Calorimeter*, to be published in [36]
- [33] F. S. Bieser *et al.*, *The STAR Trigger*, to be published in [36]
- [34] C. Adler *et al.*, *The STAR Level-3 Trigger System*, to be published in [36]

- [35] J. M. Landgraf *et al.*, *An Overview of the STAR DAQ System*, to be published in [36]
- [36] Nucl. Instrum. Methods volume dedicated to the detectors and the accelerator at RHIC
- [37] W. Blum and L. Ronaldi, *Particle Detection with Drift Chambers*, Springer-Verlag, Germany (1993)
- [38] C. Adler, A. Denisov, E. Garcia, M. Murray, H. Stroebele and S. White, Nucl. Instrum. Methods **A470** (2001) 488
- [39] J. E. Gonzales, *Calibration of STAR Zero Degree Calorimeters*, STAR Note 437 (2001), unpublished
- [40] RHIC Design Manual, Brookhaven National Laboratory (2000), available at <http://www.agsrhichome.bnl.gov/AGS/Accel/Reports>
- [41] C. Adler, Ph.D. thesis, Universität Frankfurt (2002)
- [42] P. Yepes, Nucl. Instrum. Methods **A380** (1996) 582
- [43] J. Berger, Ph.D. thesis, Universität Frankfurt (2003)
- [44] C. Adler *et al.*, STAR Coll., Phys. Rev. Lett. **87** (2001) 262301-1
- [45] M. Calderón de la Barca Sánchez, Ph.D. thesis, Yale University (2001)
- [46] R. Bossingham *et al.*, *STAR Offline Simulations and Analysis Software Design*, STAR Note 281 (2000), unpublished
- [47] D. Liko, *Track Fitting in the STAR Detector using the Kalman Filter Method*, STAR Note 87 (1992), unpublished; update of STAR Note 87 by A. C. Saulys (2000), unpublished
- [48] S. Margetis and D. Cebra, *Main Vertex Reconstruction in STAR*, STAR Note 89 (1992), unpublished
- [49] H. A. Bethe, Annalen der Physik **5** (1930) 325; F. Bloch, Z. Physik **81** (1993) 363
- [50] E. Fermi, Phys. Rev. **57** (1940) 485
- [51] U. Fano, Annu. Rev. Nucl. Part. Sci. **13** (1963) 1
- [52] L. Landau, Journal of Physics U.S.S.R. **8** (1944) 201
- [53] Y. Fisyak, private communication

- [54] GEANT, Detector Simulation Software, R. Brun et al., CERN-DD/EE/84-1 (1987)
- [55] W. G. Gong, *The STAR-TPC Slow Simulator*, STAR Note 197 (1995), unpublished; B. Lasiuk, *TPC Response Simulator, User Guide and Reference Manual*, STAR Offline Library Writeup (2000), unpublished
- [56] G. Ambrosini *et al.*, Newmass (NA52) Coll., nucl-ex/0011016, presented at Symposium on Fundamental Issues in Elementary Matter, Bad Honnef, Germany, September 25-29, 2000, published in *Acta Phys. Hung., Heavy Ion Phys.* **14** (2001)
- [57] C. Adler *et al.*, STAR Coll., *Phys. Rev. Lett.* **87** (2001) 262302-1
- [58] S. A. Bass *et al.*, UrQMD Coll., *Prog. Part. Nucl. Phys.* **41** (1998) 225; M. Bleicher *et al.*, UrQMD Coll., *J. Phys. G: Nucl. Part. Phys.* **25** (1999) 1859
- [59] D. E. Groom *et al.*, Particle Data Group, *Review of Particle Physics*, *Eur. Phys. J. C* **15** (2000) 1
- [60] T. F. Hoang, B. Cork and H. J. Crawford, *Z. Phys. C* **29** (1985) 611
- [61] O. Barannikova, F. Wang, STAR Coll., nucl-ex/0210034, presented at 16th International Conference On Quark Matter 2002, Nantes, France, 18-24 Jul 2002, to be published in *Nucl. Phys. A*
- [62] D. Magestro, *J. Phys. G* **28** (2002) 1745; D. Magestro, poster presented at 16th International Conference On Quark Matter 2002, Nantes, France, 18-24 Jul 2002 and shown in [63]
- [63] T. S. Ullrich, nucl-ex/0211004, presented at 16th International Conference On Quark Matter 2002, Nantes, France, 18-24 Jul 2002, to be published in *Nucl. Phys. A*
- [64] D. H. Rischke, *Nucl. Phys.* **A698** (2001) 153c
- [65] G. Ambrosini *et al.*, Newmass (NA52) Coll., *Phys. Lett.* **B417** (1998) 202; R. Arsenescu *et al.*, Newmass (NA52) Coll., *Nucl. Phys.* **A661** (1999) 177c
- [66] T. A. Armstrong *et al.*, E864 Coll., *Phys. Rev.* **C61** (2000) 064908-1
- [67] I. G. Bearden *et al.*, NA44 Coll., *Eur. Phys. J. C* **23** (2002) 237
- [68] E. Schnedermann, J. Sollfrank and U. Heinz, *Phys. Rev.* **C48** (1993) 2462
- [69] P. J. Siemens and J. O. Rasmussen, *Phys. Rev. Lett.* **42** (1979) 880
- [70] S. V. Afanasiev *et al.*, NA49 Coll., *Phys. Lett.* **B486** (2000) 22



- [71] A. Dumitru and D. H. Rischke, *Phys. Rev.* **C59** (1999) 354
- [72] B. Monreal *et al.*, *Phys. Rev.* **C60** (1999) 031901
- [73] H. Appelshäuser *et al.*, NA49 Coll., *Eur. Phys. J. C* **2** (1998) 661
- [74] B. Tomášik, U. A. Wiedemann and U. Heinz, nucl-th/9907096
- [75] F. Laue *et al.*, STAR Coll., *Nucl. Phys.* **A698** (2002) 177c
- [76] S. Wang *et al.*, EOS Coll., *Phys. Rev. Lett.* **74** (1995) 2646
- [77] M. J. Bennet *et al.*, E878 Coll., *Phys. Rev.* **C58** (1998) 1155
- [78] T. A. Armstrong *et al.*, E864 Coll., *Phys. Rev. Lett.* **85** (2000) 2685
- [79] C. Blume *et al.*, NA49 Coll., nucl-ex/0208020, presented at 16th International Conference On Quark Matter 2002, Nantes, France, 18-24 Jul 2002, to be published in *Nucl. Phys. A*
- [80] N. Saito *et al.*, E886 Coll., *Phys. Rev.* **C49** (1994) 3211
- [81] J. Barette *et al.*, E814 Coll., *Phys. Rev.* **C50** (1994) 1077
- [82] S. Nagamiya *et al.*, *Phys. Rev.* **C24** (1981) 971; R. L. Auble *et al.*, *Phys. Rev.* **C28** (1983) 1552
- [83] T. Chujo *et al.*, PHENIX Coll., nucl-ex/0209027, presented at 16th International Conference On Quark Matter 2002, Nantes, France, 18-24 Jul 2002, to be published in *Nucl. Phys. A*
- [84] C. Adler *et al.*, STAR Coll., *Phys. Rev. Lett.* **87** (2001) 082301; M. L. Noriega *et al.*, STAR Coll., nucl-ex/0210031, presented at 16th International Conference On Quark Matter 2002, Nantes, France, 18-24 Jul 2002, to be published in *Nucl. Phys. A*
- [85] M. Murray *et al.*, NA44 Coll., *Nucl. Phys.* **A661** (1999) 456c
- [86] An extensive introduction to Bayesian statistics and its applications in high energy physics can be found in G. D'Agostini, *Bayesian Reasoning in HEP: Principles and Applications*, Academic Training Lectures, CERN (1998); the specific application to efficiency uncertainties is described for example in J. Conway, *Efficiency Uncertainties: A Bayesian Prescription*, CDF Technical Report, CDF/PUB/5894 (2002), unpublished



# Danksagung

An dieser Stelle möchte ich mich bei allen Personen bedanken, die zum erfolgreichen Abschluß dieser Arbeit beigetragen haben. Dabei gilt mein besonderer Dank Prof. Reinhard Stock für die gleichzeitige Aufnahme in das Institut für Kernphysik und der dauerhaften Entsendung in die USA mit der für Doktoranden sicher einmaligen Möglichkeit, das Level-3 Projekt „vor Ort“ zu verwirklichen.

Bedanken möchte ich mich natürlich auch bei Prof. Dieter Röhrich, der das Level-3 Projekt ins Leben rief und mich bei meinem Wunsch, als Doktorand in die USA gehen zu können, tatkräftig unterstützte.

Bei Prof. John Harris und seiner Arbeitsgruppe möchte ich mich für die herzliche Aufnahme an der Yale University bedanken, die mir den Einstieg in der STAR Kollaboration sehr leicht machte.

Besonderer Dank geht auch an meine Kollegen der Frankfurter Level-3 Gruppe Clemens Adler, Jens Berger, Thomas Dietel, Dominik Flierl und Soeren Lange für die erfolgreiche Zusammenarbeit, David Hardtke in Berkeley für die Unterstützung bei der Analyse der „Antimaterie“ und an die vielen anderen Kollegen der STAR Kollaboration, deren Hilfsbereitschaft und Anteilnahme an meiner Arbeit mich immer wieder motiviert hat.

Mein spezieller Dank gilt Andreas Schüttauf und Jerome Lauret. Viele gemeinsame Kinobesuche und genußvolle Abendessen verschönerten den Feierabend am BNL deutlich (und subventionierten die lokale Gastronomie auf Long Island). Aus netten Kollegen wurden gute Freunde.

Nicht unerwähnt soll die freundliche Unterstützung am IKF bleiben, insbesondere von Werner Amend, Heidrun Rheinfels-Immanns und Jutta Berschin. Bei meinen seltenen Besuchen am IKF waren die Hilfestellungen keineswegs selbstverständlich.

Mein größter Dank gilt jedoch meinen Eltern für die vielen, vielen Hilfeleistungen während dieser Zeit und ohne die mein Studium und diese Arbeit nicht möglich gewesen wären, meinen Freunden und vor allem meiner lieben Familie. Zusammen mit Euch ist das Leben einfach wundervoll. Danke.

# Curriculum Vitae

Christof Struck

## Persönliche Informationen

Geburtsdatum: 4. Mai 1973  
Geburtsort: Marburg  
Familienstand: verheiratet  
Staatsangehörigkeit: deutsch

## Schulbildung

1979 – 1983 Grundschule Wetter  
1983 – 1992 Gymnasium Martin-Luther-Schule, Marburg  
Abschluß: Abitur

## Studium

Okt. 1992 – Sept. 1997 Studium der Physik an der Philipps-Universität,  
Marburg  
Sept. 1994 Vordiplom in Physik  
Sept. 1997 Diplom in Physik,  
Thema der Diplomarbeit:  
„Weiterentwicklung des Datenaufnahmesystems  
für den NA49-Flugzeitdetektor und Messung der  
Deuteronenemission in Pb-Pb-Reaktionen bei  
158 GeV/u Strahlenergie“,  
Betreuer: Prof. Dr. Falk Pühlhofer  
Okt. 1997 Förderpreis der Heraeus-Stiftung  
Okt. 1997 – Dez. 1997 Wissenschaftlicher Mitarbeiter an der Philipps-  
Universität, Marburg  
seit Feb. 1998 Wissenschaftlicher Mitarbeiter am Institut für  
Kernphysik der J.W. Goethe-Universität,  
Frankfurt am Main  
während dieser Zeit:  
Apr. 1998 – Apr. 1999 Forschungsaufenthalt an der Yale University, USA  
Apr. 1999 – Jun. 2002 Forschungsaufenthalt am Brookhaven National  
Laboratory, USA